Apparent Horizons and Marginally Trapped Surfaces in Numerical General Relativity

Dissertation
zur Erlangung des akademischen Grades

doctor rerum naturalium (Dr. rer. nat.)

vorgelegt dem Rat der Astronomisch-Physikalischen Fakultät
der Friedrich-Schiller-Universität Jena

von

Diplomphysiker Norbert Lages

geboren am 23. Oktober 1978 in Überlingen

Gutachter

1. **Professor Bernd Brügmann, Friedrich-Schiller-Universität Jena**
2. **Professor Gerhard Zumbusch, Friedrich-Schiller-Universität Jena**
3. **Professor Kostas Kokkotas, Eberhard Karls Universität Tübingen**

Tag der Disputation: 7. Januar 2010

Contents

Zusammenfassung

Diese Dissertation beschäftigt sich mit *gerade noch äußerlich gefangenen Flächen* (abgekürzt MOTSs von Marginally Outer Trapped Surfaces) in der numerischen Relativitätstheorie. Diese Flächen definieren den *scheinbaren Horizont* welcher ein Konzept für die Oberfläche eines Schwarzen Loches ist. Mit seiner Hilfe lassen sich sowohl der Spin als auch die Masse eines Schwarzen Loches berechnen. Außerdem spielen gefangene Flächen eine wichtige Rolle in dem Beweis, dass unter recht allgemeinen Bedingungen zwangsläufig Singularitäten in der Allgemeinen Relativitätstheorie auftreten können.

In einer dreidimensionalen raumartigen Hyperfläche der Raumzeit ist die Lage der MOTSs durch eine elliptische, nicht-lineare partielle Differentialgleichung gegeben. Der zentrale Teil der Arbeit ist die Ausarbeitung einer Methode welche die Verwendung von Lösern dieser Differentialgleichung nach dem Newton-Verfahren verbessern soll. Newton-Verfahren verbessern schrittweise den anfänglichen Lösungsvorschlag, wenn der Anfangswert ausreichend gut (d.h. im Konvergenzbereich) gegeben wurde. Bei jedem Iterationsschritt kann das linearisierte Problem mit einem weiteren iterativen Verfahren gelöst werden. Dabei tritt eine Matrix auf, deren betragsmäßig maximaler Eigenwert ein mögliches Kriterium für die Konvergenz sogar der äußeren Iteration darstellt. Es kann schon zu Beginn berechnet werden. Die Arbeit untersucht ob oder wann diese Eigenwertmethode anwendbar ist. Parallel dazu wird durch gezielte Veränderung der zu lösenden Funktion eine Vergrößerung des Konvergenzbereiches erreicht. Dabei kommt die eben beschriebene Eigenwertmethode zum Tragen. Die Veränderungen bestehen hier aus einer Multiplikation mit ausgewählten Faktoren.

Als weiterer Punkt wird in dieser Arbeit untersucht, unter welchen Umständen sich MOTSs überlappen können. Dazu wurde unter anderem ein Programm geschrieben, welches MOTSs in einfachen axialsymmetrischen Raumkonfigurationen mit hoher Genauigkeit bestimmen kann. Als Ergebnis ist festzuhalten, dass sich MOTSs überlappen können. Dies wird bei drei Schwarzen Löchern gezeigt, kann jedoch auch abhängig von der Eichung der Koordinaten bei Simulationen mit zwei schwarzen Löchern auftreten. Zum Verständnis werden Einbettungsdiagramme verwendet.

Abstract

General Relativity has brought a variety of predictions about our universe since its formulation in the year 1915. These include among others strange objects like black holes and also gravitiational waves, the latter being in the focus of current research. Numerical relativity simulates those areas of the nonlinear theory where perturbation methods are not applicable, examples including supernovae or the merger of black holes or neutron stars.

The broad topic of this thesis is the finding of Marginally Outer Trapped Surfaces (MOTSs). They are of theoretical interest because of their use in the singularity theorem. But they also define the apparent horizon, a local concept for the surface of a black hole. The apparent horizon can be used to calculate the spin and the mass of a black hole.

Within a three-dimensional spatial hypersurface of the four dimensional spacetime the location of a marginally outer trapped surface is given by a non-linear elliptic partial differential equation. The main result of this work is the development of a method that makes solvers of Newton-type more reliable. Starting from an initial guess a Newton method iteratively solves the linearized system. One aspect is the consideration of the maximal absolute eigenvalue of the matrix that appears at every step of the Newton iteration. It is used in a criterion which determines the convergence of the overall method and is computable a priori. Based on this criterion changes to the elliptic equation are analyzed that increase the region of convergence of Newton methods.

Also the intersection of MOTSs are investigated. A program was written that is able to find MOTSs in axial symmetric geometries with high accuracy. As a result it is shown that MOTSs can overlap in configurations with three black holes. Depending on the coordinate gauge of the simulation this can also happen in configurations with two black holes. A heuristic explanation using embedding diagrams is given.

Chapter 1

Introduction

1.1 Overview

Nearly one hundred years after Einstein introduced his General Relativistic Theory of Gravitation in 1915 [33, 32] it is still a vivid place for theoretical and experimental physicists. At first researchers were bound to simplifying assumptions to get analytical results. With the advance of the computer new possibilites have arisen to solve and investigate the nonlinear partial differential equations of Einstein's theory.

Numerical relativity has come of age in recent years. One major breakthrough was achieved around the year 2005 by the evolution of two black holes during their merger phase [24, 14, 21, 58]. Currently several groups that use independent implementations are able to compute many orbits of two black holes. The researchers try to extract more and more physical information out of their simulations. One large focus is the construction of gravitational wave templates that can be used for the detection of gravitational waves by current detectors Virgo [2], GEO600 [75], LIGO [1] and TAMA [8] or the planned space-based instrument LISA [41]. Astrophysically interesting scenarios like the collisions and mergers of neutron stars or neutron stars with black holes can then be analyzed with these instruments. This will provide an additional source of information beside the electromagnetic spectrum, high-energy particles or neutrinos. Gravitational waves will reach the earth nearly undisturbed even through dense clouds of matter.

Most numerical codes that simulate relativistic scenarios separate the four-dimensional space-time into the familiar three dimensions of space that develops in one time direction, known as the 3+1 split. It is a standard tool to prepare Einstein's equation for the computer. Some recent developments are sketched in section 1.2.

One tool that is used during the evolution of the system is the apparent horizon. It can be thought of a surface of a black hole at one instant of time and has several applications in numerical relativity. Related objects, the marginally outer trapped surfaces (MOTSs), play a role in the singularity theorems of Penrose [56] and Hawking and Ellis [37]. The introductory part 1.3 will explain why marginally trapped surfaces are of interest for both numerical and theoretical relativists. The basic definition of a 'trapped surface' in section 1.3 will lead to an elliptic partial differential equation. This equation uses the 3+1 formulation. Methods for solutions are analyzed in the last chapter.

In section 1.4 existing apparent horizon finders are described. Several methods are used to find MOTSs; a rough classification distinguishes Newton-type solvers and flow like solvers. When the problem exhibits axial symmetry additionally an integration of an ordinary differential equation is possible. The latter will be explained thoroughly in chapter 2. A code is presented that can find MOTSs in axially symmetric space-times with high accuracy (section 2.2). In paragraph 2.3.2 the critical distance between two black holes for the appearance of a common horizon was compared to results of other groups.

A somewhat puzzling question of the topological outline of MOTSs is discussed in chapter 3. It is possible that these surfaces overlap each other but this behaviour is dependent on gauge choices. A heuristic explanation is given in chapter 3.3 where the overlap of MOTSs is tracked both in axisymmetric and in general three-dimensional setups. Embedding diagrams are used to visualize the different outcomes.

The idea of using specific eigenvalues of a Newton method and solving not the original equation but a related one is presented in chapter 4. First the general layout of a Newton method is shown on examples in spherical symmetry, where the elliptic partial differential equation for the expansion reduces to root finding

in one dimension (section 4.1). In subsequent sections the full expansion is linearized to get the Jacobian needed for a matrix representation of each iteration step (see 4.2.1). It is then explained why eigenvalues of the iteration matrix at one Newton step might have useful information about the behaviour of convergence. The particular statement is that 'initial data with maximal absolute eigenvalues of its iteration matrix greater than one will converge to one of the solutions of the elliptic problem'. In section 4.3.2 it is shown how the original elliptic equation can be changed by 'goal functions' to get a larger region of convergence. Both the characterization by the eigenvalue and the goal function approach are tested together for several surfaces around one and two black holes. The method is successful but has some dependence on the damping used in the Newton method.

The results are summarized in section 5. Several ideas are sketched how the eigenvalue method can be further tested. It is discussed how finding of apparent horizons in numerical relativity can be improved. Finally the appendix shows further or more detailed description of some parts of this work.

1.2 Developments in Numerical Relativity

Numerical Relativity and 3+1 Formalism The beauty and strength of Einstein's equation lies in its covariant formulation where space and time are represented by a four-dimensional manifold. This interweaving of time and space is not suited to numerical studies. Numerical setups require a Cauchy or initial value problem. Therefore the field equations were split into their spatial and temporal part a decomposition known as the 3+1 split or the ADM formalism. It is named after Arnowitt, Deser and Misner who published the leading work in 1962 [10]. Also York [77] contributed to its success.

For years the numerical relativity community tried to have stable evolutions of black holes, starting with head-on [64] and later grazing collisions the long term goal of two merging black holes was pursued. In 1998 Baumgarte und Shapiro [15] based on Shibata and Nakamura's work [62] reformulated the ADM equations in a set of partial differential equations that are known as the BSSN system.

It was this reformulation that made long-term stable evolutions possible. The outline of this formulation and some key concepts are given in the next paragraph, further details can be found in for example [17, 45, 4] or [26]. Here the notation and outline of the latter reference is used.

Einstein's Equations The field equations of general relativity relate the geometry of space-time with its matter and energy content. Written in index notation they state

$$R_{\mu\nu} - \frac{1}{2} g_{\mu\nu} R = 8\pi T_{\mu\nu} \tag{1.1}$$

where $g_{\mu\nu}$ is the metric tensor, $R_{\mu\nu}$ is the Ricci tensor, R is the Ricci scalar and $T_{\mu\nu}$ is the energy-momentum tensor. Throughout the thesis Greek indices will mark four-dimensional quantities, whereas three-dimensional objects are labeled with Latin letters from the middle of the alphabet. Natural units are chosen such that $c = G = 1$.

The 3+1 split will assume a family of three-dimensional surfaces Σ_t that foliate space-time with a continuous parameter t. At each point the ten equations of (1.1) can be projected onto the local hypersurface and onto the normal to that surface n^μ. An observer who travels along the normal will measure the proper interval α, called the *lapse function* between slices. Additionally he can have a spatial displacement vector β^μ, called the *shift vector* such that his time direction t^μ is

$$t^\mu = \alpha n^\mu + \beta^\mu. \tag{1.2}$$

The functions α and β^μ reflect the gauge freedom of the coordinate system. The 3-metric inside the hypersurface γ_{ij} and the second fundamental form or extrinsic curvature given by the Lie-derivative

$$K_{ij} = -\frac{1}{2} \mathcal{L}_n \gamma_{ij} \tag{1.3}$$

will give the minimal information that is needed for a Cauchy evolution.

The ADM Equations Combining equations (1.1) with conditions on the hypersurface will give the ADM equations that comprise the evolution equations, the

Hamiltonian constraint and the momentum constraint respectively:

$$\begin{aligned}\partial_t K_{ij} &= \alpha\left(\bar{R}_{ij} - 2K_{il}K^l_j + KK_{ij} - 8\pi S_{ij} + 4\pi\gamma_{ij}(S-\rho)\right)\\ &\quad - \bar{\nabla}_i\bar{\nabla}_j\alpha + \beta^l\bar{\nabla}_l K_{ij} + K_{il}\bar{\nabla}_j\beta^l + K_{jl}\bar{\nabla}_i\beta^l\,, \qquad (1.4)\\ 16\pi\rho &= \bar{R} + K^2 - K_{ij}K^{ij}\,, \qquad (1.5)\\ 8\pi j^i &= \bar{\nabla}_j(K^{ij} - \gamma^{ij}K). \qquad (1.6)\end{aligned}$$

Here, $\bar{\nabla}_i$ is the spatial covariant derivative operator compatible with γ_{ij}, $\bar{R}_{ij}$ is the Ricci tensor calculated from γ_{ij}, $K = K^i_{\ i}$, ρ is the matter energy density, $S_{ij} =\perp T_{ij}$ is the matter stress tensor and $S = S^i_{\ i}$. The operator $\perp$ projects onto the spatial hypersurface along all free indices.

These equations describe the evolution of the metric and the extrinsic curvature. If the constraint equations are fulfilled on the initial slice then analytically they will hold at later times, in other words the constraints are compatible with the evolution. Numerically however there are unstable modes that may grow rapidly and crash the simulation.

The BSSN system is based on the *York-Lichnerowicz Conformal Decomposition* and rewrites the above ADM equations (1.4)-(1.6) to deal with these instabilities. First the conformal factor ψ_0 between the physical metric and a flat background is introduced followed by the split of the extrinsic curvature into a trace-free $\bar{A}_{ij}$ and a trace part K

$$\begin{aligned}g_{ij} &= \psi_0^4\tilde{g}_{ij}\,, \qquad (1.7)\\ K_{ij} &= \psi_0^{-2}\bar{A}_{ij} + \frac{1}{3}g_{ij}K. \qquad (1.8)\end{aligned}$$

Instead of the original ADM variables the following set of variables is evolved over time:

$$\begin{aligned}\phi &= \ln\psi_0\,, \qquad (1.9)\\ \tilde{A}_{ij} &= \psi_0^{-6}\bar{A}_{ij}\,, \qquad (1.10)\\ \tilde{\Gamma}^i &= -\partial_j\tilde{g}^{ij}. \qquad (1.11)\end{aligned}$$

Moreover for the real simulation the gauge has to be chosen. In the BAM code that was used for chapter 3 the '1+log' slicing and gamma-freezing shift conditions

$$(\partial_t - \beta^i \partial_i)\alpha = -2\alpha K \quad \text{and} \tag{1.12}$$

$$\partial_t \beta^i = \frac{3}{4} B^i, \quad \partial_t B^i = \partial_t \tilde{\Gamma}^i - \eta B^i \tag{1.13}$$

were applied. Usually the replacement $\partial_t \to \partial_0$ is assumed (see [22]).

1.3 Trapped Surfaces in General Relativity

Quasi-local Definitions in Numerical Relativity Familiar notions of Newtonian physics can not be carried over easily to general relativity. One obvious example comprises the notion of mass: the Schwarzschild geometry has a vanishing energy-momentum tensor, yet a mass is defined non-locally by comparing areas or lengths in the Newtonian limit. What is the spin of an object that is moving in a dynamic space? In general relativity masses and spins can not be added up for arbitrary volumes in space. If the space if asymptotically flat then it is possible to define a mass at infinity. Asymptotic flatness means the existence of preferred coordinates at large distance and known fall-off rates of the metric components. But this definition includes neither a well defined location in space nor in time, it is only defined in stationary space-times.

In numerical relativity there is at least an intrinsic form of simultaneity introduced by the 3+1 split. All events belonging to one time slice are space-like separated and can be seen as 'at the same instant of time'. Definitions that are valid within only one time-slice are here called *quasi-local*. MOTSs are quasi-local objects that depend on the three-metric and the extrinsic curvature that comprise one spatial hypersurface.

The Expansion and Marginally Outer Trapped Surfaces One remarkable feature of General Relativity is the prediction of its own break-down in the form of singularities that can develop under quite general conditions. First Penrose [56] then Hawking and Ellis [37] and Wald [72] showed necessary conditions.

The quasi-local description of a region from which even light can not escape is based on trapped surfaces that in turn are defined by their expansions. The expansion and its cousins shear and twist are useful ways to describe congruences of null geodesics in space-time. An introduction will be given in the following lines. More details can be found in chapter 9 of Wald [72].

Consider a null geodesic congruence. In an open subset O of a manifold a congruence is a family of curves such that through each point in O there passes precisely one curve in this family. The tangents k^a to these curves describe a vector field on O. The tensor field $B_{ab} = \nabla_a k_a$ describes how neighbouring tangents behave. The related tensor field $\hat{B}_{ab}$ can be decomposed into

$$\hat{B}_{ab} = \frac{1}{2} H \hat{h}_{ab} + \hat{\sigma}_{ab} + \hat{\omega}_{ab}, \tag{1.14}$$

where H, $\hat{\sigma}_{ab}$ and $\hat{\omega}_{ab}$ have the physical interpretation of expansion, shear and twist respectively. The hat over the expressions is a reminder that there is really an equivalence class involved because you can not find a unique subspace that is orthogonal to the original null geodesics. The expansion measures the average 'spread' of infinitesimally nearby geodesics. The twist shows their rotation and the shear describes the stretching and parallel displacement of curves from the congruence.

A *(marginally) outer trapped surface* is defined as a compact, space-like two-dimensional sub-manifold, for which the expansion H of outgoing orthogonal geodesics is $H \leq 0$ ($H = 0$) everywhere. Generally trapped surfaces need additionally that ingoing geodesics have expansion $H < 0$ but that is commonly the case such that this condition will not be mentioned later: only the condition on *outer* trapped surfaces is considered here. These definitions are still in the four-dimensional manifold. But they can be broken down to the objects of the 3+1 split, that are the metric γ_{ij} and the extrinsic curvature K_{ij} [71, 35, 40]. The condition $H = 0$ for every outward unit normal s^i on a marginally outer trapped surface is

$$H \equiv \nabla_i s^i + K_{ij} s^i s^j - K = 0. \tag{1.15}$$

The *apparent horizon* is the outermost or the union of all outermost of these

MOTSs in the case disjunct sets are given. It is a quasi-local equivalent to the *event* horizon. Both describe in some sense the surface of a black hole. But the latter is defined as the set of null-geodesics that will reach future null-infinity and so is clearly not defined inside one hypersurface unlike the apparent horizon. Apparent horizons are used during a simulation as an approximation of the location of the event horizon, and is thus especially useful for simulations that excise the black hole region including the singularity.

The apparent horizons within each hypersurface can be stacked together to give the so-called *trapping horizon* [38][1]. If the resulting trapped tube is null, Ashtekar and others [11] named it an *isolated horizon*, whereas *dynamical horizons* [12] can also have space-like parts. These objects resemble the event horizon more closely with respect to topology.

Use of MOTSs and Apparent Horizons There are several applications of apparent horizons both in numerical and theoretical relativity. The primary example for the latter are the singularity theorems [37]. One version of them states that the space-time $\mathcal{M}$ can not be null geodesically complete if (1) $R_{\mu\nu}K^\mu K^\nu \geq 0$ for all null vectors K^μ (implied by the weak energy condition), (2) there is a non-compact Cauchy surface in $\mathcal{M}$ and (3) there is a closed trapped surface in $\mathcal{M}$. The reverse of being geodesically complete implies the existence of a singularity. Since both (1) and (2) are normally seen in physical space-times all that is left is to show the existence of trapped surfaces.

The *cosmic censorship hypothesis* states that these singularities can not be seen from outside. Each singularity should be hidden inside the event horizon. Otherwise the singular part could effect an observer in a non-predictable manner. The location of the apparent and the event horizon coincides for stationary space-times (and suitable spatial hypersurfaces) but because of the slicing dependence the apparent horizon is not a good indicator for cosmic censorship. Wald and Iyer [73] showed that it is possible to slice the Schwarzschild geometry with hypersurfaces that come arbitrary close to the singularity but no apparent horizon exists.

[1] Some subtleties are involved in this definition, concerning inside or outside directions. See appendix A of that reference.

In general relativity quantities like the mass have only meaning to the global space-time assuming asymptotic flatness. But to have some local values at all, one can locally define the mass and the spin of a black hole by integrations over a surrounding surface. The apparent horizon as a geometric object in the hypersurface, is independent of the coordinates and is therefore the distinguished choice for such a surface. The formulas for the area, the spin and the mass are [30, 25]

$$A_{AH} = \oint_{AH} \mathrm{d}^2 A, \tag{1.16}$$

$$S_{AH} = \frac{1}{8\pi} \oint_{AH} (\phi^i R^j K_{ij}) \, \mathrm{d}^2 A \quad \text{and} \tag{1.17}$$

$$M_{AH} = \frac{1}{2R_{AH}} \sqrt{R_{AH}^4 + 4S_{AH}^2}, \tag{1.18}$$

with the areal radius $R_{AH} = \sqrt{\frac{A_{AH}}{4\pi}}$. The integrals are taken with the area measure constructed from the induced two-metric. K_{ij} is the extrinsic curvature, R^i is the outgoing unit normal on the surface and ϕ^i is a rotational Killing vector. In practice the latter is hard to find [27], thus the flat space coordinate rotational killing vectors are taken.

1.4 Apparent Horizon Finders

Over the years several finders for apparent horizons were studied. They vary both in the description of the surface and in the choice of the actual solving procedure of the differential equation. Some main aspects are described in the following lines. A more detailed survey can be found in Thornburg's Living Review [71].

Earlier work on apparent horizons focused on the time-symmetric cases because there are analytic formulas by Misner and Wheeler describing multiple black holes [50]. These configurations have become the standard test cases for codes [3]. The first methods by Brill and Lindquist [20] used Legendre polynomials to approximate the surface. The surface area was minimized by the application of a variational principle. Čadež [23] pioneered the use of a geodesic integration combined with the idea of a shooting method to find solutions of the elliptic partial

differential equations. This approach was refined by Bishop in his work [18, 19], where it was found that an additional extremal (maximal) surface exists for two black holes with small separation.[2] The parameterization ansatz can find general, non star-shaped surfaces. In chapter 2 our own implementation of an axisymmetric apparent horizon finder using this method is described. One can also minimize the area of the rotational volume that is created when turning the surface line around the axis of symmetry. But this minimization is strictly possible only in slices of time-symmetry.

Another possibility to find the apparent horizon in axial symmetry uses the same ansatz as in three dimensions described later. The horizon is expressed as a function $h(\theta, \phi)$ in usual spherical coordinates, it is $\partial_\phi h = 0$ because of symmetry. Then the isoline $F(r, \theta) = r - h(\theta) = 0$ describes the surface.

There are several ways to define a surface in three (spatial) dimensions. Most apparent horizon finders use a star-shaped outline. Then the surface can be written as height function over two angular coordinates [69, 60]. It is common to use spherical harmonics [52, 16, 46]. Metzger [49] presented a method based on finite elements, but that was not developed further. Another possibility is the use of level set functions. They are described by Pasch [55] and Shoemaker et al. [63] and may also be used for event horizon finders [29].

The elliptic partial differential equation (1.15) can be tackled by a variety of methods. The most prominent distinction is that of a local and a global algorithm. Most apparent horizon finders are local, meaning they need a good initial guess to find the horizon. On the other hand these methods are often faster. An algorithm is called 'global' if it can also handle initial guesses not close to the solution. Flow algorithms are known to have this feature but it is not proven to hold under all conditions. Anninos et al. [9] describe another class of algorithms in which scalar norms are defined on the expansion of the trial surface. General minimization schemes can then change the shape and thus decrease the expansion until it drops below a given tolerance. But their generality makes them slow and the tolerance level is hard to determine optimally.

[2] Hawking and Ellis [37] thought of a different second 'inner apparent horizon' when they consider a spherical thin shell of dust falling into a black hole.

Flow methods stand out for their robustness against bad initial guesses. They define a gradual change of the initial surface proportional to the local expansion. Obviously near to the apparent horizon with expansion $H = 0$ the speed will also tend to zero. Special choices of the flow functions must be applied. One major improvement was introduced by Gundlach's [35] 'fast-flow' algorithm. He iterates each mode of the surface with different speed, thus high frequency modes do not slow down down the evolution. His method is based on the spectral code that Nakamura et. al. developed in 1984 [52].

Direct methods solve the PDE (1.15) mainly by using a variant of Newton's method. The set of equations is solved to first (linear) approximation. In an iteration procedure the resulting surface is taken as next best initial guess until the solution is sufficiently close. Usually when the first guess is too far away from the solution the iteration does not converge. Thornburg [69] tested the robustness and found problems especially for high frequency changes. In chapter 4 alternative goal functions will be used to broaden the convergent regime and an eigenvalue procedure gives expectations about the convergence beforehand.

Chapter 2

Trapped Surfaces in Axial Symmetry

Starting in the 1960s finders of marginally trapped surfaces were implemented in the axisymmetric cases in general relativistic space-times. Of those methods already described in the introduction 1.4 the more general parameterization ansatz will be used in this thesis. It is not restricted to star-shaped surfaces. Consider a surface line given by $\rho(\lambda)$ and $z(\lambda)$ where z is the coordinate along the axis of symmetry and ρ is the distance from it. The solution can be found starting from correct initial data by integration in such a way that everywhere the expansion is preserved to be zero.

The parameterization of that path is governed by a second order differential equation with Neumann type boundary conditions on the axis (see 2.6). The solution can be found by a shooting method. Special care has to be taken at and near to the axis ($\rho \ll 1$), as shown in chapter 2.1. The solutions in time-symmetric slices represent surfaces of extremal area, and one has to decide based on other criterias whether these are maximal or minimal surfaces. The outermost of these solutions represents the *outermost* marginally trapped surface and therefore the apparent horizon.

In this thesis a numerical implementation of a finder of marginally trapped surfaces in axial symmetry with time-symmetric analytical data is presented. One

main focus is the accuracy of that code, once established it was used to find the marginally trapped surfaces of two black holes with very small separation. It can also track 'maximal' surfaces for two or three black holes. Finally overlapping marginally trapped surfaces are found for three black holes. In its standard form the code accepts the space-time data of a conformal axisymmetric Brill-Lindquist metric.

2.1 Marginally Trapped Surfaces as Geodesics

The following section will explain how the problem of finding a trapped surface in axial symmetry can be recast into the problem of finding a geodesic in a related space. The derivation is close to that of [18] and can also partly be found in [40].

Consider the location of a marginally trapped surface S in a time-symmetric and axisymmetric hypersurface. The 3-metric is given by

$$\mathrm{d}s^2 = \psi^4(\,\mathrm{d}\rho^2 + \rho^2\,\mathrm{d}\phi^2 + \,\mathrm{d}z^2), \tag{2.1}$$

with cylindrical coordinates ρ, ϕ and z. The extrinsic curvature vanishes, i. e. $K_{ij} = 0$. The conformal factor ψ is given in vacuum by the solution of $\nabla^2\psi = 0$ and reads

$$\psi(\rho, z) = 1 + \frac{1}{2}\sum_{i=1}^{N} \frac{m_i}{\sqrt{\rho^2 + (z - z_i)^2}} \tag{2.2}$$

where N is the number of masses m_i at positions z_i on the axis of symmetry.

Because of the rotational symmetry a closed surface can be fully described by a path $z(\lambda)$, $\rho(\lambda)$ in one half of the z-ρ-plane. The ϕ-direction of the complete surface is re-established by rotating this line around the axis of symmetry. In order to get a closed volume the path has to start and end on the axis. Moreover the curve must reach the z-axis perpendicular otherwise the resulting surface would not be smooth.

The key steps of using a geodesic are the following. In time symmetric slices of space-time the condition for a vanishing expansion reduces to $\nabla_i s^i = 0$ for the unit normal s^i on the surface S (see section 1.3) – which is exactly the condition

on finding minimal surfaces. The variation of the area reduces to finding a line of extremal length (a geodesic) in the ρ-z-plane with some metric that has yet to be defined.

The area of the surface in the Brill-Lindquist time-symmetric metric (2.1) is

$$\begin{aligned} A &= 2\pi \int_{\lambda=0}^{\lambda_1} \rho\psi^2 \sqrt{\psi^4 \, \mathrm{d}z^2 + \psi^4 \, \mathrm{d}\rho^2} \\ &= 2\pi \int_{\lambda=0}^{\lambda_1} \rho\psi^4 \sqrt{\dot{z}^2 + \dot{\rho}^2} \, \mathrm{d}\lambda \end{aligned} \tag{2.3}$$

where the parameterization of the surface is done by $\rho(\lambda)$ and $z(\lambda)$ and 'dot' means differentiation with respect to λ. The end value λ_1 is not fixed initially, it is related to the area, and thus unknown at first. Using the fact that the affine parameter can be adjusted by $\mathrm{d}\tilde{\lambda} = \rho\psi^4 \sqrt{\dot{\rho}^2 + \dot{z}^2} \, \mathrm{d}\lambda$ such that the new $\mathrm{d}\tilde{\lambda}$ is proportional to the local area element, then $A = 2\pi \int_{\lambda=0}^{\lambda_1} \mathrm{d}\tilde{\lambda} = 2\pi\lambda_1$.

Finding the extremum of the area corresponds now to the problem of finding the curve of extremal length in the metric

$$\mathrm{d}s^2 = (\rho\psi^4)^2 (\, \mathrm{d}\rho^2 + \, \mathrm{d}z^2). \tag{2.4}$$

From the geodesic equation

$$\frac{\mathrm{d}^2 x^i}{\mathrm{d}\lambda^2} + \Gamma^i_{kl} \frac{\mathrm{d}x^k}{\mathrm{d}\lambda} \frac{\mathrm{d}x^l}{\mathrm{d}\lambda} = 0 \tag{2.5}$$

the following partial differential equations of second order for the coordinates

$$\begin{aligned} 0 &= \ddot{\rho} + 8\frac{\partial_z \psi}{\psi} \dot{z}\dot{\rho} + (1/\rho + 4\frac{\partial_\rho \psi}{\psi})(\dot{\rho}^2 - \dot{z}^2) \qquad \text{and} \\ 0 &= \ddot{z} + 4\frac{\partial_z \psi}{\psi}(\dot{z}^2 - \dot{\rho}^2) + 2(1/\rho + 4\frac{\partial_\rho \psi}{\psi})\dot{\rho}\dot{z} \end{aligned} \tag{2.6}$$

can be derived. Note that these equations for the second derivatives are singular at $\rho = 0$. To complete the description of the problem we specify boundary conditions. These are readily established from the smoothness of the surface. The path

has to start and to end perpendicular to the z-axis, i.e.

$$\begin{aligned} \rho(0) &= 0, & \dot{z}(0) &= 0, \\ \rho(\lambda_1) &= 0 \qquad \text{and} & \dot{z}(\lambda_1) &= 0. \end{aligned} \tag{2.7}$$

The solution of these partial differential equations will produce curves that correspond to surfaces which have extremal area. Therefore lines that satisfy equations (2.12) and (2.13) can either correspond to surfaces of minimal or of maximal area. In asymptotically flat space-times both the outermost surface and the innermost extremal surfaces closest to every puncture must be minimal. The former comes from the fact that the area of surfaces far away from the black holes will be very large. The latter represent the outermost solution as seen from the asymptotically flat end of each black hole.

2.2 Implementation and Accuracy

The straightforward method of introducing additional two variables for $\dot{z}$ and $\dot{\rho}$ and writing the system with four equations and four variables yields a rather inaccurate method. The relative lengths of the second derivatives are crucial in getting the right direction of the geodesic, but these do not sum up stably. The following section describes these issues and solutions.

2.2.1 Choice of Variables

The main idea lies in choosing a better set of variables. Bishop [19] introduces the variable $\alpha = \arctan(\dot{\rho}/\dot{z})$ (compare also [40]). It describes the orientation of the tangent of the path. From the metric the first integral

$$1 = (\rho\psi^4)^2(\dot{z}^2 + \dot{\rho}^2) \tag{2.8}$$

is already known and can be automatically satisfied when the two derivatives fulfill

$$\dot{\rho} = \frac{1}{\rho\psi^4}\sin(\alpha) \quad \text{and} \tag{2.9}$$

$$\dot{z} = \frac{1}{\rho\psi^4}\cos(\alpha). \tag{2.10}$$

Since both (2.9) and (2.10) show a singularity at $\rho = 0$ a system of three rescaled variables $y_0 = \rho^2$, $y_1 = z\rho^2$ and $y_2 = \alpha\rho^2$ is used. The primary variables are then given by

$$\rho = \sqrt{y_0}, \qquad z = y_1/y_0 \qquad \text{and} \qquad \alpha = y_2/y_0. \tag{2.11}$$

The differential equations (2.6) become

$$\begin{aligned}
\dot{y}_0 &= 2\psi^{-4}\sin(\alpha), \\
\dot{y}_1 &= \psi^{-4}\left(\rho\cos(\alpha) + 2z\sin(\alpha)\right) \qquad \text{and} \\
\dot{y}_2 &= \psi^{-4}\left(\cos(\alpha) + 2\alpha\sin(\alpha) + 4\rho\left(\partial_\rho\psi\cos(\alpha) - \partial_z\psi\sin(\alpha)\right)/\psi\right).
\end{aligned} \tag{2.12}$$

The angle α starts with $\alpha(0) = \pi/2$. When it reaches the axis again it will either be $\alpha(\lambda_1) = -\pi/2$ or $\alpha(\lambda_1) = 3\pi/2$ depending on the direction. The boundary conditions for the new variables are well defined by

$$\begin{aligned}
y_i(0) &= 0, & y_i(\lambda_1) &= 0, \qquad i = 0, 1, 2, \\
\dot{y}_0(0) &= 2\psi^{-4}, & \dot{y}_0(\lambda_1) &= -2\psi^{-4}, \\
\dot{y}_1(0) &= 2\psi^{-4}z(0), & \dot{y}_1(\lambda_1) &= -2\psi^{-4}z(\lambda_1), \\
\dot{y}_2(0) &= \psi^{-4}\pi, & \dot{y}_2(\lambda_1) &= -\psi^{-4}\pi.
\end{aligned} \tag{2.13}$$

In summary the problem of unstable double integrations is overcome by introducing another variable α leading to partial differential equations of first order. The problem of the pole on the axis is cured by having the variables stretched by a factor of ρ^2. The remaining issue is the region at the axis itself. The primary variables z and α of equations (2.12) need a division by $y_0 = \rho^2$. For the initial values $y_0(0) = y_1(0) = y_2(0) = 0$ they are undefined. One has to enter directly the

known physical data at this stage.

2.2.2 Accuracy and Step Size

This paragraph derives the estimate for a good step size λ to be of the order or smaller than ρ^2. The notation $x \sim s$ will be used to express that variable x has the same order of magnitude as expression s. As a starting point consider the value of the integration routine to be $\rho = \rho_0$, $z = z_0$ and $\alpha = \alpha_0$ where both z_0 and α_0 are of the order one.

Assume that the path is not near to any of the punctures such that the conformal factor in equation (2.2) is $\psi \sim 1$ and its derivatives have magnitudes $\partial_z \psi \sim 1$ and $\partial_\rho \psi \sim \rho_0$. Otherwise these terms become larger and cause a slowdown of the integration (see later in 2.2.4). This is one reason why the examination of the behaviour of the inner MOTSs for black holes with small separation is numerically very difficult. The trigonometric expressions $\sin(\alpha)$ and $\cos(\alpha)$ are also of order one except for values that are near to multiples of $\pi/2$, but these cases do not change the overall statement.

With these assumptions the magnitudes and changes of the integration variables $y^{(n)} = (\rho_0^2, \rho_0^2 z_0, \rho_0^2 \alpha_0)$ after one (Eulerian) time step with fixed step size $\Delta\lambda$ are $y^{(n+1)} = y^{(n)} + \Delta\lambda\, \dot{y}^{(n)}$ and have magnitudes

$$y_0^{(n+1)} \sim \rho_0^2 + \Delta\lambda\,(1 + \rho_0)\,, \tag{2.14}$$

$$y_1^{(n+1)} \sim \rho_0^2 + \Delta\lambda\,(1 + \rho_0)\,, \tag{2.15}$$

$$y_2^{(n+1)} \sim \rho_0^2 + \Delta\lambda\left(1 + \rho_0 + \rho_0^2\right). \tag{2.16}$$

In our case ρ shall have an order of magnitude from zero to one, then the above expressions reduces to the statement $y^{(n+1)} \sim \rho_0^2 + \Delta\lambda$. On one hand we want that each step changes ρ^2 only by a small amount such that $\Delta\lambda \ll \rho^2$. On the other hand for numerical implementations it is important to add two values with comparable absolute size. Otherwise the smaller number will not contribute all its valid digits to the final answer. So we demand

$$\Delta\lambda \lesssim \rho_0^2 \tag{2.17}$$

for our algorithm.

From a practical point of view $\Delta\lambda$ is limited by the run time of the code, experimental data gives a limit of about $\Delta\lambda \approx 10^{-9}$. Together with condition (2.17) the integration can only be guaranteed to be stable for values of roughly $\rho > 10^{-5}$. In production runs of the code these limitations were mitigated by using an adaptive step size algorithm. But for step sizes of variable length the convergence behaviour that is shown in the next section could not be obtained. Therefore all the production runs later on will not include a thorough convergence analysis. Nevertheless the correctness of the runs was shown at least for some cases where both the fixed and the adaptive step size method were compared.

It was pointed out that an integration near the axis is somewhat problematic due to the necessity of a small step size. In this implementation of an axisymmetric finder of marginally trapped surfaces the first Runge-Kutta step away from the axis is treated separately: the first derivatives are calculated by the boundary conditions of ρ, z and α that are given in equation (2.13). The step size of this first step was adjusted to reach some given ρ_0, from that point on the integration is a normal Runge-Kutta method.

2.2.3 Region of Convergence

The validity of the code was examined by a series of convergence tests. The accurate implementation of the numerical method is thus tested. The underlying idea relies on the fact that the overall error of a discretization should behave in a foreseeable manner when the resolution is increased. The basic assumption for finite difference approximations is the possibility to expand the solution in a Taylor series around a point (see e.g. [54]). Assume a function f is computed with a finite differencing stencil of order n. Then for a fixed resolution Δ and multiple of it the solutions can be written as

$$f_\Delta = f_{exact} + C\ \Delta^n \quad + O(\Delta^{n+1}), \tag{2.18}$$

$$f_{2\Delta} = f_{exact} + C\ (2\Delta)^n + O(\Delta^{n+1}) \quad \text{and} \tag{2.19}$$

$$f_{4\Delta} = f_{exact} + C\ (4\Delta)^n + O(\Delta^{n+1}), \tag{2.20}$$

where the constant C does not depend on Δ. Taking differences and neglecting higher order error terms one gets

$$f_{4\Delta} - f_{2\Delta} = \frac{4^n - 2^n}{2^n - 1}(f_{2\Delta} - f_{\Delta}) = 2^n(f_{2\Delta} - f_{\Delta}) \tag{2.21}$$

as the estimated behaviour of the differences.

The prefactor 2^n is often called the *convergence factor*, which can easily be generalized to the case where the resolutions are not simple multiple of each other. Note that this idea of convergence analysis carries over to the integration in (pseudo-)time by a Runge-Kutta method because it is also based on a Taylor expanded solution. For this analysis the step size $\Delta = \Delta\lambda$ was always doubled when going to the next coarser resolution and with the Runge-Kutta method of order $n = 4$ the convergence factor is expected to be 16.

One convergence test consists of three runs of different resolutions Δ, 2Δ and 4Δ. From these the differences are taken as shown in (2.21) and the higher resolved runs are multiplied by the expected convergence factor. The resulting curves are compared by visual inspection (see later in figure 2.1). In the case of this axisymmetric study an additional parameter ρ_0 was considered. ρ_0 is the distance from the axis at which the regular integration starts. The first step from $\rho = 0$ to $\rho = \rho_0$ was taken to be one step of Runge-Kutta type. It will be shown that the needed accuracy for one integration depends on this parameter as was explained in section 2.2.2.

One more detail about the difference of two curves should be mentioned. The naive method for comparing runs could use every fourth point of the high resolution run and compare it with every second point of the middle resolution run and with each point of the low resolution run. But actually only the location of the whole curves should be compared against each other. This might be seen as neglecting phase shifts between the two integrations. For this analysis the output of the two curves were first interpolated to sixth order as a function $\rho(z)$ and then the resulting curves were subtracted. This method introduces large errors near to $z = z_0$ because the slope is expected to reach infinity (curves perpendicular to the z-axis). This can be seen in the convergence plots in figure 2.1 on the right side.

As a test condition an integration of one path in a Brill-Lindquist metric with two equal mass black holes $m_1 = m_2 = 1$ at $a_1 = 0.75$ and $a_2 = -0.75$ was performed. The curves started at $z_0 = 1.25$ that is close to the location where the apparent horizon lies and they terminated at $z = 0$. The outcome of every run can loosely be put into one of the following three categories that are both based on the criterion (2.17) and on the visual outcome. One representative of each type is shown in figure 2.1.

Type I covers curves that reach the expected 4^{th} order convergence, these have $\Delta\lambda \approx \rho_0^2$. In *type II* all curves are collected that show convergence only to a very low order, they correspond to runs that are under-resolved with $\Delta\lambda \gtrsim \rho_0^2$, their errors are of the order 10^{-8} to 10^{-4}. This came as no surprise, far more astonishing is the behaviour for integrations of *type III*. Despite having the step size one order of magnitude below the theoretically needed value of $\Delta\lambda \approx \rho_0^2$ and having differences from 10^{-11} to 10^{-12} they are not convergent. It seems that the accuracy of the variables for the whole equations levels off at around 10^{-12}. Throughout all combinations of ρ_0 and $\Delta\lambda$ the smallest differences in the convergence tests are of this order of magnitude and thus destroys convergence. For comparison the program was also run with increased precision, the results are in appendix B.

Independent of the above statements one can not increase the resolution arbitrarily. One reason was already mentioned in the previous section and states that decimal places are lost due to adding values that have far different magnitudes. Another disadvantage is that small inaccuracies per step can become large. The actual number of steps that are needed for a fixed step size $\Delta\lambda = 10^{-8}$ can go up to a billion for these runs. Inaccuracies of the order of the machine precision 10^{-16} for the variable type DOUBLE can add up and have noticeable effects. Altogether reasonable values for a fixed step size are above $\Delta\lambda = 10^{-9}$.

One advantage concerning accuracy is the fact that all metric quantities are calculated by analytic formulas. In real applications the metric data is normally interpolated from the underlying grid which gives additional uncertainties.

As a summary the outcome of convergence tests with several combinations of fixed step size $\Delta\lambda$ and ρ_0 are shown in table 2.1. One observation is that the

Figure 2.1: Convergence plots for three different values of $\Delta\lambda$. The differences of the interpolated integration paths are plotted as $16\,(f_{2\Delta} - f_{\Delta})$ (blue dashed) and $f_{4\Delta} - f_{2\Delta}$ (red solid). All integrations were started at $\rho_0 = 10^{-3}$.

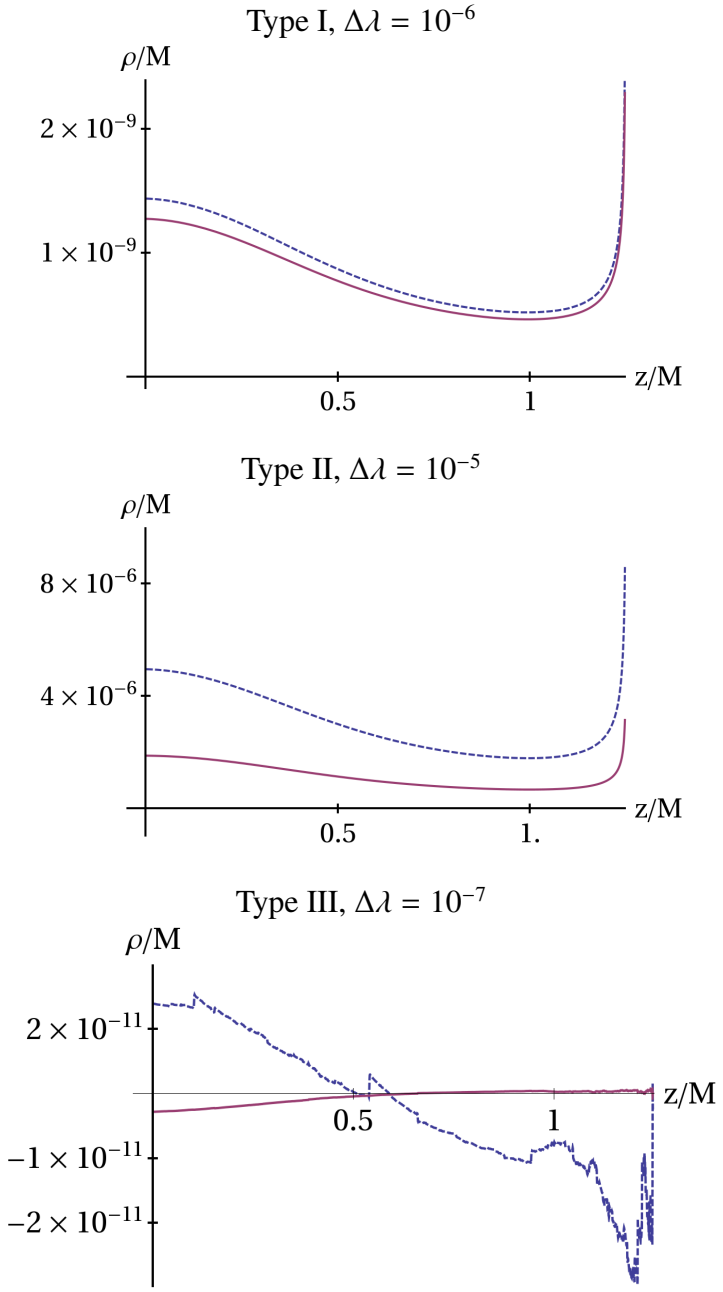

Table 2.1: Results of convergence tests for several values of the finest resolution $\Delta\lambda$ and the size of the first step ρ_0. The runs are either non-convergent or with order of convergence lower than 3 (-), or convergent to a given order (given as number), or accuracy limited, that means the differences in the paths are only limited by the overall precision of the variables that are used (+).

$\Delta\lambda$	$\rho_0 =$	.1	.01	.005	.002	.001	.0005	.0002	.0001
10^{-2}		3.8	-	-	-	-	-	-	-
10^{-3}		4	-	-	-	-	-	-	-
10^{-4}		+	3.8	3.3	-	-	-	-	-
10^{-5}		+	4	4	3.6	-	-	-	-
10^{-6}		+	+	+	+	3.8	3.3	-	-
10^{-7}		+	+	+	+	+	3.6	3.6	-
10^{-8}		+	+	+	+	+	+	+	3.6/+

three types that were explained above can indeed be mapped to three regions that depend on the finest resolution that was chosen. Curves starting nearer to the axis (smaller ρ_0) need higher resolution (smaller step size $\Delta\lambda$) and vice versa. The transition between these behaviours are related to the theoretical expected ratio $\rho_0^2/\Delta\lambda$. More specifically an integration starting with ρ_0 needs approximately $\Delta\lambda \lesssim \rho_0^2$ to get the expected 4^{th}-order convergence. Somewhat surprising is the small region of convergence, it is only up to one magnitude in both directions.

2.2.4 Adaptive Step Size

The previous section has shown the need for an adaptive step size algorithm. The code is able to use two kinds of adaptivity. The first deals with the problem near to the axis that is the main hindrance against convergence. The other diminishes the effect of a large conformal factor ψ that occurs near to a puncture.

Some details are given for both of the adaptivities. To overcome the problem near the z-axis the step size is suppressed by a factor of ρ^2. More precisely the step size is computed as

$$\Delta\lambda = C_\rho \rho^2 \tag{2.22}$$

where the prefactor C_ρ typically ranged from 10^{-2} to 10^{-6} depending on the problem. As an example figure 2.2 shows the difference between the adaptive and the

Figure 2.2: Differences between a run with fixed step size and three runs with adaptive step size algorithm. The prefactors for the adaptive method are $C_\rho = 0.1$ (blue solid), $C_\rho = 0.01$ (red dashed) and $C_\rho = 0.001$ (brown dotted). Upper picture: $\Delta\lambda_{fixed} = 10^{-6}$ and $\rho_0 = 10^{-3}$. Lower picture: $\Delta\lambda_{fixed} = 10^{-8}$ and $\rho_0 = 10^{-4}$. The red and brown curves lie on top of each other. Both are within 10^{-11} to the curve of fixed step size.

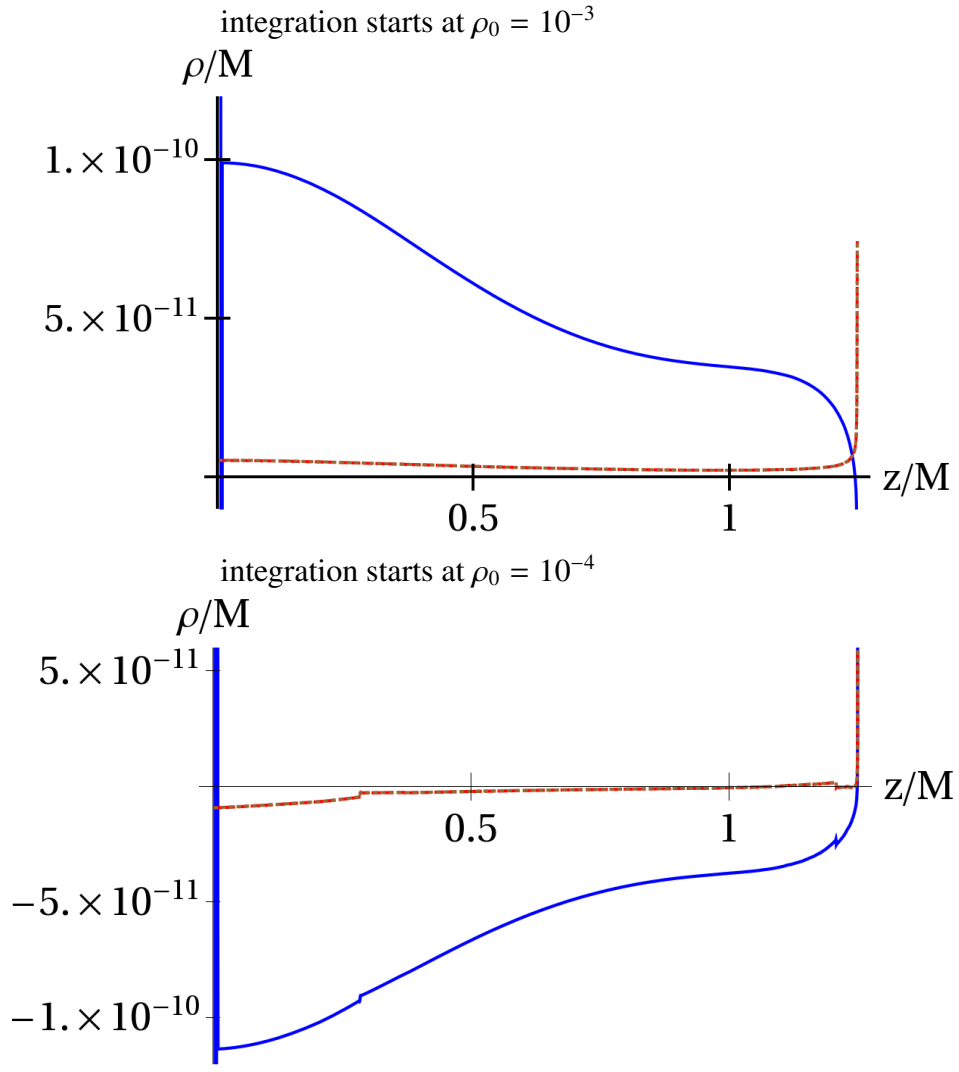

fixed step size method with two starting values $\rho_0 = 10^{-3}$ and $\rho_0 = 10^{-4}$. For both starting values the figure shows a small deviation for the coarsest adaptive method and a nearly identical even smaller difference for the finer methods. These differences of some 10^{-11} have to be compared against those in the diagram at the top of figure 2.1 where the differences of the fixed step sizes against each other are around 10^{-9}. Thus when using the adaptive step size control to cover small ρ, the curves do not change significantly. Moreover as an additional benefit the actual number of steps that have to be computed is reduced by a factor of 10 000 and more.[1]

Another source of inaccuracy appears when the integration comes near to a puncture. It is mostly of no importance but can become dominant under certain circumstances. Close to a puncture the conformal factor ψ is proportional to $1/r$, with r being the distance to the singularity. The derivatives of the integration variables in equation (2.12) are proportional to ψ^{-4} such that the integration slows down proportional to r^4. Normally this is not an issue because surfaces will not come near to either puncture. But for the runs with small separation the effect was noticeable. In addition to other adaptions the step size was scaled by ψ^4 in this instance.

Having established the main problems of the equations the actual runs were done with an adaptive step size method that will keep $\Delta\lambda$ proportional to ρ^2 and scales by ψ^4. Because of the adaptivity there is no clear rule for convergence, though. The resulting curves were compared against the runs with very small fixed step sizes and the differences of the ρ-coordinate are at the limit of 10^{-12} that was established before.

The previous sections have explained some specific issues that come with the differential equations given in (2.12) and (2.13). They were addressed by a suitable choice of variables and implementing an adaptive step size algorithm. It is left to explain the overall solution method that is quite common for these type of problems.

[1] For example compare runs with $\rho_0 = 0.005$: The reasonable fixed step size of 10^{-8} needed 1.6×10^9 steps compared to 17000 for the equivalently accurate adaptive method.

2.2.5 The Shooting Method

The differential equations (2.12) can be integrated starting from any point z_0 on the axis. But only if the curve turns back to the axis with the correct boundary conditions (2.13) an extremal surface is found (see figure 2.3).

The method of choice is the shooting method: the integration is started at one first guess z_0 and it is finished either when hitting the axis again or when leaving a given range. Depending on these outcomes the initial guess is changed and the integration is started again. After some repetitions of this 'trial and error' the boundary condition of the resulting curve at the free end should be satisfied within some acceptable error margin.

However for the equations that are considered here the integration towards the axis is not stable. Only the starting position of the *true solution* will give a curve that returns to the axis. Numerically this is not achievable, instead the curve will bend and either go off to infinity or head towards one of the black hole singularities (that are also images of infinity). See figure 2.5 or in [23] for an example.

Therefore a 'two-shot' method was used for this work (see figure 2.4). That means each trial surface actually consists of two separate parts that are started on the axis, enforcing the correct boundary conditions there. To get a single differentiable surface the two curves have to meet smoothly at some point. Analytically, for the true solution these two curves will be identical, numerically the curves will be close to each other in the middle region but will differ near to each starting point.[2]

Beside the two-shot method the literature [19] mentions a bracketing algorithm where the brackets are starting positions from where curves go off to infinity on one side and go to a singularity on the other side. Theses two behaviours are clearly separated and can also be used in the code. This is pursued in rare cases here, where the finding of MOTSs is done and checked by hand.

The two independent integration curves are called $C(\lambda)$ and $C'(\lambda')$. A prime shall indicate objects belonging to the second curve. Furthermore all values that

[2]The need for a two-shot method prevented the use of an out of the box PDE solver in MATHEMATICA .

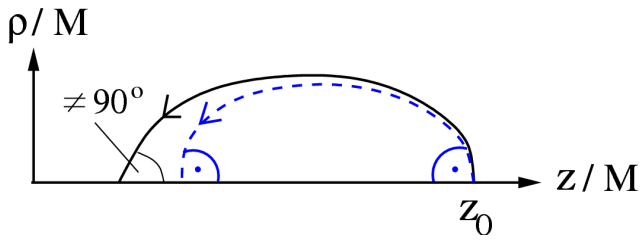

Figure 2.3: One shot method: start at one end and integrate to the axis. The second boundary condition must be correct.

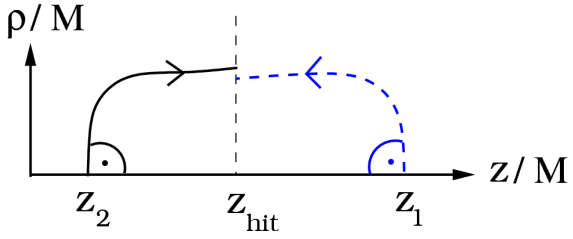

Figure 2.4: Two-shot method: start at two ends and integrate until the same z-value is reached. The boundary conditions on the axis are satisfied automatically. But need instead a smooth connection between the two curves at z_{hit}.

refer to the place where the two curves of integrations shall be compared are labeled by the subscript 'x' . Then demand from the analytical point of view

$$\begin{aligned} \rho(\lambda_x) &= \rho'(\lambda'_x), \\ z(\lambda_x) &= z'(\lambda'_x) \quad \text{and} \\ \alpha(\lambda_x) &= \alpha'(\lambda'_x) \pm \pi. \end{aligned} \tag{2.23}$$

The difference in the angles comes from the fact that the paths have opposite directions. From the numerical side the two curves will be considered equal when conditions (2.23) are fulfilled within certain margins. For monitoring the 'goodness of hit' the quadratic mean of the differences of the variables ρ and α is used:

$$g(C, C') = \sqrt{(\rho_x - \rho'_x)^2 + (\alpha_x - \alpha'_x - \pi)^2}\ . \tag{2.24}$$

The solution of the differential equation is found iteratively. The equations

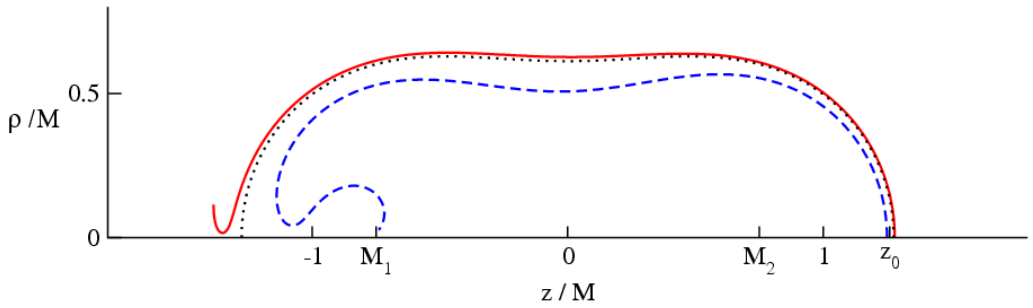

Figure 2.5: Two integrations starting at $z_0 = 1.25$ (red solid line) and $z_0 = 1.28$ (blue dashed line) in a Brill-Lindquist geometry with two black holes, marked with M_1 and M_2. The inner curve is going to the location of one black hole the outer one goes to infinity. The position of the marginally trapped surface is indicated by black dots.

(2.23) are monitored with respect to the measure (2.24) then one or both starting points are changed and the paths are integrated and compared again. Altogether a minimum of the merit-function $g(C, C')$ has to be found in the two-dimensional space of starting points z_0 and z_0'. This is done by a downhill-simplex minimization scheme as described in [57] chapter 10. It is not the fastest algorithm, there are other methods that make use of the expected quadratic behaviour of $g(C, C')$ near the solution point. But since it was not used in time-critical runs the speed was still acceptable.

It turns out that for this problem the minimization is fairly robust most of the time. That means the overall initial guesses for the two starting points do not have to be very good. This behavior is not maintained in some obvious circumstances. The first being setups where the apparent horizon jumps from two separate surfaces to a common one. For separations of the black holes that are a little smaller than the critical value there does also exist an intermediate surface that will be close to the outermost marginally trapped surface (see 2.3.1) and of course the first guesses have to distinguish between these two solutions. A second kind of problem arises for small separations of the black holes. Some runs have black holes at $z = \pm 0.001$ or less and their individual marginally trapped surfaces start at $|z_0| < 10^{-5}$. For these small separations the variation of start points has to be very small. Moreover in these cases the intermediate extremal surface is close to

the outer starting point of the inner MOTS. So both shooting positions have to be varied very carefully in order to get the correct surface.

For these cases the code had often to be tuned by hand or at least it had to be started with good initial guesses. In the case of series of MOTSs of black holes with varying separations these guesses were retrieved from a fitting function that depends on the distance of the two black holes. This fit was produced from a smaller number of prior runs. In the problematic cases discussed above a square root plus a polynomial of degree up to five was used as a fitting function.

2.3 Properties of MOTSs in Axial Symmetry

Already in an axial symmetric space-times many features of apparent horizons or marginally trapped surfaces in general can be explained. In this section the following points are discussed. An apparent horizon as the outermost MOTS can jump in a numerical simulation. The test scenario is a series of decreasing distances between two black holes in a Brill-Lindquist metric. For two holes far away each one exhibits a single MOTS and together they form the apparent horizon. Once below a critical distance a_{crit} one additional MOTS appears that surrounds both black holes outside of the individual MOTSs. This work shows numerical values for a_{crit} that were computed to high precision.

Furthermore it is examined whether for two black holes the inner MOTS will overlap when the black holes are close to each other. It is shown that at very small distances there is no overlap and the behaviour of the innermost point suggests that this behaviour will not change even for smaller separations: in the previous section the fit of the starting position needed a square root of the distance, that means the separation between the MOTSs reduces less than linear with the distance. Because the overlap was already shown in the literature for a short inspiral scenario [13] the question will also be mainly addressed for the general three-dimensional case and cases with extrinsic curvature in the later chapter about overlapping marginally trapped surfaces.

In the case of three (or more) black holes there indeed may exist overlapping

MOTSs. It will be shown and explained in the following chapter 3.3 how minimal surfaces can naturally overlap in these configurations.

2.3.1 The Near Distance

Two black holes with only a small separation give rise to basic questions. What happens to the inner marginally trapped surfaces, what happens to the intermediate extremal surface? Do these surfaces overlap? At least for the axisymmetric case of two equal mass black holes in a slicing of time symmetry the last question can be negated. Also the intermediate extremal surfaces show no unexpected behaviour, it nestles tightly to the inner marginally trapped surfaces.

The four extremal surfaces of the two equal mass black hole space-time were found for distances in the range of $a = 2$ down to $a = 10^{-4}$. The emphasis is on the small distances. Four samples are drawn in figure 2.6 as typical outcomes of MOTSs with decreasing distance of the black holes. For all these plots the Brill-Lindquist metric of equations (2.1) and (2.2) with equal masses $m_1 = m_2 = 1$ was used.

It will now be stated clearly what the general behaviour of marginally outer trapped surfaces around two black holes in a space-time of time-symmetry is. The different stages are shown in figure 2.6.

If the separation is large then there is one marginally trapped surface around each puncture, together they form the apparent horizon (see the upper left picture). Once the distance reduces below a critical value (see 2.3.2) two additional surfaces form outside of them, they are here called the outermost and the intermediate surface respectively. The latter represents a locally maximal surface. Now the single outermost is the apparent horizon, the intermediate surface wanders from this outer MOTS towards the inner MOTSs. For the distance $a = 0.5$ in the lower left picture the intermediate surface is now already very close to the inner ones but it never touches them. On the other hand the latter are still almost circles that do not touch. For $a = 0.04$ the apparent horizon has the shape very near to the one that comes from one single black hole with the composite mass of both black holes (see the lower right panel). The shape of the inner MOTSs remains

Figure 2.6: Series of MOTSs with decreasing distance between two black holes. Each surface is obtained by rotating the line around the horizontal z-axis.

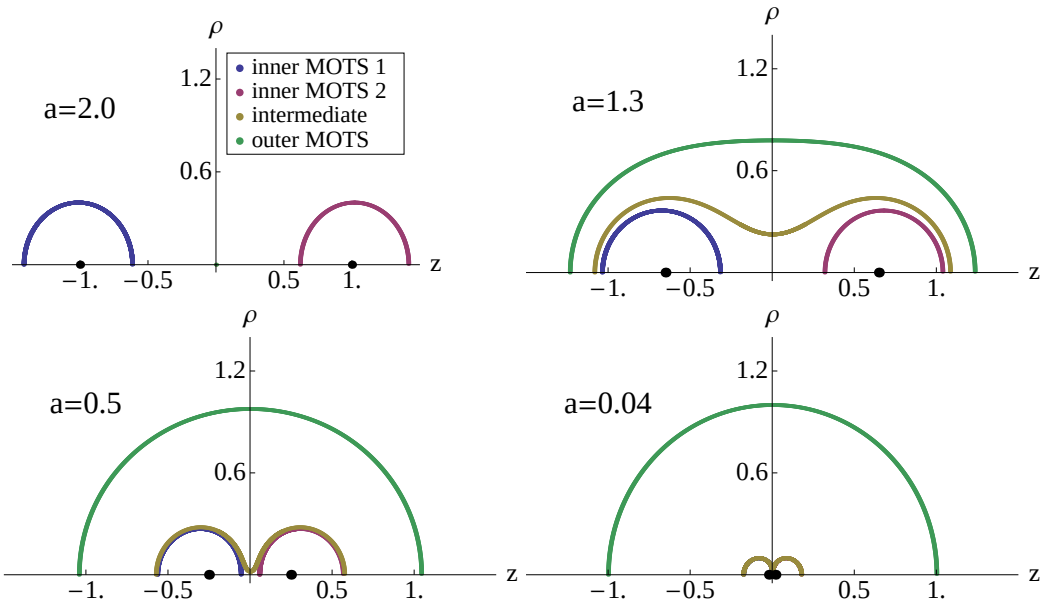

fairly spherical but their centers are considerably different from the black hole positions. At this resolution the intermediate surface is indistinguishable from the inner MOTSs, but we will see in the next example that they do not touch each other.

In figure 2.7 the inner region close to the origin is shown for the distance $a = 0.0001$ of the black holes. The upper picture shows the overall outline of the three surfaces, where it can be seen how close the curves are in almost the entire domain. To gain overview the axes were deformed. With the proper aspect ratio and with zoom into the region near the origin in the lower panel it is visible how close the intermediate surface comes to the z-axis. This surface is an example where a star-shaped representation of the surface (see 1.4) would fail.

These curves were found with an adaptive step size method to account for the very small values of ρ and the small distance to the punctures. Although the integration shows no signs of instability it is not possible to show convergence – because the adaptivity has no clear meaning of doubling the step size.

Figure 2.7: Zoom into inner MOTSs for $a = 0.0001$ near to the origin, *upper*: overview far away from the axis, *lower*: behaviour near to the axis.

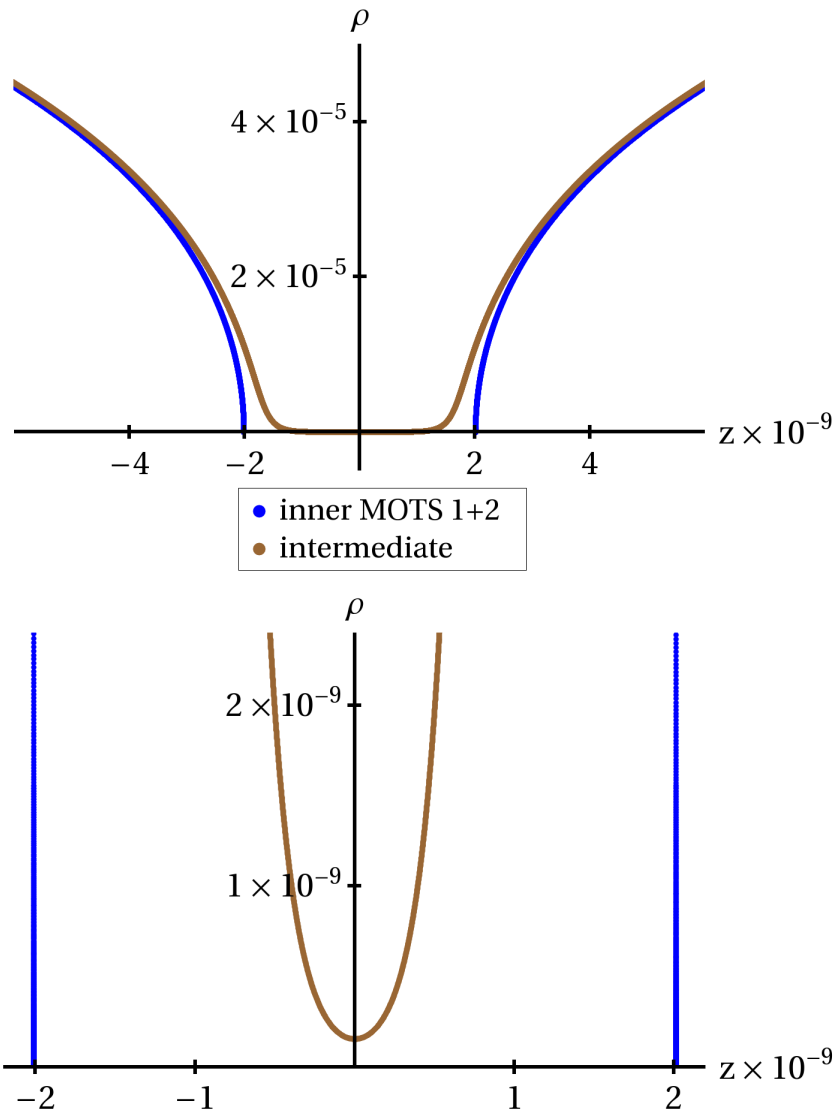

Table 2.2: Results and methods to find the critical distance in an equal mass two black hole setup.

reference	a_{crit}/M	remark
Brill, Lindquist [20]	$1.52 - 1.56$	search for 1/(2a)
Čadež [23]	1.534 ± 0.002	using $\alpha = 0$ at $z = 0$
Kemball, Bishop [42]	1.53	using spectral expansion
Alcubierre et al. [3]	1.532	search range of distances
Bishop [18]	1.45	search for 1/a
Bishop [19]	1.53	search range of distances
Baumgarte et al. [16]	1.53	search a/2
Lin, Novak [46]	1.532	spectral
Shoemaker et al. [63]	1.535	level flow
this work	$1.532\,394\,856\,480\,1 \pm 10^{-13}$	using $\alpha = 0$ at $z = 0$ + fit

2.3.2 The Critical Distance

It is a remarkable feature of the apparent horizon around two black holes that once they come near together a new MOTS outside of the individual trapped surfaces appears. This jump can not happen for the slices through the event horizon.[3] In numerical simulations the onset of a common horizon marks the time of merger. Some research was therefore focused on finding the correct time of appearance. One example is 'horizon pretracking' (see [61], [60] and also [63]).

For axial symmetric space-times the following typical scenario and setup was examined. The two black holes are described by a Brill-Lindquist metric in isotropic coordinates as in equations (2.1) and (2.2) with masses $m_1 = m_2 = 1$. The two punctures are located on the z-axis symmetrically around zero at $\pm a/2$. The critical distances that were computed by other groups are listed in table 2.2.

The critical value a_{crit} at which the common horizon forms can be found in several ways. The obvious method is to let the finder of MOTSs run for a range of distances and decide whether a common horizon was found or not. Čadež used the reflection symmetry at $z = 0$ that forces the curve to be parallel to the z-axis.

[3] Although Thierfelder [66, 67, 68] found that slices exist where a new part of the event horizon appears between three black holes that is not connected to parts of the event horizon that exist in *earlier* time slices. Only later they combine to one single object. Compare also the collapse of a shell of dust, where an event horizon forms in flat space.

Figure 2.8: Sketch of five integration curves for a space-time with two black holes that are near the critical distance. *Left panel*: For $a < a_{crit}$ the blue solid lines (curve 4 is the outermost MOTS and curve 2 is the intermediate extremal surface) hit the $z = 0$ line perpendicular, other integration curves (black dashed) do not. *Right panel*: The angle α between the curve and the z-axis at $z = 0$. The two extremal surfaces correspond to zeros of this function. For $a = a_{crit}$ exactly one root is found.

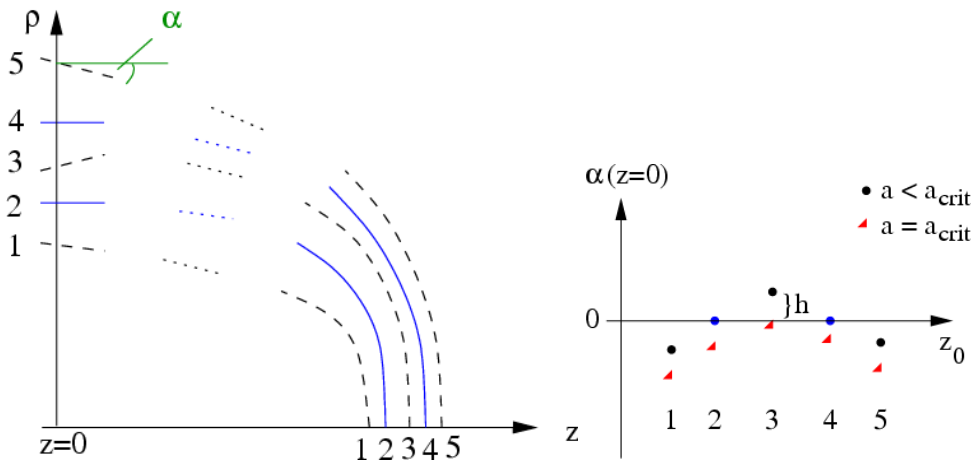

In his earlier work Bishop [18] showed plots of starting locations vs. a^{-1} and mentioned that a_{crit} can be deduced from these plots.

In this work a refinement of the last two ideas was developed. The additional knowledge is used that an intermediate MOTS exists that is close to the outermost one. Therefore, having reflection symmetry around $z = 0$, there are two nearby zeros[4] in the function $\alpha = \arctan(\mathrm{d}\rho/\mathrm{d}z)$ evaluated at $z = 0$. This idea is captured in figure 2.8. For $a \leq a_{crit}$ the corresponding function $g(z_0; a) := \alpha(z_0; a)|_{z=0}$ has two zeros. On the other hand, when the distance between the black holes exceeds the critical limit, the integrations will not hit the $z = 0$ line perpendicular, therefore $g(z_0; a)$ has no roots. Finally in the transitional point when $a = a_{crit}$ the function $g(z_0; a)$ has exactly one root.

To be concrete the critical value was found as follows. For several distances a approximations of the functions $g(z_0; a)$ was determined by fitting $\alpha(z_0; a)|_{z=0}$

[4]There are other zeros for the inner MOTSs, but these are of no concern here.

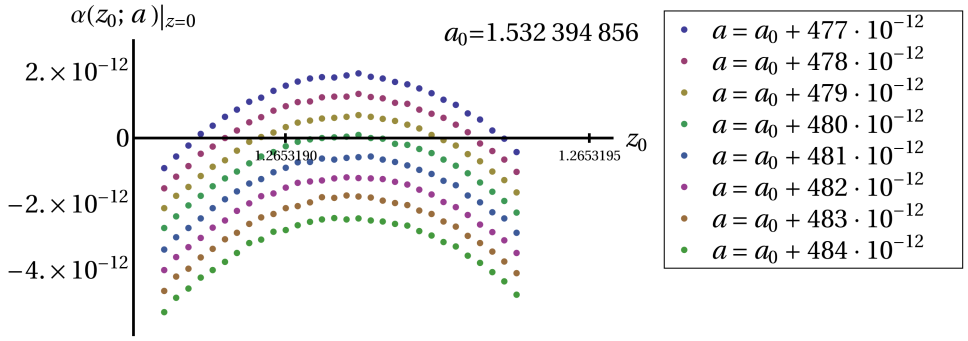

Figure 2.9: Angle of integration curves at $z = 0$ as function of starting position z_0. Depending on the separation a of the black holes the lines either do or do not cross zero.

in a suitable range of z_0. This is easily implemented since the code uses α as variable. One typical outcome for several values of a is shown in figure 2.9. The fitting function $g_{fit}(z_0; a)$ was found to be almost quadratic in z_0. The mean square difference of the computed values and the fit give an estimate of the accuracy of integration. The next step was to obtain the maxima (heights) $h(a)$ of each curve by determination of the extremum of the quadratic fit. The critical distance will then be the zero of the maxima $h(a)$. Since the maxima $h(a)$ follow to good agreement a linear behaviour in a a linear fit $h_{fit}(a)$ was done. The final value a_{crit} is then computed as the root of the linear function $h_{fit}(a)$. The result for the critical distance for a common horizon of two equal mass black holes was found to be

$$a_{crit} = 1.532\,394\,856\,480\,1 \pm 10^{-13} M \,. \tag{2.25}$$

The error of the critical distance is somewhat hard to measure. From a theoretical point of view the error of the above method is far less than the one that is stated in (2.25). This is because the uncertainties of the parameters that come out of the fitting routines are suppressed by the inverse square root of the number of points that were used, which can be made quite large. Instead the dominant uncertainty has to be extracted from variations of the integration.

To get a hold on the integration error the value a_{crit} was determined for several

Table 2.3: The critical distances computed with several prefactors of the adaptive step size algorithm. The integration shows fluctuations that are captured by the expression in the last column.

C_ρ	a_{crit}/M	$\sqrt{\frac{1}{n}\sum_i \left(g_i(z_0;a) - g_{fit}(z_0;a)\right)^2} \times 10^{-13}/M$
10^{-2}	1.532 394 856 744 588	0.220
10^{-3}	1.532 394 856 480 131	0.164
10^{-4}	1.532 394 856 480 098	0.281
10^{-5}	1.532 394 856 480 087	0.760
10^{-6}	1.532 394 856 480 236	2.236

runs that differ in the pre-factor C_ρ of the adaptive step size method (see section 2.2.4). For each one the root mean square differences to the fitted curves were computed. The results can be seen in table 2.3.2: Although the error for $C_\rho = 10^{-2}$ seems to be as small as the others there is a relatively large discrepancy in the actual value a_{crit} that shows that the integration is not accurate enough. $C_\rho = 10^{-3}$ has the lowest mean square difference, for smaller values of the step size the integration collects other sources of errors. But beside the variation of the integration curves there is no clear indication of what pre-factor should be taken. Therefore the differences of the critical distances a_{crit} between the runs for $C_\rho = 10^{-3}$, 10^{-4} and 10^{-5} were taken as estimate of the overall error. It was rounded up to be 10^{-13}.

The foregoing chapter has described the implementation of a finder of marginally trapped surfaces in axisymmetric Brill-Lindquist data. The code uses an adaptive Runge-Kutta method of fourth order to integrate a geodesic which will give the outline of the surface. The routine can use a two-shot algorithm driven by a downhill simplex minimization scheme. The overall accuracy was seen at the example of the critical distance of two black holes, where a common horizon forms. The next chapter will bring another application for overlapping marginally trapped surfaces.

Chapter 3

Overlapping Marginally Trapped Surfaces

Marginally outer trapped surfaces (MOTSs) are geometric objects inside the numerically evolved time slice. They are of interest in the general context of black holes where they approximate the location of event horizons. In this chapter it is examined under which conditions MOTSs can overlap. The intersection of MOTSs is studied both numerically and analytically. It is found that MOTSs can overlap in space-times with three bodies. The possibility of overlapping MOTSs for two black holes is described by using embedding diagrams. The next section will give a summary of previous work on the topic.

3.1 Knowledge About MOTSs

MOTSs and Minimal Surfaces Revisited There is no proof that marginally trapped surfaces can not overlap. Yet the scientific community had assumed so.[1] Thus it came to some surprise for those who first encountered intersecting MOTSs. One reason is the close relationship between MOTSs and minimal surfaces. The differential equation for minimal surfaces is in fact equation (1.15) for the expansion but without the extrinsic curvature terms. An intuitive picture is that there can

[1] Thornburg made a comment in [71] that MOTSs do not cross, but without explanation.

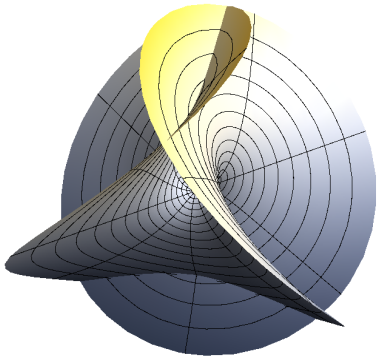

Figure 3.1: The inner part of the Enneper surface.

be no corners in minimal surfaces except those that are enforced by boundaries. Any corner can be smoothed by a little arc that has less area. It was not clear what the extrinsic curvature can add to it, but since it is smooth no change was expected in principle.[2] But in fact minimal surfaces can intersect themselves. An example is Enneper's surface, its inner part is shown in figure 3.1 [74]. The reason is that the minimal surface equation $\nabla_i s^i = 0$ is a local condition like Einstein's equation in general relativity. Both do not determine the global behaviour of the solution. Thus the corner is made by different regions on the manifold. At pure corners without a clear normal the partial differential equation would be ill-defined.

Previous Results on Overlapping and Outermost MOTS In a series of papers [5, 6, 7, 44] Andersson and others developed a good understanding of stability of MOTSs. This includes the analysis of small perturbations and short evolutions in time. As a result they have shown in [7] that when two MOTSs come sufficiently close together an outer surrounding MOTS must exist. This can be restated as:

[2]The flow method for apparent horizon finding is based on methods that were used for minimal surfaces. There is no sign that extrinsic curvature changes the basic behaviour of the flow, yet there is no rigorous proof.

when marginally outer trapped surfaces touch or overlap then they can not be outermost. The proof is based on the one hand on an existence theorem for an outer MOTS given a surface with expansion equal to and smaller than zero under quite general conditions. On the other hand they are able to construct such a trapped surface by establishing a suitable tube-like link between the marginally trapped surfaces that almost touch. In this respect the examples that are shown or mentioned in this work agree with the theoretical prediction: in all cases of overlap an outer MOTS is present.

There are a few examples in the literature where intersecting marginally trapped surfaces are shown. The work considered here are by Schnetter [59], and Szilágyi et al. [65]. Furthermore there is work published by Metzger [49] who found overlapping horizons with three black holes.

In [59] the author uses the multiple black hole initial data that was proposed in [48]. This initial data is made by overlaying two Kerr black holes followed by solving the Hamiltonian constraints. In the original paper on the initial data the authors considered binary black holes whose masses are small compared to their coordinate separation. The near distance in Schnetter's paper might exhibit problems that could change the overlapping MOTSs.

The more interesting case is the binary black hole evolution that was carried out by Szilágyi and co-workers. It uses the initial data and run parameters from a series by Baker et al. [13]. Their code is based on the harmonic gauge with excision. They show overlapping inner horizons. Besides the intersection there is another interesting feature: the common outer horizon seems to start at the rim of the still existing inner horizons. Maybe the tightness is only a coordinate effect, but also it raises the question where the third intermediate (kind of maximal) surface could start.

3.2 Search for Overlapping Surfaces

It was shown that overlapping marginally trapped surfaces can be expected in numerical simulations. It thus is surprising that in the simulations that were performed for this work it was only with three black holes that intersecting surfaces

were found. Three cases are considered: the two black hole axisymmetric setup from the previous chapter, a two black hole merger scenario evolved with the BAM code ([21, 22] and see 3.2.2) and a three black hole axisymmetric setup. Subsequently the reason for the different outcomes between these runs and those of other groups is examined.

3.2.1 Two Axisymmetric Near Black Holes Revisited

The setup of two black holes in Brill Lindquist initial data was explained in section 2.2. Therefore only a short summary is given. The program is able to find MOTSs in axisymmetric and time-symmetric hypersurfaces. It integrates curves with a Runge-Kutta method using an adaptive step size. The correct initial data is found iteratively with a shooting method. In the special case that is considered here the iteration was often run by hand because the initial positions of curves should be varied only in a very small range. The implementation of the downhill simplex minimization method also tries some points that are farther away and can thus be fooled by other minima.

The separation a of the black holes is changed down to $a = 0.0001$ and the MOTSs were found consistently. This distance is small compared to the separation $a \approx 1.53$ at which the two black holes have a common horizon (see 2.3.2). For $a = 0.0001$ the common horizon is nearly spherical, the ratio between the radius in the z- and the ρ-direction differs by only 4.13×10^{-9} from one. The result is shown in figures 3.2 and 3.3, the blue lines belong to the individual MOTSs around each puncture, the brown one is the intermediate surface that lies between these and the outermost MOTS. Looking at the off-centered position of the punctures it is remarkable that these inner MOTSs are only minimally distorted, the ratio between the diameters in ρ- and in z-direction is around 1.033.

In this example none of the surfaces overlap, but it is of course far from general because the extrinsic curvature is zero. The additional terms can supply changes to the geometry and thus to the surfaces. Furthermore one numerical example is not a proof for arbitrary distances, for even smaller separations the surfaces might overlap. However, in natural units given by the mass the black holes are

Figure 3.2: The inner MOTSs of two black holes with distance $a = 0.0001$. The plot is distorted in order to see both the small separation and the behaviour away from the z-axis.

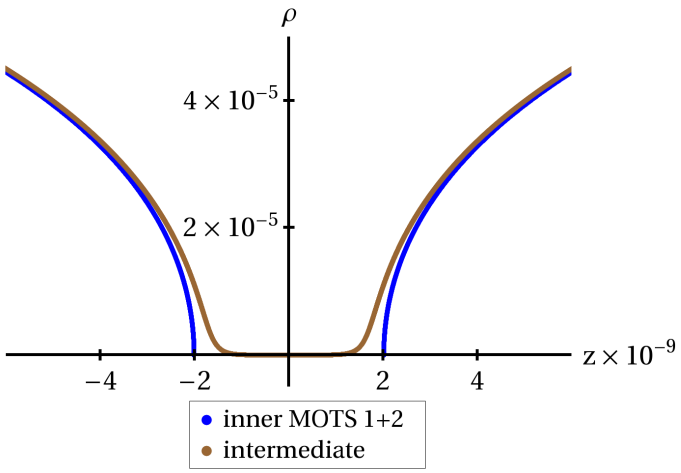

Figure 3.3: The individual inner MOTSs of two black holes with distance $a = 0.0001$. The plot shows how circular the surfaces are.

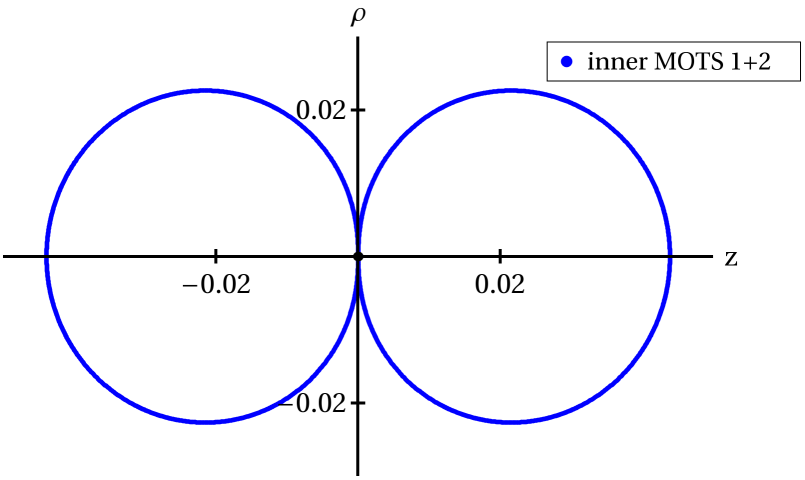

already very close to each other, no further change is expected when going nearer. In appendix D a short analytical setup is considered for the axial symmetric case. But in the end no strict result is found that forbids these MOTSs from overlapping. The next section will be more general, it introduces black hole evolutions that have non-vanishing extrinsic curvature.

3.2.2 The BAM Apparent Horizon Finder

The BAM program [21, 22] is a fully general relativistic code that is capable of simulating multiple black holes before and through merger. It is a finite difference code that uses a Cartesian grid with adaptive mesh refinement. Evolutions are performed with the BSSN system with the gamma-driver shift and 1 + log-slicing gauge conditions (see 1.2).

The apparent horizon finder uses the fast flow method [35] already explained in the introduction 1.4. The finder was coded by José Antonio González based on a previous routine that was implemented by Miguel Alcubierre in Fortran. The basic version was thoroughly tested with several orders of their spectral expansion and various numbers of points on the grid in [3].

Several missing features were established that were needed for this study. First not only the outermost trapped surface can be found but also the inner ones. Secondly the location for each surface is saved and used as the initial guess of the next search. Additionally the time periods throughout the evolution at which a specific surface is searched for can be given as input. Specifying the search window prevents the apparent horizon finder from costly searches for the common horizon long before merger; the disadvantage being that the time of merger should be roughly known beforehand.

The accuracy of the horizon finder can be selected in several ways. One aspect is the maximal degree $LMAX$ of the spherical harmonics that represent the surface. Its value was mostly kept at $LMAX = 10$, since tests with higher orders gave no better results. During the solution the expansion is calculated at specific positions given by a regular angular grid, the grid size is normally around $n_\theta \times n_\phi = 36 \times 72$ but was increased up to 100×200 based on the following logic. The spectral

expansion of order $LMAX$ has angular distributions up to $\cos(LMAX\ \pi)$. Four points per cycle are needed at least, a better resolution can use eight or ten points. Thus $10 \times LMAX$ points in ϕ-direction should be an adequate number.

One other parameter is the stopping criteria of the flow. For each surface the mass is calculated from its area as $mass = \sqrt{area/(16\pi)}$. When the change of the mass between steps drops below a certain tolerance, the flow has converged. Compared to standard parameters of the code, this tolerance was decreased from 10^{-3} to 10^{-10}.

3.2.3 Equal Mass Merger and MOTSs

In this section the results are shown that were produced with the BAM code. The initial data was chosen to be similar to the simulations of [65] that were taken from the series in [13]. Two non-spinning black holes with equal mass $M = 0.5$ are set in a point-symmetric configuration with a distance of $d = 2M$ giving both of them momentum $P = 0.3$ in the direction of circular motion. That will result in a merger of the two objects after about one orbit. The modified apparent horizon finder tracks both the individual marginally outer trapped surfaces and the common horizon that forms after about $13.2M$.

The inner MOTSs could be tracked until around $19.1M$ (that is $6M$ after merger), the separation of the black holes is then around $0.156M$. The MOTSs show no sign of overlap. Two representative plots are shown in figure 3.4. The configurations was run with several resolutions of the underlying grid. Higher resolutions lead to a longer time where the inner MOTSs can be found. The highest resolution run that is shown here has a resolution of the innermost mesh refinement box of $dx = 0.008M$. Besides not finding the MOTSs at all, the inner MOTSs vary somewhat between resolutions. The tendency is to have larger surfaces with larger grid spacings. But for all runs the gap between these surfaces stays roughly the same, the shapes of the surfaces changes mostly on their more distant parts.

It is found that the full numerical simulation of an equal mass black holes merger using 1 + log slicing and Γ-driver shift condition in the BAM code does not produce overlapping marginally trapped surfaces. Although these surfaces

Figure 3.4: The individual inner and the outermost MOTSs from a simulation of two equal mass black holes. The three-dimensional output is cut in the $x-y-$plane to look into one half. *Upper*: The MOTSs at $t = 13.2M$ shortly after the common apparent horizon appeared. *Lower*: The MOTSs at $t = 19.1M$ the latest stage where all three could be tracked.

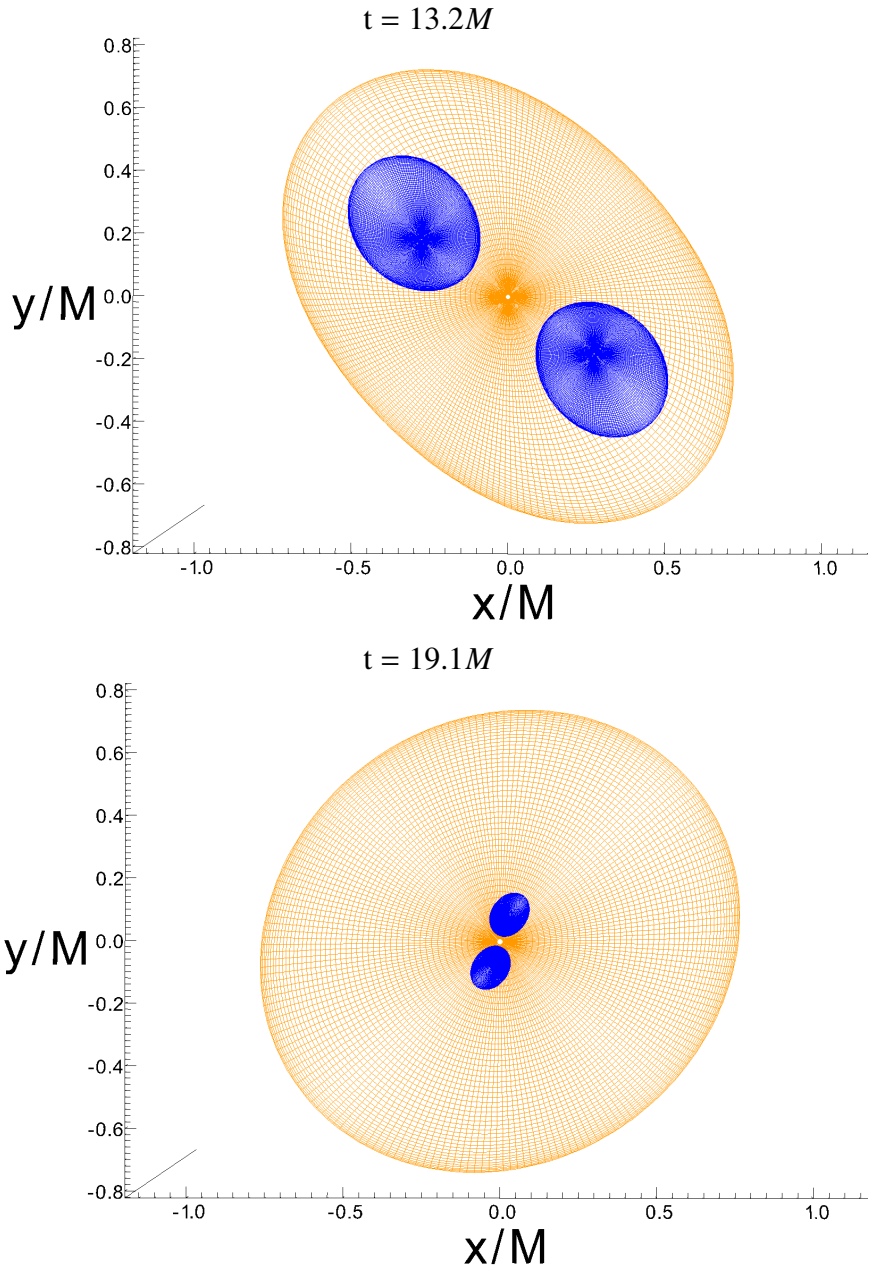

could not be tracked as far as in the axisymmetric case their general behaviour suggests that also at later times the surfaces stay separate: the surfaces approach each other more slowly than the punctures do.

3.3 Embedding Diagrams and Three Black Holes

It was shown in the previous sections that for two black holes both in axial symmetry and in a symmetric merger case no overlapping MOTSs were found. This stands in contrast to the findings of the other groups as explained in section 3.1. But already the three black hole setup changes everything. An intuitive way of understanding this is to visualize the black holes in an embedding diagram. In [49] Metzger showed an embedding diagram for understanding the three black hole case. Here the idea is broadened to use embedding diagrams for two black holes.

Embedding diagrams (see [51]) try to visualize the bending of the three- or even four-dimensional space with a manifold in lower dimensions. Normally this method is only applicable to symmetric space-times, where two or three dimensions of the original problem can be neglected. One famous example is the Schwarzschild space-time: depending on the coordinates that are used the resulting surface will resemble a wormhole or another kind of funnel or trumpet [36]. In isotropic coordinates these tubes even blow up near to the puncture and become flat again: this region is then another asymptotically flat end. Together with the 'normal' outer asymptotic end that includes spatial infinity and the tube-like connection they form a Brill-Lindquist wormhole topology. With every black hole in the space-time another wormhole can be constructed. Figure 3.5 shows an example with two black holes. The embedding diagrams have a suggestive meaning in the case of minimal surfaces. In the examples with an axial symmetric space-time at an instant of time-symmetry a reduction of four to two dimensions is possible. The third dimension is the unphysical one that is needed to visualize the curvature, points outside of the surface are no legal points in the corresponding real space. Through the reduction of dimensions a closed surface around a puncture is represented by a closed loop in the embedding diagram.

Figure 3.5: Embedding diagram with two and three black holes (*upper* and *lower* plot respectively) which have large separations. Marginally outer trapped surfaces are marked by red lines. From the top sheet each puncture is reached by crossing exactly one MOTS.

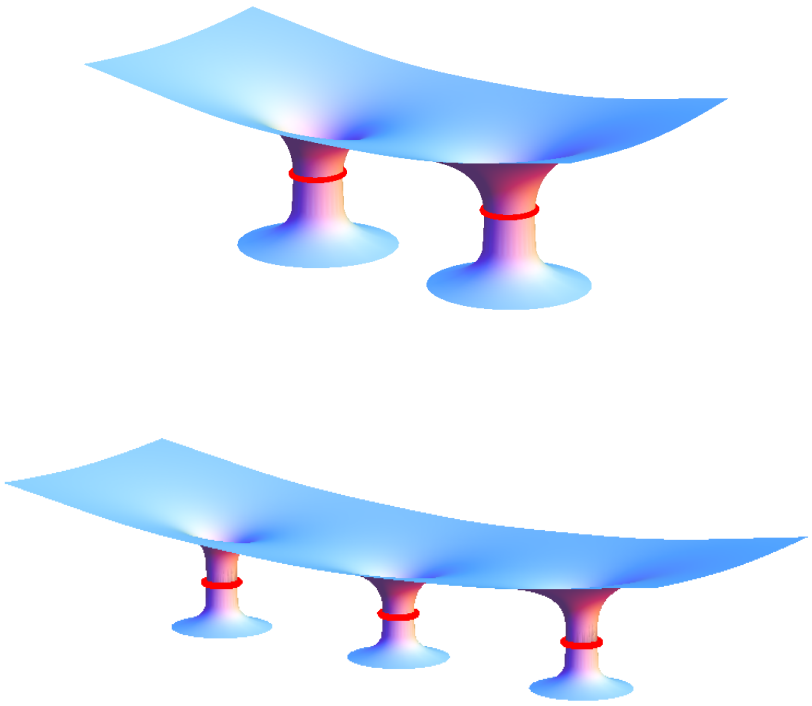

Figure 3.6: An embedding diagram with two black holes with small separation. Marginally trapped surfaces are marked by red lines. There is one common outer minimal surface and two individual MOTSs.

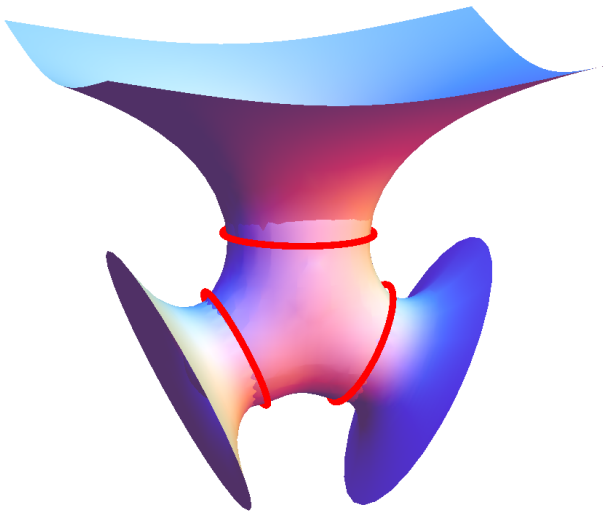

With these visualizations the outcomes of marginally trapped surfaces stated in the previous sections can be explained. For two or three black holes that are remote their asymptotic ends are well separated and do not interfere, that is illustrated in figure 3.5. On each wormhole there is one location of minimal diameter, this represents a surface of minimal area in the physical space. When the black holes are near, their wormholes lie inside the same gravitational well and only near to the punctures they separate again into individual flat ends. In this case another minimal surface forms that is outside of both inner minimal surfaces, outside means here nearer to the physical space-like infinity. This is visualized in figure 3.6. No intersection of the surfaces is needed.

In the next paragraphs the issue of overlapping MOTSs for three black holes will be considered. Two cases can be seen directly. First when the three black holes are aligned and have large separations, that is shown in the lower part of figure 3.5. As in the corresponding case for two black holes the minimal surfaces are well distinct, no other minimal surfaces are present. Also the '2+1' case in

Figure 3.7: An embedding diagram with three black holes that are close to each other. Two additional minimal surfaces exists (dashed red lines).

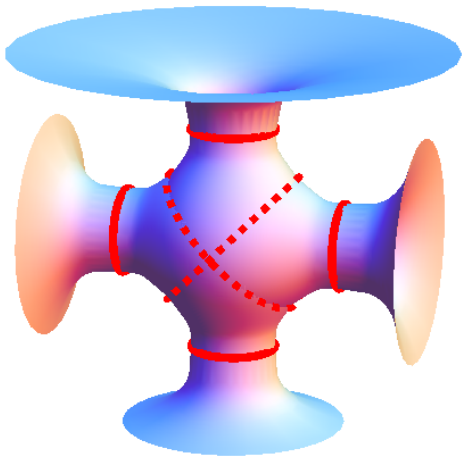

which two black holes are near whereas the third puncture is still far away does not give new insight: the minimal surfaces look like the two near case (figure 3.6) and the single black hole case respectively.

In figure 3.7 the embedding diagram for three black holes that are aligned near to each other is schematically shown. These geometries exhibit a new feature that will be addressed here, namely the arise of two additional minimal surfaces that are shown as dashed lines in the figure. They are formed from new topological possibilities that come with another puncture. The new MOTSs can not be smoothly deformed to one of the marginally trapped surfaces near to each puncture nor to the outermost MOTS.

The newly formed marginally trapped surfaces do intersect each other. The two intersections in the embedding diagram correspond to a closed line where the two spherical surfaces meet. So the three black hole geometry can naturally exhibit overlapping MOTSs in an instant of time-symmetry. Several remarks of the generality of this result will be given. From a topological point of view this crossing is inevitable. Assume a space-like hypersurface with three distinct black

holes called ‘A’, ‘B’ and ‘C’. Let S_1 be a surface that surrounds A and B but not C. Another surface S_2 that surrounds only B and C but not A must intersect S_1.

Another possibility concerns the idea that even the MOTSs near to the punctures might intersect with the newly formed MOTSs. But this is not the case. The reason can be found in [7] and references therein (also already rephrased in 3.1). The theorem states that given two MOTSs that almost touch each other then there must be a MOTS outside of them encompassing both. One idea is to switch the notion of inner and outer part near to one puncture, which can be thought of rotating figure 3.7 by 90 degrees to the left or to the right. Then the theorem states that the new outermost MOTS can not intersect with any of the other MOTSs, in particular not with those newly formed ones.

The newly developed minimal surfaces can also be visualized as a common horizon of two black holes where the third black is in the same gravitational well but still separate from both of them. Like the ‘2+1’ case considered above.

The embedding diagrams that are shown here are not computed from actual space-times. In fact only for a minority of metrics an embedding in three dimensions is possible. For example it is not even possible for the conformal metric of the Schwarzschild geometry although it exhibits spherical symmetry [51]. Schematic diagrams are produced to give possible visualizations of minimal surfaces.

These surfaces can indeed be found by the axisymmetric code described before in section 2.2. They are searched for in a setup where three black holes are aligned on the axis with the following parameters. The location on the z-axis of the black holes are $z_1 = -z_0,\ z_2 = 0, z_3 = z_0$ with z_0 ranging from 1.2 to 2.4. The masses were $m_1 = 2$, $m_2 = m_3 = 2\sqrt{2}$. All pictures look qualitatively equal, as representative the one with distance $a = 1.5$ is shown in figure 3.8.

Finally the case with two black holes is reconsidered; is it possible to have this overlapping surfaces too? An intuitive possibility is shown in the embedding diagram in figure 3.9. Two wormholes dominate the topology, but in-between a small bulb is created. This need not be an additional mass aggregation (although it could), it can also be due to the extrinsic curvature, i.e. the stretching of the spatial hypersurface in the four-dimensional continuum. This additional structure

Figure 3.8: The marginally outer trapped surfaces in axial symmetry for three black holes. Two MOTSs overlap.

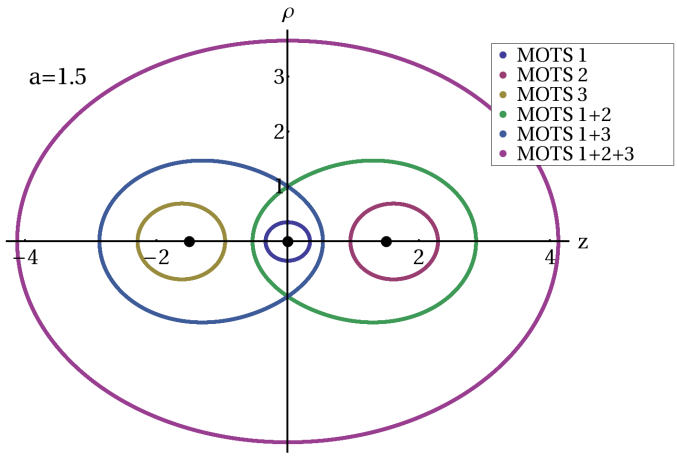

allows the existence of two locally minimal surfaces that overlap, although they are topologically equivalent to the individual minimal surfaces around each puncture. They have a larger coordinate position than the individual MOTS. This could be problematic if one wants to find the inner ones by a flow method starting with larger radii. The work of Szilágyi et al. [65] might suffer from this behaviour, at least it would be an explanation why their common horizon starts so close to the inner horizons.

3.4 Conclusion on Overlapping MOTSs

The forgoing sections have given an overview over overlapping MOTSs. It was explained that the own experiments failed to find these for two black holes, unlike examples from the literature. Visualizing the three black hole case with embedding diagrams helped in finding a plausible but not strict explanation why all these results can be correct. The appearance of an inflated region is proposed that can have the effect of another black hole.

Since the physical content of simulations by both BAM code and the AEI harmonic code is roughly the same, it is natural to search for differences coming

Figure 3.9: Embedding diagram with two black holes, the region between the punctures is inflated. MOTSs are marked by red lines, also overlapping MOTSs can be found (dashed). They are topologically equivalent to one surface at the puncture.

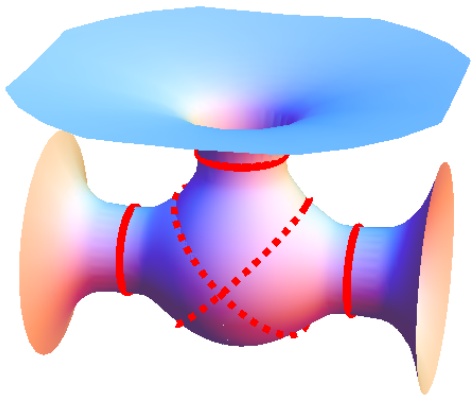

from the gauges. The AEI code uses the generalized harmonic gauge whereas the BAM code has the Gamma-driver shift and 1 + log condition. The latter has the possibility to flatten the spatial slice with a speed faster than light. In the case of Schnetter's example it is not possible to conclude any statement about the extrinsic curvature. Both algorithms that found an overlap use excision. The boundary conditions at the excision region might increase or disguise this problem by introducing large errors.

Overall overlapping marginally outer trapped surfaces are still not fully understood and open questions remain. The main problem in addressing them is that no code with harmonic gauge – maybe also with excision – was available to the author.

Chapter 4

Eigenvalues for Newton Solvers

4.1 Newton Method for PDEs

Over the years several direct methods were introduced to find the apparent horizon, see Čadež [23], Dykema [31]. Especially Thornburg [71] gives a thorough descriptions of the used notation and further references. The following notation and aspects about Newton solvers can be found in [28] and also in [39].

This section gives first a short introduction into solving partial differential equations by Newton methods together with an overview of the eigenvalue analysis. It is followed by a derivation of the explicit form of the expansion as a function of derivatives of the height function h. Then the expansion is perturbed by explicitly substituting $h + \mathrm{d}h$ for h. By taking the difference of the perturbed and the unperturbed expansion the Jacobian in the sense of (4.6) is recovered. Finally the eigenvalues of the iteration matrix, together with actual iterations for several goal functions are computed for simple examples and conclusions are drawn how to improve the radius of convergence for this kind of direct methods.

The apparent horizon and marginally outer trapped surfaces in general are defined by a vanishing expansion of outgoing null rays at every point. Within the framework of the 3+1 split the expansion of a closed 2-surface S in the spatial hypersurface can be calculated as (see chapter 1.3)

$$H(S) = \nabla_i s^i + K_{ij} s^i s^j - K \tag{4.1}$$

where s^i is the outward unit normal on S, K_{ij} is the extrinsic curvature and K its trace. This equation is a non-linear partial differential equation of elliptic type.

Elliptic partial differential equations can be solved by Newton solvers. There are several variants of Newton solvers but only a few are described here. A Newton solver takes an initial guess for the solution and solves the linearized problem for the difference vector. The result is used as an improved guess, that is again applied to the linear solver. After several iterations of these steps overall convergence to the solution of the full system can be reached. Although the Newton iterations can be shown to be quadratically convergent towards a solution their major drawback comes from their small region of convergence: already the initial guess has to be close to the final solution. Moreover getting the linear problem and finding its solution can be a computationally involved. In this thesis it is investigated how the change of the original problem by 'goal functions' might extend the range of good initial guesses. It is accompanied by the use of eigenvalues: At each step of the outer Newton iteration a linear problem has to be solved, this again is also often done by an indirect, iterative solver. This inner iteration loop exhibits an iteration matrix, its eigenvalues are the ones under consideration here. It is assumed that the maximal absolute eigenvalue indicates the convergence of the overall procedure. The above steps will be explained with the special case where the expansion H is given as function of the height function h.

In the case of root finding of a function of one variable Newton's method has a clear geometric meaning. Therefore parallel to the general outline an example will be shown that is based on the expansion in spherical symmetric Schwarzschild geometry. This is also helpful in the later section where this geometry is used as primary example.

The metric for Schwarzschild geometry in isotropic coordinates is

$$g_{ij} = (1 + \frac{m}{2r})^4 \delta_{ij}. \tag{4.2}$$

The expansion of a sphere of radius r around the center can be analytically computed as

$$H(r) = \frac{8r(2r - m)}{(2r + m)^3}. \tag{4.3}$$

Also the roots can analytically be found at $r_1 = m/2$, $r_2 = 0$ and $r_3 \to \infty$. Only r_1 will be considered the correct solution for the minimal surface. Note that $H(r)$ stands here for the above one-dimensional example, that is actually not even a partial differential equation anymore, whereas $H(h)$ will stand for the general problem with h characterizing a two-dimensional surface. Iterations are indicated by upper indices in parentheses.

The initial guess $r^{(0)}$ for the surface will in general not satisfy $H(r^{(0)}) = 0$. But starting from $r^{(0)}$ the local tangent with slope $\partial_r H(r^{(0)})$ is used as an approximation to the function. Finding the zero-crossing of the tangent needs the solution of the (here analytic) equation

$$\partial_r H(r^{(0)})\, \Delta r^{(0)} = -H(r^{(0)}) \tag{4.4}$$

for the correction $\Delta r^{(0)}$. The updated guess

$$r^{(1)} = r^{(0)} + \Delta r^{(0)} \tag{4.5}$$

will be nearer to the true solution r^* at least for purely convex or concave functions. More complicated functions will exhibit divergences or convergence to other solutions for certain ranges of its variable. This process can be iterated until suitable criteria are fulfilled. These first two steps are marked as $r_1^{(0)}$ and $r_1^{(1)}$ in diagram 4.1. Starting from $r_2^{(0)}$ the method leads to an unphysical negative radius for the next step, thus the simple Newton method will fail.

Note that one step of the Newton method in the full problem $H(h) = 0$ needs the solution of

$$\frac{\mathrm{d}H^{(i)}}{\mathrm{d}h}\, \mathrm{d}h^{(i)} = -H(h^{(i)}) \tag{4.6}$$

for the change $\mathrm{d}h$, followed by an update

$$h^{(i+1)} = h^{(i)} + \mathrm{d}h^{(i)} \tag{4.7}$$

of the surface. The term $\frac{\mathrm{d}H^{(0)}}{\mathrm{d}h}$ stands for the Jacobian of the functional $H(h)$. This nontrivial task is done with a solver for linear equations at each step of the New-

Figure 4.1: The expansion in spherical symmetric isotropic coordinates (blue), and two tangents showing the geometric meaning of the Newton method. Starting from $r_1^{(0)}$ the zero of the red tangent at $r_1^{(1)}$ is closer to the zero of the expansion. Starting from $r_2^{(0)}$ the brown dashed tangent has no meaningful root. The simple Newton method would fail, but a damped scheme still gives the right direction.

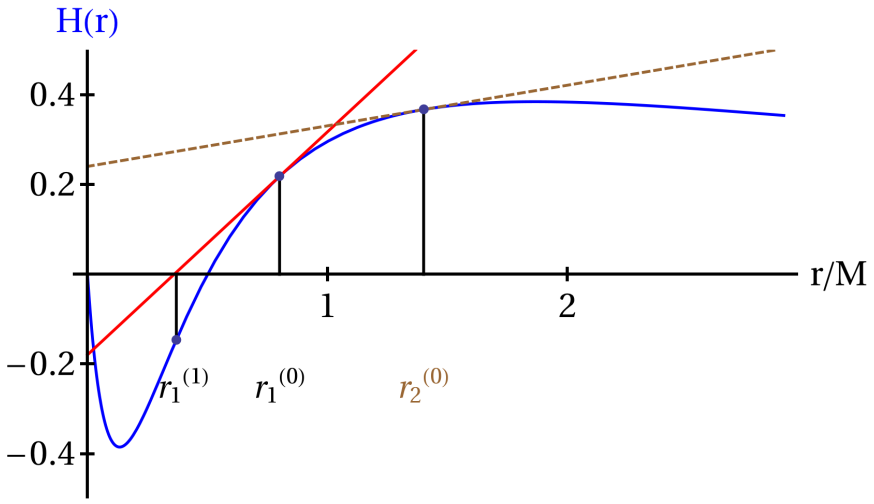

ton algorithm. If the latter uses a direct elimination method the whole algorithm is called a *direct Newton method* if otherwise an iterative solver for the linear problem is used it is called an *inexact Newton method* (nomenclature of Deuflhard [28]). Other classifications rely on the choice of norms for the conditions at each iteration. *Corrections based* methods use the displacement $\|\Delta h^{(i)}\|$, *residual based* methods use the norms in the function (or general operator) space $\|H(h^{(i)})\|$ to monitor the progress.

A distinction can be made between *local* and *global* Newton methods. The latter try to circumvent the small region of convergence by different techniques. Deuflhard mentions several of such 'globalization concepts'. But the criteria for application in each special case are hard to establish. Only the so-called Newton path as one general idea is considered here, it will lead to the 'residual based descent', that is a damped Newton iteration [53, 28].

The theory states that one Newton step gives a distinguished direction, but its length might be too large. The related theorem gives conditions for H under

which a path can be constructed from $x^{(0)}$ to the solution x^*. This *Newton path* will end either (i) at the 'nearest solution', (ii) at a critical point that has a singular Jacobian or (iii) at the boundary. Of these three possible outcomes, the last two are pitfalls that have to be dealt with. Unfortunately in the case of the expansion equation the necessary condition on H could not be shown by the author, and it seems unlikely that it can be shown at all. That is a major missing link to a rigorous statement about the eigenvalue method. On the other hand the numerical methods will not resemble a possible exact mathematical statement because finite sized step lengths are needed. More details about the prerequisites of the theorem are given in appendix E.

The behaviour of the Newton path is also observable in the example in figure 4.1, the correct solution would be found also from starting point $r_2^{(0)}$ when only the direction of the tangent is used for a small step. Below the minimum at $r_{min} = m(1 - \sqrt(3)/2) \approx 0.134$ the path is directed towards the boundary at zero and beyond the maximum $r_{max} = m(1 + \sqrt(3)/2) \approx 1.866$ the outer boundary at infinity is reached.

Both the problem with critical points and with the boundary will be addressed by *goal functions*. Consider for concreteness instead of $H(r) = 0$ the goal function $G = H(r)r^2 = 0$. It has the same zeros $r_1 = m/2$ and $r_2 = 0$ but the outer part is now convex. Any damped Newton step that starts at large radius will converge to the outer solution r_1 (see figure 4.2). In general the expansion can be multiplied by a positive expression that changes the critical points r_{min} and r_{max} and even the limit at infinity. Goal functions for operator equations in dimensions larger than one can not be found by visual inspection. Instead in this thesis the largest absolute eigenvalue of an iteration matrix for one inner step of the Newton method is proposed as an indicator.

The overall strategy will be as follows. First the expansion will be written as a sum of a perturbed and an unperturbed part, where the perturbation is given by a small change $\mathrm{d}h_1$ to the height function h. The difference will give direct access to the Jacobian $\frac{\mathrm{d}H}{\mathrm{d}h}$. The height function and its perturbation are given by a finite set of numbers such that the equation (4.6) becomes a set of linear equations. Then an inner linear solver treats these equations. A general theorem states that

Figure 4.2: The expansion in spherical symmetric isotropic coordinates (blue), and an alternative goal function with the same roots (dashed red).

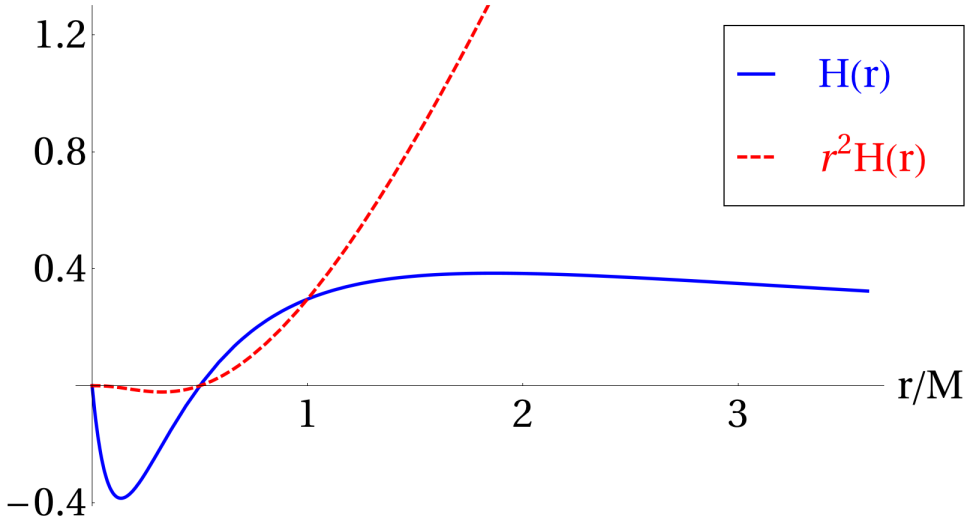

the eigenvalue of the iteration matrix that is related to this equation system has a solution if the absolute eigenvalues are below one (see page 74 for details).

Putting things together the new idea is to analyze the eigenvalues of the iteration matrix at the beginning of a Newton step. If the maximal eigenvalue is smaller than one the linear problem will have a solution and in particular it will not diverge. From the Newton path it follows that it will reach either a solution, a critical point with singular Jacobian or the boundary. In addition the goal function might be chosen such that the outer boundary will not be reached. Assuming that the apparent horizon is somewhat away from any black hole also critical points seem unlikely to occur. Starting with a surface that is larger than the expected apparent horizon makes this solution the nearest. Thus a damped Newton iteration will have good chances in finding the right solution when the specified eigenvalue is smaller than one.

There is one major drawback in these theoretical discussions. Newton methods are favored for their quadratic convergence near to a solution. But the Newton

path can exhibit very small steps that nearly stall the advancement. Thus the speed of these solvers might not be superior to fast flow methods that were described in the introduction 1.4. The usability of Newton methods has to be tested experimentally, compare also Thornburg's observations in [70].

4.2 Linearization and Eigenvalues

The next lines will introduce basic notations that are used in this chapter. We start with the formulation of the Jacobian

$$H(h_0 + h_1) \approx H(h_0) + \frac{\mathrm{d}H}{\mathrm{d}h} h_1 \tag{4.8}$$

where h_1 plays the role of a small perturbation $\mathrm{d}h$ of the surface h_0. h shall be discretized by N_{tot} points labeled by I and J. Within this setup at each iteration step the matrix equation can be written as

$$\sum_J \left.\frac{\mathrm{d}H}{\mathrm{d}h}\right|_{IJ} \mathrm{d}h_J = -H(h^0)_I. \tag{4.9}$$

Wherein $\left.\frac{\mathrm{d}H}{\mathrm{d}h}\right|_{IJ}$ is the proportional (linear) change of H at position I when the surface at position J is changed by an infinitesimal amount. Alternatively it is also possible to think of label J as generalized index of coefficients of the expansion in spherical harmonics. The term $\left.\frac{\mathrm{d}H}{\mathrm{d}h}\right|_{IJ}$ then expresses the proportional change of H at position I when the coefficient J is changed by an infinitesimal amount.

The following sections will describe the setup of the experiments with the eigenvalue method in a greater depth. In section 4.2.1 the expansion H will be written as function of the height h alone. Therein the expansion and all metric functions are assumed to be in Cartesian coordinates, the necessary transformation is taken into account. The subsequent section 4.2.2 shows the linearization and generation of the Jacobian from the functional $H(h)$. Finally in 4.2.3 the iteration matrix for the Newton method is given as a function of the surface. Certain steps were coded symbolically in Mathematica as verification. Later on the program will compute all terms numerically when both the metric and the surface are given.

4.2.1 The Expansion as Functional of the Height

The following analysis is based on the assumption that the surface is represented by the height function $h(\theta, \phi)$. Most modern apparent horizon finders use this ansatz, often combined with the expansion into spherical harmonics. Furthermore this height function shall be given by a finite set of numbers – either the coefficients of the spherical harmonics or the actual coordinates of points on the surface. The indices u, v, w, s, t stand for the spherical coordinates r, θ and ϕ whereas $i, j, k, \ldots$ represent the Cartesian coordinates x, y, z.

Given the height $h(\theta, \phi)$ then the outward normal s^i can be computed with the help of the 3-dimensional scalar function $F(r, \theta, \phi) = r - h(\theta, \phi)$. The surface is the level set $F\big(\, h(\theta, \phi)\,, \theta, \phi\big) = 0$ of this scalar field, and the unit normal can be written as

$$s^i = \frac{g^{ij}\nabla_j F}{\sqrt{g^{kl}\nabla_k F \nabla_l F}}. \tag{4.10}$$

The covariant derivative ∇ is compatible with the three-dimensional metric of the spatial hypersurface. Inserting s^i into equation (4.1) the expansion

$$\begin{aligned} H = \; & |\nabla F|^{-3}\, g^{ij} g^{kl} \Big(\nabla_k F \nabla_l F \nabla_i \nabla_j F - \nabla_j F \nabla_l F \nabla_i \nabla_k F \Big) \\ & + \; |\nabla F|^{-2}\, g^{ik} g^{jl} K_{ij} \nabla_k F \nabla_l F \; - \; g^{ij} K_{ij} \end{aligned} \tag{4.11}$$

is a function of $\nabla_i F$ where the abbreviation

$$|\nabla F| \; = \; \sqrt{g^{kl}\nabla_k F \nabla_l F} \tag{4.12}$$

is used. Derivatives of $F(h)$ should conveniently appear in spherical coordinates

$$\partial_r F = 1, \quad \partial_\theta F = -h_{,\theta} \quad \text{and} \quad \partial_\phi F = -h_{,\phi}. \tag{4.13}$$

On the other hand in most numerical codes the fields g_{ij} and K_{ij} and their derivatives are given on a Cartesian grid. Introduce the transformation from Cartesian to spherical coordinates

$$T^u_i = \frac{\partial x^u}{\partial x^i}. \tag{4.14}$$

With those the first and second derivatives of F as function of h alone become

$$\nabla_i F = T_i^u \partial_u F = T_i^r - T_i^\theta h_{,\theta} - T_i^\phi h_{,\phi} \qquad \text{and} \tag{4.15}$$

$$\begin{aligned}\nabla_i \nabla_j F &= \partial_i \nabla_j F - \Gamma_{ij}^k \nabla_k F \\ &= \nabla_i T_j^r - \nabla_i T_j^\theta h_{,\theta} - \nabla_i T_j^\phi h_{,\phi} - T_j^\theta T_i^\theta h_{,\theta\theta} - T_j^\phi T_i^\phi h_{,\phi\phi} - (T_i^\theta T_j^\phi + T_i^\phi T_j^\theta) h_{,\theta\phi}\end{aligned} \tag{4.16}$$

where the obvious abbreviation $\nabla_i T_j^u = \partial_i T_j^u - \Gamma_{ij}^k T_k^u$ is used. The following four variables help to further shorten the notation. Parentheses around indices mean the sum over the specific combinations of those indices given below:

$$\begin{aligned} G^{uv} &\coloneqq g^{ij} T_i^u T_j^v, \\ F^{uv} &\coloneqq K_{ij} g^{ik} g^{jl} T_k^u T_l^v, \\ M^{uvw} &\coloneqq g^{kl} g^{ij} (T_k^u T_l^v \nabla_i T_j^w - T_j^u T_l^v \nabla_i T_k^w), \\ N^{uvst} &\coloneqq g^{kl} g^{ij} (T_i^u T_j^v T_k^s T_l^t - T_j^u T_l^v T_i^s T_k^t), \end{aligned} \tag{4.17}$$

$$\begin{aligned} M^{u(vw)} &= M^{uvw} + M^{uwv}, \\ M^{(uvv)} &= M^{uvv} + M^{vuv} + M^{vvu}, \\ N^{(uv)(st)} &= N^{uvst} + N^{vust} + N^{uvts} + N^{vuts}. \end{aligned} \tag{4.18}$$

By plugging $\nabla_i F$ and $\nabla_i \nabla_j F$ into equation (4.11) the expansion is

$$\begin{aligned} H(h) = &\left(G^{rr} - 2G^{r\theta} h_{,\theta} - 2G^{r\phi} h_{,\phi} + G^{\theta\theta} h_{,\theta}^2 + G^{\phi\phi} h_{,\phi}^2 + 2G^{\theta\phi} h_{,\theta} h_{,\phi}\right)^{-3/2} \\ &\Big(M^{rrr} - h_{,\theta} M^{(rr\theta)} - h_{,\phi} M^{(rr\phi)} + h_{,\theta}^2 M^{(r\theta\theta)} + h_{,\phi}^2 M^{(r\phi\phi)} + h_{,\theta} h_{,\phi} M^{(r\theta\phi)} \\ &- h_{,\theta}^3 M^{\theta\theta\theta} - h_{,\theta}^2 h_{,\phi} M^{(\theta\theta\phi)} - h_{,\theta} h_{,\phi}^2 M^{(\theta\phi\phi)} - h_{,\phi}^3 M^{\phi\phi\phi} \\ &- h_{,\theta\theta} N^{\theta\theta rr} + h_{,\theta\theta} h_{,\phi} N^{\theta\theta(r\phi)} - h_{,\theta\theta} h_{,\phi}^2 N^{\theta\theta\phi\phi} \\ &- h_{,\phi\phi} N^{\phi\phi rr} + h_{,\phi\phi} h_{,\theta} N^{\phi\phi(r\theta)} - h_{,\phi\phi} h_{,\theta}^2 N^{\phi\phi\theta\theta} \\ &- h_{,\theta\phi} N^{(\theta\phi)rr} + h_{,\theta\phi} h_{,\theta} N^{(\theta\phi)(r\theta)} + h_{,\theta\phi} h_{,\phi} N^{(\theta\phi)(r\phi)} - h_{,\theta\phi} h_{,\theta} h_{,\phi} N^{(\theta\phi)(\theta\phi)}\Big) \\ &+ \left(G^{rr} - 2G^{r\theta} h_{,\theta} - 2G^{r\phi} h_{,\phi} + G^{\theta\theta} h_{,\theta}^2 + G^{\phi\phi} h_{,\phi}^2 + 2G^{\theta\phi} h_{,\theta} h_{,\phi}\right)^{-1} \\ &\cdot \left(F^{rr} - 2F^{r\theta} h_{,\theta} - 2F^{r\phi} h_{,\phi} + F^{\theta\theta} h_{,\theta}^2 + F^{\phi\phi} h_{,\phi}^2 + 2F^{\theta\phi} h_{,\theta} h_{,\phi}\right) \\ &- K\,. \end{aligned} \tag{4.19}$$

Note that some combinations like $h_{,\theta\theta}h_{,\theta}$ do not appear because the corresponding prefactors $N^{\theta\theta(r\theta)}$ are zero. Equation (4.19) shows the expansion as a nonlinear function of the height function $h(\theta, \phi)$ and its first and second derivatives. The use of spherical derivatives with Cartesian coordinate components of the metric is incorporated in the variables G^{uv}, F^{uv}, M^{uvw} and N^{uvst}.

4.2.2 The Linear Perturbation of the Expansion

The next section will compute the linearized perturbation of the expansion as an intermediate step to gain the Jacobian. For that the height $h(\theta, \phi)$ is rewritten as a perturbation around a given surface:

$$h = h_0 + h_1 = h_0 + \mathrm{d}h \ . \tag{4.20}$$

For small perturbations the expansion can be calculated as an unperturbed part plus a product of the Jacobian and $\mathrm{d}h$

$$H(h) \approx H(h_0) + \left.\frac{\mathrm{d}H}{\mathrm{d}h}\right|_{h=h_0} \mathrm{d}h. \tag{4.21}$$

Note that in equation (4.19) the functional H is only written with derivatives of h. The dependence on h is only indirectly as all values are evaluated at positions $r = h$. In principle all the perturbations of the derivatives of the height function will directly follow from the perturbation h_1 itself. But in the following calculations the layout will be broadened to allow a dependence not only on the height function but also on its angular derivatives $h_{,\theta}$, $h_{,\phi}$, $h_{,\theta\theta}$, $h_{,\phi\phi}$ and $h_{,\theta\phi}$ as additional variables. By doing so, the analysis can be held general. Only finally one differencing scheme has to be chosen either finite differences or differentiation of the basis functions of the spherical harmonics. Then the perturbation will solely depend on h. Similar to (4.20) the perturbations of the derivatives are written as

$$h_{,\theta} = h_{0,\theta} + h_{1,\theta}, \qquad h_{,\phi} = h_{0,\phi} + h_{1,\phi}, \tag{4.22}$$

$$h_{,\theta\theta} = h_{0,\theta\theta} + h_{1,\theta\theta}, \quad h_{,\phi\phi} = h_{0,\phi\phi} + h_{1,\phi\phi} \quad \text{and} \quad h_{,\theta\phi} = h_{0,\theta\phi} + h_{1,\theta\phi}. \tag{4.23}$$

There is one key ingredient that is not entirely established. For a perturbation one should assume h_1 to be small, but there is no a priori possibility to control the relative size of e.g. $h_{0,\theta}$ and $h_{1,\theta}$. Nevertheless we will assume $h_{0,\theta}$ to be much larger than $h_{1,\theta}$ and similar for the other derivatives, which is justified by the assumption that the surface has to be smooth and that high frequency perturbations are suppressed. Both can be controlled by either the number of points in the grid or the highest mode of an expansion in spherical harmonics.

Although no term inside $H(h)$ is proportional to r, the linearized expression has one. It includes the dependence of the metric and the extrinsic curvature on the radial position. In this sense the linearized perturbation will be written as

$$H(h) \approx H(h_0) + h_{1,r}C_{1,r} + h_{1,\theta}C_{1,\theta} + h_{1,\phi}C_{1,\phi} + h_{1,\theta\theta}C_{1,\theta\theta} + h_{1,\phi\phi}C_{1,\phi\phi} + h_{1,\theta\phi}C_{1,\theta\phi}, \tag{4.24}$$

where the indices *zero* and *one* indicate unperturbed and perturbed quantities respectively. The constants C_i will be determined within the next paragraphs.

The main task comes down to writing equation (4.19) with the linearizations (4.20), (4.22) and (4.23). Then all terms are neglected that are quadratic or of higher order in any perturbation term, these terms include for example h_1^2 but also $h_{1,\theta}^2$ and $h_{1,\phi}h_{1,\theta}$. As a preparation the different combinations of $h_{,\theta}$, $h_{,\phi}$, $h_{,\theta\theta}$, $h_{,\phi\phi}$ and $h_{,\theta\phi}$ that arise in equation (4.19) are split into the unperturbed and the perturbed part in linear order. The general relation for arbitrary terms x and y is

$$(x+y)^n \approx x^n + nx^{n-1}y, \qquad \text{for} \quad x \gg y. \tag{4.25}$$

For the derivatives the following perturbations are used:

$$\begin{aligned} h_{,\theta} &= h_{0,\theta} + h_{1,\theta}, \\ h_{,\phi} &= h_{0,\phi} + h_{1,\phi}, \\ (h_{,a})^n &\approx (h_{0,a})^{n-1} + n(h_{0,a})^{n-1}h_{1,a} \quad \text{and} \\ (h_{,a})^2 h_{,b} &\approx (h_{0,a})^2 h_{0,b} + (h_{0,a})^2 h_{1,b} + 2h_{0,a}h_{0,b}h_{1,a}. \end{aligned} \tag{4.26}$$

All occurring combinations of the derivatives are explicitly written in appendix C.

The following abbreviations $\mathcal{G}$, $\mathcal{M}$ and $\mathcal{F}$ depending only on the unperturbed expressions h_0 shorten the subsequent equations:

$$\mathcal{G} = G^{rr} - 2G^{r\theta}h_{0,\theta} - 2G^{r\phi}h_{0,\phi} + G^{\theta\theta}h_{0,\theta}^2 + G^{\phi\phi}h_{0,\phi}^2 + 2G^{\theta\phi}h_{0,\theta}h_{0,\phi}, \tag{4.27}$$

$$\begin{aligned}\mathcal{M} = {} & M^{rrr} - h_{0,\theta}M^{(rr\theta)} - h_{0,\phi}M^{(rr\phi)} + h_{0,\theta}^2M^{(r\theta\theta)} + h_{0,\phi}^2M^{(r\phi\phi)} + h_{0,\theta}h_{0,\phi}M^{(r\theta\phi)} \\ & - h_{0,\theta}^3M^{\theta\theta\theta} - h_{0,\theta}^2h_{0,\phi}M^{(\theta\theta\phi)} - h_{0,\theta}h_{0,\phi}^2M^{(\theta\phi\phi)} - h_{0,\phi}^3M^{\phi\phi\phi} \\ & - h_{,\theta\theta}N^{\theta\theta rr} + h_{,\theta\theta}h_{0,\phi}N^{\theta\theta(r\phi)} - h_{,\theta\theta}h_{0,\phi}^2N^{\theta\theta\phi\phi} \\ & - h_{,\phi\phi}N^{\phi\phi rr} + h_{,\phi\phi}h_{0,\theta}N^{\phi\phi(r\theta)} - h_{,\phi\phi}h_{0,\theta}^2N^{\phi\phi\theta\theta} \\ & - h_{,\theta\phi}N^{(\theta\phi)rr} + h_{,\theta\phi}h_{0,\theta}N^{(\theta\phi)(r\theta)} + h_{,\theta\phi}h_{0,\phi}N^{(\theta\phi)(r\phi)} - h_{,\theta\phi}h_{0,\theta}h_{0,\phi}N^{(\theta\phi)(\theta\phi)},\end{aligned} \tag{4.28}$$

$$\mathcal{F} = F^{rr} - 2F^{r\theta}h_{0,\theta} - 2F^{r\phi}h_{0,\phi} + F^{\theta\theta}h_{0,\theta}^2 + F^{\phi\phi}h_{0,\phi}^2 + 2F^{\theta\phi}h_{0,\theta}h_{0,\phi}\ . \tag{4.29}$$

The perturbed and the linearization of the unperturbed parts of (4.19) are then

$$H(h_0 + h_1) = H(h_0) + H_1(h_0, h_1) \tag{4.30}$$

$$H(h_0) = \mathcal{G}^{-3/2} \cdot \mathcal{M} + \mathcal{G}^{-1} \cdot \mathcal{F} - K \tag{4.31}$$

$$H_1(h_0, h_1) = \tag{4.32}$$

$$\begin{aligned}& \mathcal{G}^{-3/2}\Big[\mathbf{h}_{\mathbf{1},\theta}\Big(- M^{(rr\theta)} + 2h_{0,\theta}M^{(r\theta\theta)} + h_{0,\phi}M^{(r\theta\phi)} - 3h_{0,\theta}^2M^{\theta\theta\theta} \\ & \qquad - 2h_{0,\theta}h_{0,\phi}M^{(\theta\theta\phi)} - h_{0,\phi}^2M^{(\theta\phi\phi)} \\ & \qquad + h_{0,\phi\phi}N^{\phi\phi(r\theta)} - 2h_{0,\phi\phi}h_{0,\theta}N^{\phi\phi\theta\theta} + h_{0,\theta\phi}N^{(\theta\phi)(r\theta)} - h_{0,\theta\phi}h_{0,\phi}N^{(\theta\phi)(\theta\phi)}\Big) \\ & \quad \mathbf{h}_{\mathbf{1},\phi}\Big(- M^{(rr\phi)} + 2h_{0,\phi}M^{(r\phi\phi)} + h_{0,\theta}M^{(r\theta\phi)} - h_{0,\theta}^2M^{(\theta\theta\phi)} \\ & \qquad - 2h_{0,\theta}h_{0,\phi}M^{(\theta\phi\phi)} - 3h_{0,\phi}^2M^{\phi\phi\phi} \\ & \qquad + h_{0,\theta\theta}N^{\theta\theta(r\phi)} - 2h_{0,\theta\theta}h_{0,\phi}N^{\theta\theta\phi\phi} + h_{0,\theta\phi}N^{(\theta\phi)(r\phi)} - h_{0,\theta\phi}h_{0,\theta}N^{(\theta\phi)(\theta\phi)}\Big) \\ & \quad \mathbf{h}_{\mathbf{1},\theta\theta}\Big(- N^{\theta\theta rr} + h_{0,\phi}N^{\theta\theta(r\phi)} - h_{0,\phi}^2N^{\theta\theta\phi\phi}\Big) \\ & \quad \mathbf{h}_{\mathbf{1},\phi\phi}\Big(- N^{\phi\phi rr} + h_{0,\theta}N^{\phi\phi(r\theta)} - h_{0,\theta}^2N^{\phi\phi\theta\theta}\Big) \\ & \quad \mathbf{h}_{\mathbf{1},\theta\phi}\Big(- N^{(\theta\phi)rr} + h_{0,\theta}N^{(\theta\phi)(r\theta)} + h_{0,\phi}N^{(\theta\phi)(r\phi)} - h_{0,\theta}h_{0,\phi}N^{(\theta\phi)(\theta\phi)}\Big)\Big] \\ & - 3\mathcal{G}^{-5/2}\mathcal{M}\Big(\mathbf{h}_{\mathbf{1},\theta}\Big(- G^{r\theta} + G^{\theta\theta}h_{0,\theta} + G^{\theta\phi}h_{0,\phi}\Big) + \mathbf{h}_{\mathbf{1},\phi}\Big(- G^{r\phi} + G^{\phi\phi}h_{0,\phi} + G^{\theta\phi}h_{0,\theta}\Big)\Big) \\ & + \mathcal{G}^{-1}\Big(\mathbf{h}_{\mathbf{1},\theta}(-2F^{r\theta} + 2h_{0,\theta}F^{\theta\theta} + h_{0,\phi}2F^{\theta\phi}) + \mathbf{h}_{\mathbf{1},\phi}(-2F^{r\phi} + 2h_{0,\phi}F^{\phi\phi} + h_{0,\theta}2F^{\theta\phi})\Big) \\ & - 2\mathcal{G}^{-2}\mathcal{F}\Big(\mathbf{h}_{\mathbf{1},\theta}\Big(- G^{r\theta} + G^{\theta\theta}h_{0,\theta} + G^{\theta\phi}h_{0,\phi}\Big) + \mathbf{h}_{\mathbf{1},\phi}\Big(- G^{r\phi} + G^{\phi\phi}h_{0,\phi} + G^{\theta\phi}h_{0,\theta}\Big)\Big)\ .\end{aligned} \tag{4.33}$$

By collecting all terms in front of the perturbed derivatives the linear change of H due to the perturbation is given by the following structure (recall equation (4.24))

$$H(h_0 + h_1) - H(h_0) = \tag{4.34}$$
$$h_{1,r}C_{1,r} + h_{1,\theta}C_{1,\theta} + h_{1,\phi}C_{1,\phi} + h_{1,\theta\theta}C_{1,\theta\theta} + h_{1,\phi\phi}C_{1,\phi\phi} + h_{1,\theta\phi}C_{1,\theta\phi}.$$

The constants in equation (4.34) are given by

$$C_{1,r} = -\frac{3}{2}\mathcal{G}^{-5/2}\,\mathcal{M}\,\partial_r\mathcal{G} + \mathcal{G}^{-3/2}\partial_r\mathcal{M} + \mathcal{G}^{-2}\,\mathcal{F}\,\partial_r\mathcal{G} + \mathcal{G}^{-1}\,\partial_r\mathcal{F} - \partial_r K, \tag{4.35}$$

$$\begin{aligned} C_{1,\theta} = {} & \mathcal{G}^{-3/2}\Big(- M^{(r\theta\theta)} + 2h_{0,\theta}M^{(r\theta\theta)} + h_{0,\phi}M^{(r\theta\phi)} - 3h_{0,\theta}^2M^{\theta\theta\theta} \\ & \quad - 2h_{0,\theta}h_{0,\phi}M^{(\theta\theta\phi)} - h_{0,\phi}^2M^{(\theta\phi\phi)} \\ & \quad + h_{0,\phi\phi}N^{\phi\phi(r\theta)} - 2h_{0,\phi\phi}h_{0,\theta}N^{\phi\phi\theta\theta} + h_{0,\theta\phi}N^{(\theta\phi)(r\theta)} - h_{0,\theta\phi}h_{0,\phi}N^{(\theta\phi)(\theta\phi)}\Big) \\ & - 3\mathcal{G}^{-5/2}\Big(- G^{r\theta} + G^{\theta\theta}h_{0,\theta} + G^{\theta\phi}h_{0,\phi}\Big)\cdot\mathcal{M} \\ & + \mathcal{G}^{-1}(-2F^{r\theta} + 2h_{0,\theta}F^{\theta\theta} + h_{0,\phi}2F^{\theta\phi}) \\ & - 2\mathcal{G}^{-2}\Big(- G^{r\theta} + G^{\theta\theta}h_{0,\theta} + G^{\theta\phi}h_{0,\phi}\Big)\cdot\mathcal{F}\ , \end{aligned} \tag{4.36}$$

$$\begin{aligned} C_{1,\phi} = {} & \mathcal{G}^{-3/2}\Big(- M^{(r\phi\phi)} + 2h_{0,\phi}M^{(r\phi\phi)} + h_{0,\theta}M^{(r\theta\phi)} - h_{0,\theta}^2M^{(\theta\theta\phi)} \\ & \quad - 2h_{0,\theta}h_{0,\phi}M^{(\theta\phi\phi)} - 3h_{0,\phi}^2M^{\phi\phi\phi} \\ & \quad + h_{0,\theta\theta}N^{\theta\theta(r\phi)} - 2h_{0,\theta\theta}h_{0,\phi}N^{\theta\theta\phi\phi} + h_{0,\theta\phi}N^{(\theta\phi)(r\phi)} - h_{0,\theta\phi}h_{0,\theta}N^{(\theta\phi)(\theta\phi)}\Big) \\ & - 3\mathcal{G}^{-5/2}\Big(- G^{r\phi} + G^{\phi\phi}h_{0,\phi} + G^{\theta\phi}h_{0,\theta}\Big)\cdot\mathcal{M} \\ & + \mathcal{G}^{-1}(-2F^{r\phi} + 2h_{0,\phi}F^{\phi\phi} + h_{0,\theta}2F^{\theta\phi}) \\ & - 2\mathcal{G}^{-2}\Big(- G^{r\phi} + G^{\phi\phi}h_{0,\phi} + G^{\theta\phi}h_{0,\theta}\Big)\cdot\mathcal{F}\ , \end{aligned} \tag{4.37}$$

$$C_{1,\theta\theta} = \mathcal{G}^{-3/2}\Big(- N^{\theta\theta rr} + h_{0,\phi}N^{\theta\theta(r\phi)} - h_{0,\phi}^2N^{\theta\theta\phi\phi}\Big), \tag{4.38}$$

$$C_{1,\phi\phi} = \mathcal{G}^{-3/2}\Big(- N^{\phi\phi rr} + h_{0,\theta}N^{\phi\phi(r\theta)} - h_{0,\theta}^2N^{\phi\phi\theta\theta}\Big) \quad \text{and} \tag{4.39}$$

$$C_{1,\theta\phi} = \mathcal{G}^{-3/2}\Big(- N^{(\theta\phi)rr} + h_{0,\theta}N^{(\theta\phi)(r\theta)} + h_{0,\phi}N^{(\theta\phi)(r\phi)} - h_{0,\theta}h_{0,\phi}N^{(\theta\phi)(\theta\phi)}\Big). \tag{4.40}$$

The dependence from h_1 is introduced through the changes in the metric, the extrinsic curvature and the coordinate transformations. They all see the radial change $\partial/\partial h = \partial/\partial r$ and are therefore computed as derivatives with respect to r.

Equations (4.34)-(4.40) are given to the Jacobian matrix, according to the finite difference scheme.

4.2.3 Matrix Form of Linearization

In the previous section the expansion was expressed as sum of an unperturbed plus a linear perturbed part. The perturbation was assumed to come from the derivatives of the height function h and from indirect contributions that are related to the change of the position of the surface. In this section the matrix form of the Jacobian will be introduced. For this the representation of the height function and its derivation method has to be chosen – here the height is fixed on a regular angular grid and finite differentiation is used.

In this work the surface function $h(\theta, \phi)$ will be discretized on a rectangular grid in θ- and ϕ-direction with N_θ and N_ϕ points respectively. The points are placed with equal angular distance and the angles in θ-direction are staggered to avoid problems at the poles, otherwise several points would coincide. Moreover N_θ has to be even for the application of the correct boundary conditions:

$$\theta_i = (i - 1/2)\, \pi/N_\theta\,, \qquad i = 1 \ldots N_\theta, \tag{4.41}$$

$$\phi_j = (j - 1)\, 2\pi/N_\phi\,, \qquad j = 1 \ldots N_\phi\,. \tag{4.42}$$

The spacings are given by $\Delta\theta = \pi/N_\theta$ and $\Delta\phi = 2\pi/N_\phi$.[1] For values beyond the boundaries in θ-direction the code reaches across the poles (see [60]), that evaluates to a change of $N_\theta/2$ in the index of ϕ. In ϕ-direction periodic boundary conditions are used.

Overall centered finite difference stencils of second order are used, limitations in memory prevented from going to higher orders. The indices i and j of one point are related via

$$K = iN_\theta + j \tag{4.43}$$

to one general index, called with capital letter K for example. For the next lines the abbreviation $[i, j]$ is used to indicate that i and j form one index using the

[1] The notation is adapted to have indices starting at *one* because the computer algebra system MATHEMATICA organizes matrices that way.

scheme above. With the notation $h_{[i,j]}$ for the height in direction $\theta = \theta_i$ and $\phi = \phi_j$, $i = 1 \ldots N_\theta$, and $j = 1 \ldots N_\phi$, the finite differences are

$$\begin{aligned}
h_{,\theta[i,j]} &= \left(h_{[i+1,j]} - h_{[i-1,j]}\right)/(2\Delta\theta), \\
h_{,\phi[i,j]} &= \left(h_{[i,j+1]} - h_{[i,j-1]}\right)/(2\Delta\phi), \\
h_{,\theta\theta[i,j]} &= \left(h_{[i+1,j]} - 2h_{[i,j]} + h_{[i-1,j]}\right)/(\Delta\theta)^2, \\
h_{,\phi\phi[i,j]} &= \left(h_{[i,j+1]} - 2h_{[i,j]} + h_{[i,j-1]}\right)/(\Delta\phi)^2 \qquad \text{and} \\
h_{,\theta\phi[i,j]} &= \left(h_{[i+1,j+1]} - h_{[i-1,j+1]} - h_{[i+1,j-1]} + h_{[i-1,j-1]}\right)/(4\Delta\theta\Delta\phi)\ ,
\end{aligned} \tag{4.44}$$

modulo the boundary conditions.

The linear change of H at position K as in equation (4.34) is written as

$$\mathrm{d}H_K = H_K(h_0 + h_1) - H_K(h_0) \approx \sum_L J_{KL}\ \mathrm{d}h_L \tag{4.45}$$

where the indices K and L label one of the $N = N_\theta \times N_\phi$ points on the grid. The discrete Jacobian is a matrix whose entries J_{KL} give the linear change of H at position K when the height of position L is changed by a small amount. Rewriting the left hand side of equation (4.45) via (4.34) and (4.44) gives

$$\begin{aligned}
\mathrm{d}H_K &= H_K(h_{[i,j]} + h_{[i,j]}) - H_K(h_{[i,j]}) \\
&= \quad C_{1,r}h_{1[i,j]} \\
&\quad + C_{1,\theta}(h_{1[i+1,j]} + h_{1[i-1,j]})/(2\Delta\theta) \\
&\quad + C_{1,\phi}(h_{1[i,j+1]} + h_{1[i,j-1]})/(2\Delta\phi) \\
&\quad + C_{1,\theta\theta}(h_{1[i+1,j]} - 2h_{1[i,j]} + h_{1[i-1,j]})/(\Delta\theta)^2 \\
&\quad + C_{1,\phi\phi}(h_{1[i,j+1]} - 2h_{1[i,j]} + h_{1[i,j-1]})/(\Delta\phi)^2 \\
&\quad + C_{1,\theta\phi}(h_{1[i+1,j+1]} - h_{1[i-1,j+1]} - h_{1[i+1,j-1]} + h_{1[i-1,j-1]})/(\Delta\theta\Delta\phi) \\
&= a_{K[i,j]}h_{1[i,j]} + a_{K[i+1,j]}h_{1[i+1,j]} + a_{K[i,j+1]}h_{1[i,j+1]} + a_{K[i-1,j]}h_{1[i-1,j]} \\
&\quad + a_{K[i,j-1]}h_{1[i,j-1]} + a_{K[i+1,j+1]}h_{1[i+1,j+1]} + a_{K[i+1,j-1]}h_{1[i+1,j-1]} \\
&\quad + a_{K[i-1,j+1]}h_{1[i-1,j+1]} + a_{K[i-1,j-1]}h_{1[i-1,j-1]} \\
&= \sum_L a_{KL}h_{1L}\ .
\end{aligned} \tag{4.46}$$

All constants $C_{1,a}$ and $C_{1,aa}$ have the index $K \hat{=} [i, j]$ but it is suppressed for the ease of reading. This results in a definition for the Jacobian J_{KL} on the right, that is needed in equation (4.9). By comparison of coefficients the values a_{KL} (that are defined for every index K) are exactly the matrix entries of the Jacobian J_{KL}. The perturbation h_{1L} plays the role of the small change $\mathrm{d}h_L$.

4.2.4 The Eigenvalues of the Iteration Matrix

At each step of the Newton method the matrix equation (4.9) has to be solved. For the forthcoming derivation this equation is written as

$$\sum_L J_{KL}\ \mathrm{d}h_L = -H_K. \tag{4.47}$$

This system of equations has to be solved for the unknown change $\mathrm{d}h_L$ of the surface at position L. Through finite differencing the matrix will be sparse – the expansion at one point will be effected only from neighbouring places in the grid.

In the last sections the solution of the expansion equation $H = 0$ was reformulated to become a linearized problem with a matrix equation that has to be solved at each iteration step. The subsequent derivation is better studied in the usual terms of linear algebra therefore the equation will be written as

$$\mathbf{A}\ \mathrm{d}\mathbf{h} = -\mathbf{r} \tag{4.48}$$

with an $N \times N$ matrix $\mathbf{A}$, solution vector $\mathrm{d}\mathbf{h}$ and the residuals vector $\mathbf{r}$ of length N where $N = N_\theta \times N_\phi$ is the total number of points of the surface grid. The notation is introduced by Schwarz [39].

The computations that were explained in the last sections were implemented in the MATHEMATICA computer algebra system that allowed the management of the increasingly large terms. Originally it was planned to have an analytic statement about the eigenvalues for a given analytic metric. However the naive algebraic substitutions gave rise to high memory consumption. A medium size grid in spherical symmetry with $N_\theta = N_\phi = 16$ and non-spherical metrics with an even smaller number of points exhausted the four gigabyte of RAM on the desktop computer.

Therefore the program was reformulated to calculate pure numerical values for the matrix from explicitly given surfaces and metrics.

A linear system of equations can be solved by iterative algorithms. Successive steps define a linear mapping with the solution vector $\mathrm{d}\mathbf{h}^*$ as fixed point. For a compact notation the matrix $\mathbf{A}$ is split into matrices with the diagonal elements $\mathbf{D}$, the elements of the negative lower $\mathbf{L}$ and the negative upper half $\mathbf{U}$ respectively:

$$\mathbf{A} \coloneqq \mathbf{D} - \mathbf{L} - \mathbf{U}. \tag{4.49}$$

Then the iteration matrix for a simple Jacobi-elimination system is

$$\mathbf{T_J} \coloneqq \mathbf{D}^{-1}(\mathbf{L} + \mathbf{U}), \tag{4.50}$$

$$\mathbf{c_J} = -\mathbf{D}^{-1}\mathbf{b} \qquad \text{and} \tag{4.51}$$

$$\mathbf{x}^{(k+1)} = \mathbf{T_J}\mathbf{x}^k + \mathbf{c_J}. \tag{4.52}$$

Choosing other elimination procedures alters the iteration matrix. E. g. the iteration matrix for successive over-relaxation can be written as

$$\mathbf{T}_{SOR}(\omega) \coloneqq (\mathbf{D} - \omega\mathbf{L})^{-1}\left((1-\omega)\mathbf{D} + \omega\mathbf{U}\right), \tag{4.53}$$

$$\mathbf{c}_{SOR}(\omega) \coloneqq -\omega(\mathbf{D} - \omega\mathbf{L})^{-1}\mathbf{b} \tag{4.54}$$

with the relaxation factor $0 < \omega < 2$.

Regardless of these details the following important theorem in [39] is given:[2]

Theorem 4.2.1. *'The fixed point iteration* $\mathbf{x}^{(k+1)} = \mathbf{T}\mathbf{x}^{(k)} + \mathbf{c}$, $(k = 0, 1, 2, \dots)$ *that is completely consistent with the equation system* $\mathbf{A}\,\mathbf{x} + \mathbf{b} = 0$ *does produce a series that converges towards the solution* $\mathbf{x}^*$ *for every starting vector* $\mathbf{x}^{(0)}$ *if and only if the maximal absolute eigenvalue of* $\mathbf{T}$ *is less than one'.*

Here being 'completely consistent' means that each solution of the equation system $\mathbf{A}\,\mathbf{x} + \mathbf{b}$ is also a solution to the fixed point equation $\mathbf{x} = \mathbf{T}\mathbf{x} + \mathbf{c}$ and vice versa. Both $\mathbf{T}_J$ and $\mathbf{T}_{SOR}$ are completely consistent to equation (4.48) as needed in the theorem. The matrix that is used in the subsequent analysis is $\mathbf{T}_J$. Because of

[2] translated and rephrased from 'Satz 11.6'

the complexity of the matrix entries they could not be treated analytically. They have to be tested for a representative variety of metrics and surfaces. The next section will cover a spherical symmetric geometry that represents one black hole.

The logic behind the use of the eigenvalue information is as follows. The maximal absolute eigenvalue will already tell at the beginning of the inner iteration whether it will converge. But on the other hand at the first step of the outer Newton iteration, it will tell the condition of a Newton path. If the iteration diverges then it is unlikely that we have the 'good' case (i) of page 62. Probably it will turn towards one of the cases (ii) or (iii) that are critical points or the boundary, respectively.

4.3 Eigenvalue Experiments

After the introduction of the iteration matrix within a Newton solver in the previous section it will now be shown how its eigenvalues will reflect the region of convergence of the underlying problem. The setup is the spherically symmetric Schwarzschild metric in isotropic coordinates that is analytically given by the Brill-Lindquist initial data. Without further change of the geometry the problem of the vanishing outgoing expansion is reformulated in various ways. This leads to the so-called goal functions that have the same solution as the original problem but their iteration matrix has different eigenvalues.

First the basic result is recovered that between the minimum and the maximum of the expansion the Newton type method does indeed show possible convergence, i.e. the absolute size of the largest eigenvalue is smaller than one. The analytic expression for the expansion is given by

$$H(r) = \frac{8r(2r-m)}{(2r+m)^3} \tag{4.55}$$

For these runs the mass parameter was set to $m = 1$.

In the next sections it is assumed that *the maximal of the absolute eigenvalues belonging to the iteration matrix coming from a certain goal function G is computed for a surface that is described by parameters S*. As a short notation a

capital lambda with upper and lower indices Λ_S^G is used to express this meaning. For example the maximal absolute eigenvalue for the plain equation $H(h) = 0$ on a sphere with radius r could be written as Λ_r^H. For the sake of brevity the phrase is often reduced to state the main point as in *the eigenvalue for radius r* or *the eigenvalues for H*. The background idea of the underlying iteration matrix is always implied.

4.3.1 The Eigenvalues of the Plain Expansion

The eigenvalues coming from the solution of $H(h) = 0$ in spherical symmetry yield the expected intuitive answer about the convergence of the Newtonian approach. It was already shown in figure 4.1 that the expected region of convergence for a damped Newton iteration is within the extrema of the curve that are at $r_{min} = 1 - \sqrt{3}/2$ and $r_{max} = 1 + \sqrt{3}/2$. This estimation is strengthened by the plot of the maximal absolute eigenvalue as can be seen in figure 4.3, in that region the eigenvalues are below one.

The diagram shows both the analytical curve of the expansion $H(r)$ for a sphere with radius r and the respective maximal eigenvalue of the iteration matrix. At the extrema the former has a vanishing Jacobian, i.e. the derivatives with respect to r are zero, they mark the end points of the region of convergence, below r_{min} the damped Newton steps converges to $r = 0$ whereas initial guesses larger than r_{max} will lead to a divergence in r towards infinity.

One obvious drawback is the small number of points that are used to define the surface: only four in each direction. Since all the angular derivatives should be zero this might not play a role, but a quick check with more points reveals the following pattern, see figure 4.4: The locations where the curve of the maximal absolute eigenvalue Λ_r^H crosses 1 are not altered. Using more points let Λ_r^H move closer to 1 independent of the radius. For eigenvalues below one there is an explanation why they should increase. Because of the finite difference scheme and the regular angular grid, points are more dense towards the poles, although staggered there. Thus the system is more sensitive to small changes of the height function between points. Numerically an increase of the high frequency noise is

Figure 4.3: The maximal eigenvalues for the expansion of a sphere of given radius around a Brill-Lindquist black hole. The size of the surface was $N_\theta = N_\phi = 4$. *Top red points*: the eigenvalues, *bottom blue*: the expansion $H(r)$. The extrema of $H(r)$ corresponds to locations where the maximal eigenvalue is one.

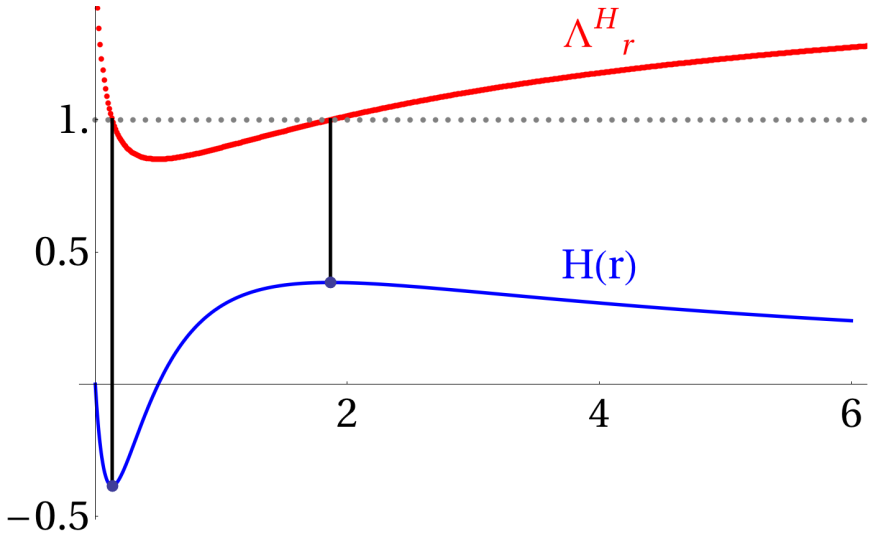

expected. This should be seen by the change of the eigenvalues of high frequency eigenmodes. But it does not explain why eigenvalues above one should decrease.

One more question comes from the behaviour for small r. If the solution $r = 0$ is a regular point the method should converge with eigenvalues below one. That is not the case though. The behaviour can be attributed to the fact that $r = 0$ is another spatial infinity in the wormhole picture. Thus it is in fact a boundary and not a real point.

All these results are of no importance unless indeed a Newton scheme does or does not converge depending on these eigenvalues. This was tested based on a damped Newton method that started on the same initial data. For that a standard Newton scheme was implemented in MATHEMATICA. It repeatedly calculates the change $\mathrm{d}h$ of the surface by solving the linear equation

$$J_{KL}\ \mathrm{d}h_L = -G_K \tag{4.56}$$

Figure 4.4: The maximal eigenvalues for spherical symmetry and H(h)=0. The grid size of the surface is varied as $N_\theta = N_\phi = 4, 8, 12, 16, 20$.

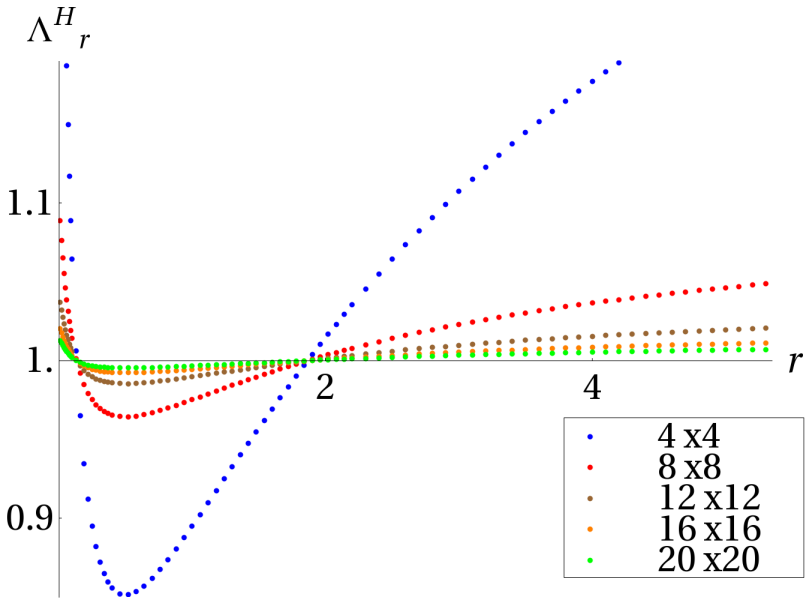

and then making a damped step in this 'direction':

$$h_K = h_K + \lambda \, \mathrm{d}h_K, \tag{4.57}$$

where $0 < \lambda \leq 1$ is the damping factor and G stands for one of the goal functions, originally it is $G = H(h)$. These tests support the ideas of using eigenvalues to find the region of convergence and to use goal functions instead of the plain expansion. Specific results are shown in section 4.3.3.

4.3.2 Goal Functions

For the case of spherical symmetry the solution of the expansion equation is reduced to root finding. Moreover the solution can be easily visualized, it is therefore used as a 'playground' for the goal functions G. The ideas and restrictions for changing the expansion equation are the following.

1. Solutions of $G = 0$ are also solutions of $H = 0$.

2. The region of convergence for Newton's method with G is enlarged.

3. No solution at spatial infinity for G.

4. G shall not depend on coordinates rather on geometric properties.

Each one of these four points will be discussed in the following lines.

The first one seems to be a natural thing to claim. But it is not clear what happens when additional solutions appear outside our region of interest. For example additional solutions corresponding to small radii may not cause a problem. Usually the initial surface is outside of the expected final location, mainly because the *outermost* trapped surface is searched. Also for simulations that use excision the interior might not even exist.

The next claim about the increase of the region of convergence is of course the main goal. In this thesis the maximal absolute eigenvalue is used as an indication of whether the region of convergence is reached or not. But it must be remembered from the previous sections that this convergence is actually only valid for one Newton step. Only when a Newton path is followed also the convergence for the non-linear equation is certain.

Removing the solution at infinity is not crucial but it is an effective way to allow surfaces that have large radius as initial guess. For systems of two black holes it is unclear whether there exists a common horizon or not. Depending on the distance between the two black holes the eigenvalues may predict different outcomes. Under these circumstances reducing the number of options by excluding the spatial infinity solution is advisable. The following lines give an idea of how to exclude infinity.

Current numerical simulations often rely on asymptotic flatness. For large distances the near field structure is of no importance the remaining contribution comes from the monopole term that is the total mass M. Then at large distances spheres of constant expansion can be found and the expected radial behaviour of the expansion is the same as in the Schwarzschild case. For isotropic coordinates the expansion will fall off with $2/r$ towards zero. Having H multiplied by r will

at least lift the end result to a constant but it turns out that the first derivative is zero so the Newton method will be ill defined. It is expected to need at least linear corrections in r to exclude infinity from the solution space.

The last of the four considerations about goal functions is subtle. Two considerations are explained but no clear answer was found. Although all the calculations are carried out with certain coordinates the choice of a good goal function will depend on the overall geometry. Even more than that it might even solely depend on the geometry since the marginally trapped surfaces are also coordinate independent. On the other hand the whole Newton method can be seen as an independent problem without knowing anything about the geometric background. Seen from this side getting insight might not be restricted to geometric properties.

Two ingredients for goal functions will be examined, one is the multiplication by the radial distance r. This will mainly effect the long range behaviour of the expansion. Another factor is $|\nabla F|^{-1} = (g^{kl}\nabla_k F \nabla_l F)^{-1/2}$ (see page 65) that has the feature of locating a puncture in the sense that it has a pole $|\nabla F|^{-1} \sim \psi^2 \sim r_{BH}^{-2}$ or equivalently its inverse is zero at a puncture. It also has the above-mentioned notion of a geometry independent quantity. In [35] Gundlach describes the mean curvature flow and states that any flow of the surface proportional to $|\nabla F| \times X$ is geometric in nature, where X is any scalar depending only on the metric, the extrinsic curvature or the outward unit normal on the surface.

4.3.3 Goal Functions, Eigenvalues and Convergence

Two kinds of adapted functions were considered in the literature, Schnetter [60] used prefactors based on r for horizon pretracking. Gundlach [35] mentions $|\nabla F|$ for his flow algorithm. In the next section several goal function are created with the foregoing ideas in mind. Then they are analyzed by the eigenvalue method. The conclusion of the behaviour leads to the following pointed *Eigenvalue Hypothesis*:

> Every damped outer iteration of a Newton method that starts with a maximal absolute eigenvalue of its inner iteration matrix below one ($\Lambda_S^G < 1$) does converge to the solution.

Table 4.1: Comparison of different goal functions with respect to the location of their extremal values and the location where the eigenvalues are 1. The test would fail if a surface with eigenvalues smaller than one did not converge to the solution.

goal function	short tag	$\partial_r G = 0$	$\Lambda_r^G = 1$	test passed
H	H	0.134, 1.87	0.134, 1.87	✓
Hr	Hr	0.25	0.25	✓
Hr^2	Hr2	0.323	0.33	✓
$H\,\lvert\nabla F\rvert^{-1}$	HinvDF	1.21	1.2	✓
$H\,\lvert\nabla F\rvert^{-1}\,r$	HinvDFr	–	–	✓
$H\,\lvert\nabla F\rvert^{-1}\,r^2$	HinvDFr2	0.207	0.21	✓

It will be a short tag for that behaviour and will also serve as a guideline. The main problem appears when $\Lambda_S^G < 1$ but the iteration does not converge (error of first kind). A series that converges although it started with $\Lambda_S^G > 1$ (error of second kind) need not be a disadvantage to the algorithm, unless based on the eigenvalue another more expensive solution method is pursued.

The following examinations must try to single out cases where despite having eigenvalue smaller than one the iteration does not converge, such cases limit the use of this method. For several surfaces both the eigenvalue is calculated and a Newton iteration is done (more details later on), that shows whether the initial surface converges or not. For high enough damping no exception was found for spherical symmetry as explained below. The results are shown in table 4.1. The short notation G^{HabsDF} is introduced to refer to one specific goal function, here the fourth of the table. The column $\partial_r G = 0$ shows the location of extrema at positive values of r. In column $\Lambda_r^G = 1$ the approximate locations are given at which the curve of eigenvalues crosses 1. The goal functions G^{Hr2}, $G^{HinvDFr}$ and $G^{HinvDFr2}$ are new in this thesis. Beside $G = Hr$ Schnetter [60] even tested $G = \bar{h}$, that is the average of h over the surface. Gundlach [35] considered $G = 2r^2\,|\nabla F|$ (also without H) as the right hand side of the flow method.

The behaviour of the eigenvalues when changing the resolution is also exhibited for the new goal functions: the places where the curve crosses 1 are not changed and the maximal eigenvalues are moved towards 1 when increasing the number of points of the surface. But there are a few exceptions, G^{Hr2} has crossing

points between 0.32 and 0.35 this is recovered for $N = 4 \times 4$ but the higher resolutions have the 1-crossing between 0.35 and 0.38. And the curves for G^{HinvDF} do not follow the usual pattern since the eigenvalues for 8×8 for large spheres are smaller (nearer to one) than the ones for 12×12. But since the main line of reasoning is not altered mainly the values that are computed for $N = N_\theta \times N_\phi = 4 \times 4$ will be used in the subsequent discussion.

First the analytic multiplications of H with r and $|\nabla F|^{-1}$ are shown in figure 4.5. The goal functions that have one factor of $|\nabla F|^{-1}$ are dashed. In the diagrams can be seen that the additional factors of r indeed change the limiting behaviours: where G^H tends towards zero, G^{rH} has the limiting constant 2 and G^{r2H} is linearly rising. One factor of $|\nabla F|^{-1}$ is able to remove the additional zero at $r = 0$. Note the absence of the outer maxima for those goal functions that are multiplied by r or r^2 and the absence of the inner minima for G^{HinvDF} and $G^{HinvDFr}$. In particular there is neither extremum for the function $G^{HinvDFr}$ for any positive r.

The eigenvalues of each method are presented in the lower panel of figure 4.5. The curves generally correspond to the behaviour that one would expect from the position of extrema. As with H all of the functions have an eigenvalue equal to one close to the location of its extrema. Only G^{Hr2} and $G^{HinvDFr^2}$ have values that are a bit higher than the analytic value. And indeed the function $G^{HinvDFr}$ has only eigenvalues less than one, it is therefore a good candidate for detailed tests also for two black holes.

The connection shown above between the maximal eigenvalue of the iteration matrix and the possible use of Newton's method is not conclusive without the real implementation of a Newton solver. For one dimension the behaviour of a Newton step is 'obvious' since it is the tangent to a function of one variable. But for the higher dimensional examples it is indispensable to check the convergence of Newton's method for several representative initial surfaces.

A Newton solver was programmed as explained in equations (4.56) and (4.57). The actual solution of the linear system of equations was done by the standard MATHEMATICA solver. The step length or damping parameter λ was chosen to be between 0.05 to 0.4 together with a simple limiter to prevent large changes of the surface. In addition when the change of the height function is very small compared

Figure 4.5: The expansion (*upper panel*) and the eigenvalues (*lower panel*) for goal functions of surfaces of constant radius r that have H multiplied with various powers of r and $|\nabla F|^{-1}$. Note the varying number of extrema for the goal functions.

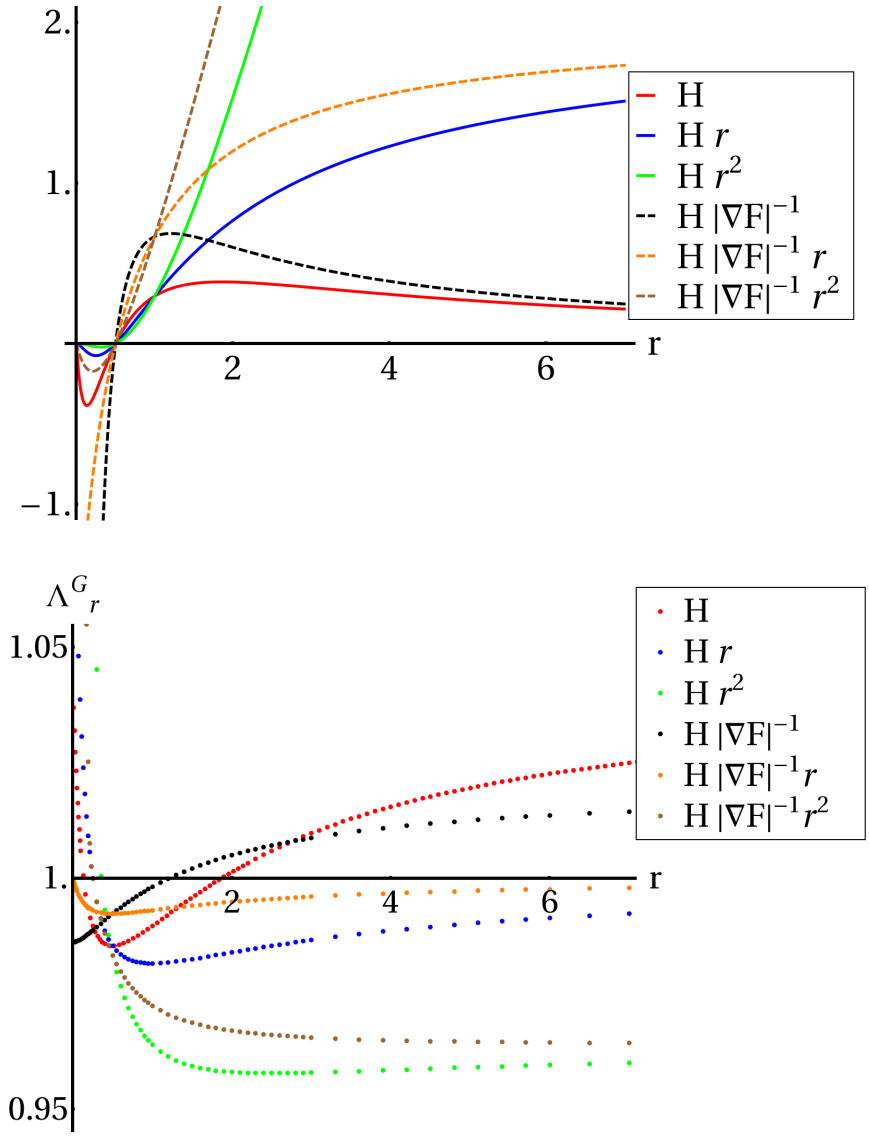

to the average height, then the full step is taken, that increases the speed once the solution is close. Also compare with theorem 3.8 and the subsequent discussion about the optimal damping strategy in [28]. These runs support the conclusion that the eigenvalues can be used as an indicator of the convergence of a damped Newton method. Initial surfaces with a corresponding largest absolute eigenvalue smaller than one converge to the solution $r = 0.5$. In figure 4.6 the mean radius of each surface is plotted over the iterations. Because the time demand is quite high only resolutions of the surface of $N = 4 \times 4$ was used. One test was done with a grid of $N = 8 \times 8$ that brought qualitatively the same results. A logarithmic plot of the data was found to be most convenient to distinguish the different regions.

For each of the goal functions mentioned above these iterations were done. All results strengthen the claim of the Eigenvalue Hypothesis. They are put together in figure 4.6. The calculated locations of the extrema of the goal functions are indicated at the left side by black dots given in table 4.1. For all the runs the region from where initial guesses converge to the solution $r = 0.5$ are well described by the location of the extrema (at the black dots). The goal function $H\ |\nabla F|^{-1}\, r$ is exceptional because every initial spherical surface will converge to the right solution. The small slope of the curves for large starting values is explained by the step size limiter that prevents the surface from making relatively big jumps. Near to the solution $r = 1/2$ the damping is switched off completely.

4.3.4 Non-Spherical Surfaces in Spherical Geometry

The previous section showed a good agreement between experiment and prediction with respect to eigenvalues and convergence. Of course this was only a first step, in this section non-spherical surfaces are considered. The problem can not be represented by a single curve in one dimension any more, no intuitive picture is possible. Two kinds of surfaces are analyzed, one with a sinusoidal modulation called S_3, the other called S_{rand} has random noise added to a sphere.

The form S_3 has a sinusoidal pattern in both θ- and ϕ-direction. The height of the surface is given by

$$h(\theta, \phi) = d + A \sin(\omega_t \theta) \sin(\omega_p \phi), \tag{4.58}$$

Figure 4.6: The mean value of h for each damped Newton iteration step for several goal functions. Depending on the initial surface these iterations converge to $r = 1/2$ or they diverge. The black dots indicate the locations of extrema, the region with eigenvalues less than one are shaded. The goal functions enlarge the region of convergence, and the convergence is indicated by the eigenvalue.

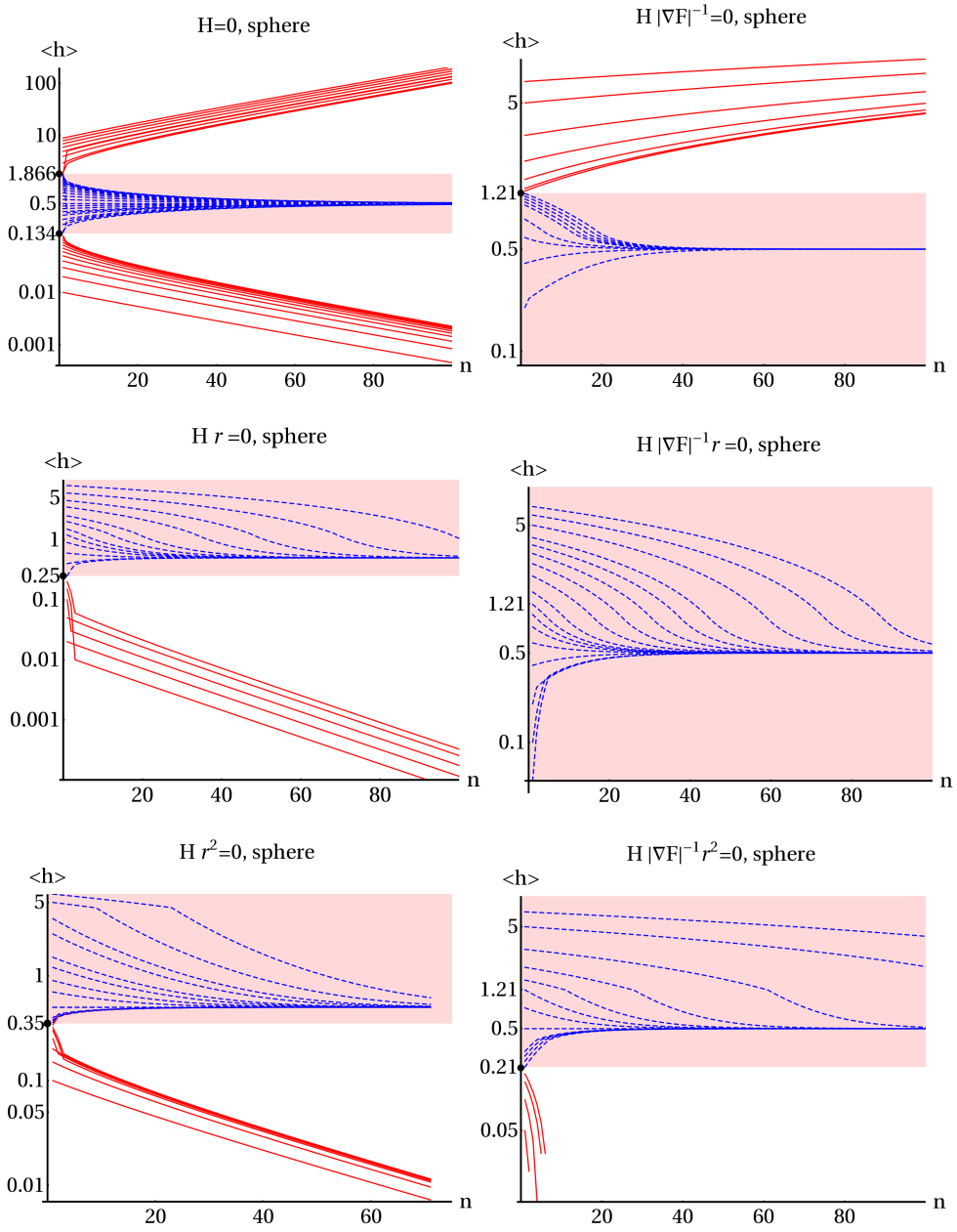

with parameters d for the mean height, the variation amplitude A, and the frequencies ω_t and ω_p. In the following tests the values are chosen as $A = d/5$, $\omega_t = 1$ and $\omega_p = 3$ such that the surface is oblate and has three hills and ditches around the equator. It needs at least twelve points in the ϕ-direction and about four in the θ-direction to form this shape at least crudely, the sizes 8×16 and 10×20 were chosen in the test runs.

The surface S_{rand} uses a random additional height around the mean radius d. The formula reads

$$h(\theta, \phi) = d + A \; random[-1, 1]. \tag{4.59}$$

The function *random* shall give uniformly distributed random numbers in the specified interval. The size of the variation was set to $A = d/10$. The grid consisted of 8×8 points. As a rough scalar characteristic of the location of the surface again its mean height is used. When the mean converges towards $r = 1/2$ then it is most likely that the surface is a sphere with radius 1/2.

Several initial surfaces are considered under iteration with the damped Newton method. Their convergence or divergence is compared against the size of the largest eigenvalue. In the upper part of figure 4.7 the mean of the height function is plotted as a function of the iteration steps. In the case of S_{rand} several of the runs converged, although they had an absolute eigenvalue larger than one. But none of the runs that did not converge had an eigenvalue of less than one. The same is true for the convergence of surfaces shaped according to S_3, they completely agree with the expectation from the Eigenvalue Hypothesis. This is partly due to the high damping values. The appendix F shows iterations where the eigenvalue approach fails for the same initial values. However, the deformation of the spheres decreases the region of convergence, surfaces with mean heights around 0.15 or 1.7 are not safely inside it, compared to the 'standard' range from 0.134 to 1.866.

Two more scenarios were considered with the goal function $G = H \; |\nabla F|^{-1} \, r$ that was promising in enlarging the region of convergence (see the lower two plot of figure 4.7). Indeed most of the surfaces of type S_{rand} and S_3 at different average heights converged. For both shapes only initial surfaces with mean height below around 0.01 did not converge – these are typically never chosen as initial data for the Newton procedure anyway. The rest of the tested surfaces had eigen-

Figure 4.7: The mean value of h for each damped Newton iteration step for the functionals $G = H$ and $G = H\ |\nabla F|^{-1}\ r$ for initial surfaces S_{rand} and S_3. The black dots indicate the locations of extrema for the spherical surface. Red lines belong to series that had an eigenvalue greater than one, blue dashed lines belong to iterations with eigenvalue smaller than one. The curves that rise from below 0.01 after around iteration 10 are not convergent, the Newton step has led them to a (partially) negative height.

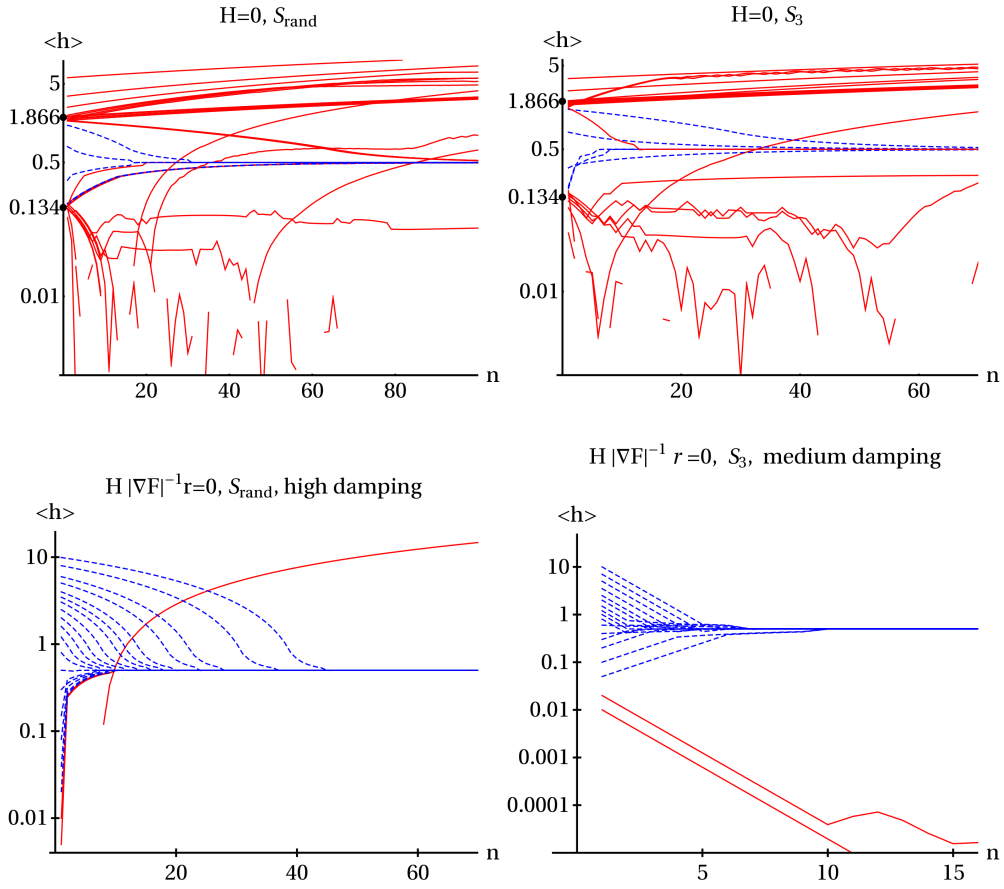

values below one and converge in compliance with the Eigenvalue Hypothesis, but again high enough damping must be applied. The goal function $G^{HinvDFr}$ is far favourable above G^{H} as can be seen from the range of convergent surfaces.

As conclusion for the one spherical black hole case one can state that all the test runs obey the Eigenvalue Hypothesis, as long as the Newton method uses enough damping. Moreover the use of the goal function $G = H\ |\nabla F|^{-1}\ r$ shows the expected favourable enlargement of the region of convergence.

4.3.5 Eigenvalues for Two Black Holes

Several test runs of the eigenvalue procedure were done in the case of two black holes. These computations are considerably slower than the one black hole cases mainly because more points are needed to resolve the surface. For that reason the number of iterations was reduced and the damping was weakened (resulting in larger steps). The surfaces are represented by 12×12 points, which is still reasonable since the MOTSs typically stay almost spherical. In figure 4.8 the mean values of the height at each iteration step are presented. This time the Eigenvalue Hypothesis clearly reaches its limit. One reason is the large step size that does not resemble a Newton path. It can be seen in the upper right plot: although the eigenvalue is smaller than one (blue dashed line) and it starts with a sphere not much larger than the final solution it diverges towards zero. But on the other hand the goal function $G^{HinvDFr}$ is remarkable fast and stable, even far out solutions converged within approximately seven steps.

4.4 Conclusion on the Search for Trapped Surfaces

The eigenvalue method could provide several refinements for the determination of the apparent horizon. For example the fast flow algorithms decompose the surface into spherical harmonics. Usually these have one preferred direction (the z-axis). That means that alignment in this direction does significantly reduce the number of multipoles that are needed to form the surface with a certain precision. On the other hand misaligned surfaces might be inaccurately described. Since the

Figure 4.8: The mean value of h for each damped Newton iteration step for two black holes. Red solid (blue dashed) lines belong to series that have an eigenvalue greater (smaller) than one, respectively.

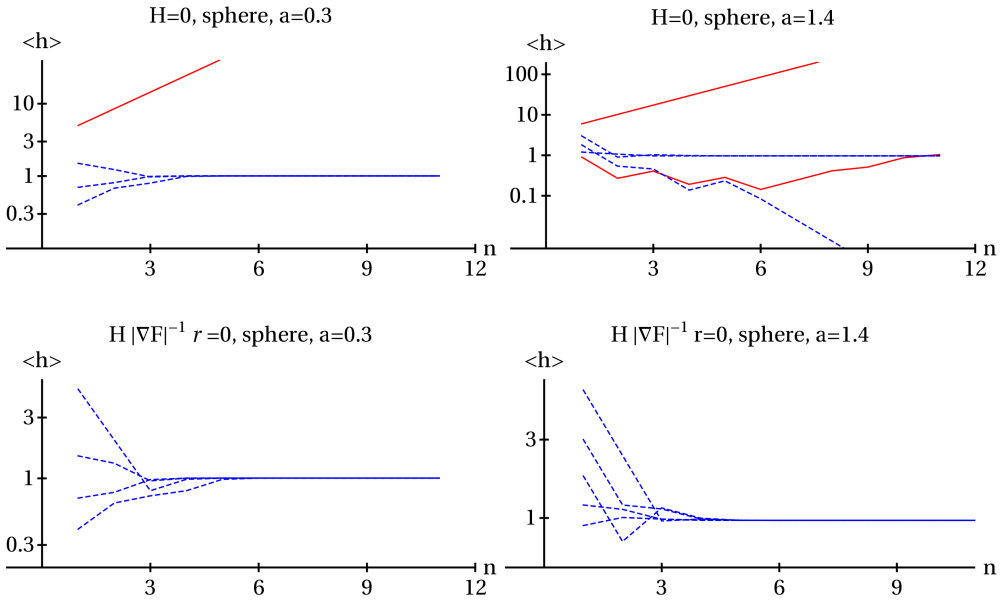

speed of the fast flow is dependent on the mode, arbitrary surfaces are less well handled. Alongside the eigenvalues the method presented in this thesis can deliver the eigenvectors. Then each particular change can be damped corresponding to the absolute maximal size of its eigenvalue. This is not dependent on any given direction.

Analyzing the eigenvectors could also be combined with a selection between several goal functions. If the standard one does exhibit an eigenvalue larger than one, a second could be tried. But still the overall computational cost is high. The eigenvalue method will be probably better used only beforehand to determine a good goal function. Once chosen the apparent horizon finder will not need the information any longer.

Finally the use of goal functions especially the one that solves the partial differential equation $H\ |\nabla F|^{-1}\ r = 0$ seems a very good alternative instead the straight forward solution of $H = 0$. Since the use of the goal function is not limited to a special representation of the surface it could be adopted to existing solvers, combining the speed of Newton's method with a reasonable robustness for the initial guess.

Chapter 5

Summary

Summary In this work two aspects of overlapping marginally outer trapped surfaces (MOTSs) in numerical relativity are examined. MOTSs are surfaces on which the expansion of outgoing null rays is zero everywhere, they are typically found around black holes. The outermost of the MOTSs is called apparent horizon. Its most important use is the determination of the mass and the spin of the enclosed black hole. The first aspect gives a deeper understanding of how MOTSs can overlap within one spatial hypersurface. The second introduces enhancements for solving the partial differential equation that governs the position of MOTSs.

For analyzing overlapping MOTSs an accurate code for axisymmetric configurations with vanishing extrinsic curvature was developed. It is based on geodesic integration and uses a two-way shooting technique. The code was applied for several configurations where the two black holes have varying separation. Even for distances as small as $a = 0.0001M$ the marginally trapped surfaces were reliably found and it is concluded that they do not overlap. As a by-product the code is used to determine the critical distance of two black holes, where the common apparent horizon is formed, to be $a_{crit} = 1.532\,394\,856\,480\,1 \pm 10^{-13}M$. The search for overlapping MOTSs was continued with a three-dimensional simulation of a two black hole merger calculated with the BAM code. With small changes to its apparent horizon finder the MOTSs could be tracked for a considerable time after the merger. However also in this setup no overlap could be seen, in contrast to older results shown by the AEI numerical relativity group. The difference was

then explained with the help of embedding diagrams: Conceptually the outline of embedding diagrams with three black holes were taken and adapted to the two black holes case. It was shown with the axisymmetric finder that three black holes can have overlapping MOTSs. It was considered that the gauge choice could produce such a behaviour.

The partial differential equation that expresses the vanishing expansion on the surface is of elliptic type. The method introduced in this thesis characterizes an initial guess for a finder of MOTSs in terms of the eigenvalue of an iteration matrix. To be more precise the finder shall solve the PDE by a Newton method. Then the iteration matrix that solves the linearized problem is the source of the eigenvalue information. It is stated that when the largest absolute eigenvalue of the iteration matrix is smaller than one, then the iteration will converge to the solution of the linear problem. This is not simply true for the non-linear case but the direction given by the Newton step is of special importance, an algorithm with a damped step size can converge to the correct solution. Since it was not possible to give a rigorous proof for general matrices, the concept was tested for several cases: First the spherical one black hole geometry where an analytic and visual understandable and therefore predictable outcome was observed. Then the test was broadened to two black holes. The eigenvalue method gives a good indication of the outcome of the iteration.

Parallel to the eigenvalue analysis a change to the partial differential equation was discussed. The idea is to solve an equation that has the same solution but has a better behaviour of convergence. The choice was mainly supported by the size of the maximal eigenvalue as seen in the one dimensional tests. The different goal functions showed a greatly improved radius of convergence also for the two black hole setups, the prominent example is the goal function $G = H\,|\nabla F|^{-1}\,r$.

Conclusion and Outlook The question about overlapping horizons was the first more programmatic search for them. In those cases of overlapping trapped surfaces reported in the literature they were found more by coincidence. There are open questions. One is the influence of the gauge that could not be established thoroughly. Second, even if it is not possible to create a complete embedding dia-

gram from the numerical data, it might be useful to at least embed the region between the two black holes. Doing so for cases of overlap and non-overlap should clarify the influence of the extrinsic curvature that reflects the different gauges.

The eigenvalue method is a new approach in this thesis. It fulfills the expectations in the spherically symmetric case but with two black holes the result is less strict. Since the result is dominated by the damping of the Newton iteration, it is more useful as an analysis tool that governs the choice of a suitable goal function in advance to a simulation. In this case the simulation could run without further checking of eigenvalues.

The use of goal functions in Newton methods is clearly favourable. The particular example $G = H\,|\nabla F|^{-1}\,r$ brought convergence to initial guesses that would otherwise fail. The computational overhead is negligible since both $|\nabla F|$ and r are computed anyway. Together with a damped Newton scheme the solutions were typically found within ten to fifteen steps. These numbers are equivalent to the number of iterations for the flow method used in the BAM code. By now the time demand however is drastically higher due to MATHEMATICA term manipulation. Comparable experiments of Schnetter [60] needed only some seconds to track a surface. The implementation of such an apparent horizon finder and comparison should be the next conclusive step.

Bibliography

[1] B. Abbott et al. Ligo: The laser interferometer gravitational-wave observatory. *arXiv:0704.3041 [gr-qc]*, 2007.

[2] F. Acernese et al. The virgo status. *Class. Quantum Grav.*, 25(114045), 2008.

[3] Miguel Alcubierre, S. R. Brandt, B. Brügmann, C. Gundlach, Joan Massó, E. Seidel, and P. Walker. Test-beds and applications for apparent horizon finders in numerical relativity. *Class. Quantum Grav.*, 17:2159–2190, 2000.

[4] Miguel Alcubierre, Bernd Brügmann, Peter Diener, Michael Koppitz, Denis Pollney, Edward Seidel, and Ryoji Takahashi. Gauge conditions for long-term numerical black hole evolutions without excision. *Phys. Rev. D*, 67:084023, 2003.

[5] L. Andersson, M. Mars, and W. Simon. Local existence of dynamical and trapping horizons. *Phys. Rev. Lett.*, 95:111102, 2005.

[6] Lars Andersson and Jan Metzger. Curvature estimates for stable marginally trapped surfaces, 2005.

[7] Lars Andersson and Jan Metzger. The area of horizons and the trapped region, 2007.

[8] M. Ando et al. Current status of the tama300 gravitational wave detector. *Class. Quantum Grav.*, 22:S881–S889, 2005.

[9] Peter Anninos, Karen Camarda, Joseph Libson, Joan Massó, E. Seidel, and W.-M. Suen. Finding apparent horizons in dynamic 3D numerical spacetimes. *Phys. Rev. D*, 58:024003, 1998.

[10] Richard Arnowitt, Stanley Deser, and Charles W. Misner. The dynamics of general relativity. In L. Witten, editor, *Gravitation: An introduction to current research*, pages 227–265. John Wiley, New York, 1962.

[11] Abhay Ashtekar, Christopher Beetle, and Stephen Fairhurst. Isolated horizons: A generalization of black hole mechanics. *Class. Quantum Grav.*, 16:L1–L7, 1999.

[12] Abhay Ashtekar and Badri Krishnan. Dynamical horizons and their properties. *Phys. Rev. D*, 68:104030, 2003.

[13] J. Baker, M. Campanelli, C. O. Lousto, and R. Takahashi. Modeling gravitational radiation from coalescing binary black holes. *Phys. Rev. D*, 65:124012, 2002. astro-ph/0202469.

[14] J. G. Baker, J. Centrella, D.-I. Choi, M. Koppitz, and J. van Meter. Gravitational-Wave Extraction from an inspiraling Configuration of Merging Black Holes. *Phys. Rev. Lett.*, 96:111102, 2006. gr-qc/0511103.

[15] T. W. Baumgarte and S. L. Shapiro. On the Numerical integration of Einstein's field equations. *Phys. Rev. D*, 59:024007, 1999. gr-qc/9810065.

[16] Thomas W. Baumgarte, Gregory B. Cook, Mark A. Scheel, Stuart L. Shapiro, and Saul A. Teukolsky. Implementing an apparent-horizon finder in three dimensions. *Phys. Rev. D*, 54(8):4849–4857, 1996.

[17] Thomas W. Baumgarte and Stuart L. Shapiro. Numerical relativity and compact binaries. *Physics Reports*, 376(2):41–131, March 2003.

[18] Nigel T. Bishop. The closed trapped region and the apparent horizon of two Schwarzschild black holes. *Gen. Rel. Grav.*, 14(9):717–723, 1982.

[19] Nigel T. Bishop. The horizons of two Schwarzschild black holes. *General Relativity and Gravitation*, 16:589–593, June 1984.

[20] D. R. Brill and R. W. Lindquist. Interaction Energy in Geometrostatics. *Phys. Rev.*, 131:471–476, 1963.

[21] B. Brügmann, W. Tichy, and N. Jansen. Numerical simulation of orbiting black holes. *Phys. Rev. Lett.*, 92:211101, 2004. gr-qc/0312112.

[22] Bernd Brügmann, José A. González, Mark Hannam, Sascha Husa, Ulrich Sperhake, and Wolfgang Tichy. Calibration of moving puncture simulations. *Phys. Rev. D 77*, 2008.

[23] A. Čadež. Apparent horizons in the two-black-hole problem. *Ann. Phys.*, 83:449–457, 1974.

[24] M. Campanelli, C. O. Lousto, P. Marronetti, and Y. Zlochower. Accurate Evolutions of Orbiting Black-Hole Binaries without Excision. *Phys. Rev. Lett.*, 96:111101, 2006. gr-qc/0511048.

[25] Manuela Campanelli, Carlos O. Lousto, Yosef Zlochower, Badri Krishnan, and David Merritt. Spin flips and precession in black-hole-binary mergers. *Phys. Rev.*, D75:064030, 2007.

[26] Gregory B. Cook. Initial data for numerical relativity. *Living Rev. Relativity*, 3:5, 2000.

[27] Gregory B. Cook and Bernard F. Whiting. Approximate Killing Vectors on S2. *Phys. Rev.*, D76:041501, 2007.

[28] Peter Deuflhard. *Newton Methods for Nonlinear Problems*. Springer, Berlin, Heidelberg, 2004.

[29] P. Diener. A new general purpose event horizon finder for 3D numerical spacetimes. *Class. Quantum Grav.*, 20(22):4901–4917, 2003.

[30] Olaf Dreyer, Badri Krishnan, Deirdre Shoemaker, and Erik Schnetter. Introduction to Isolated Horizons in Numerical Relativity. *Phys. Rev. D*, 67:24018, 2003.

[31] Pieter Geer Dykema. *The Numerical Simulation of Axially Symmetric Gravitational Collapse*. PhD thesis, University of Texas at Austin, December 1980.

[32] Albert Einstein. Die feldgleichungen der gravitation. *Preuss. Akad. Wiss. Berlin, Sitzungsber.*, pages 844–847, 1915.

[33] Albert Einstein. Zur algemeinen relativitätstheorie. *Preuss. Akad. Wiss. Berlin, Sitzungsber.*, pages 778–786, 1915.

[34] Grace/XmGrace plooting tool
`http://plasma-gate.weizmann.ac.il/Grace/`.

[35] Carsten Gundlach. Pseudo-spectral apparent horizon finders: an efficient new algorithm. *Phys. Rev. D*, 57:863–875, 1998.

[36] Mark Hannam, Sascha Husa, Frank Ohme, Bernd Bruegmann, and Niall O'Murchadha. Wormholes and trumpets: the Schwarzschild spacetime for the moving-puncture generation. *Phys. Rev.*, D78:064020, 2008.

[37] Stephen W. Hawking and George F. R. Ellis. *The Large Scale Structure of Space-Time*. Cambridge University Press, Cambridge (UK), 1973.

[38] Sean A. Hayward. General laws of black hole dynamics. *Phys. Rev. D*, 49(12):6467–6474, 15 June 1994.

[39] H.R.Schwarz. *Numerische Mathematik*. Teubner, 1997. 4th edition.

[40] S. Husa. *Asymptotically Flat Initial Data for Gravitational Wave Space-times, Conformal Compactification and Conformal Symmetry*. PhD thesis, University of Vienna, 1998.

[41] O. Jennrich. LISA technology and instrumentation. *arXiv*, 2009.

[42] A. J. Kemball and Nigel T. Bishop. The numerical determination of apparent horizons. *Class. Quantum Grav.*, 8(7):1361–1367, July 1991.

[43] Lawrence Livermore National Laboratory. Visit – visualization tool, 2009. Versions 1.6 and 1.11.

[44] Jan Metzger Lars Andersson, Marc Mars and Walter Simon. The time evolution of marginally trapped surfaces. *Classical and Quantum Gravity*, 26(8):085018 (14pp), 2009.

[45] Luis Lehner. Numerical relativity: A review. *Class. Quantum Grav.*, 18:R25–R86, 2001.

[46] Lap-Ming Lin and Jerome Novak. A new spectral apparent horizon finder for 3D numerical relativity. *Class. Quant. Grav.*, 24:2665–2676, 2007.

[47] Mathematica - computational software package, versions 6 and 7.

[48] Richard A. Matzner, Mijan F. Huq, and Deirdre Shoemaker. Initial data and coordinates for multiple black hole systems. *Phys. Rev. D*, 59:024015, 1999.

[49] Jan Metzger. Numerical computation of constant mean curvature surfaces using finite elements. *Class. Quantum Grav.*, 21(19):4625–4646, 2004.

[50] C. Misner and J. Wheeler. Classical physics as geometry. *Ann. Phys. (N.Y.)*, 2:525, 1957.

[51] Charles W. Misner, Kip S. Thorne, and John A. Wheeler. *Gravitation*. W. H. Freeman, San Francisco, 1973.

[52] Takashi Nakamura, Yasufumi Kojima, and Ken-ichi Oohara. A method of determining apparent horizons in three-dimensional numerical relativity. *Phys. Lett. A*, 106(5-6):235–238, 10 December 1984.

[53] U. Nowak and L. Weimann. A family of newton codes for systems of highly nonlinear equations. Technical Report TR 91-10, Konrad-Zuse-Zentrum für Informationstechnik Berlin, December 1991.

[54] F. S. Guzman P. Diener. The wave equation in 1+1. Lecture Notes, 2003.

[55] Eberhard Pasch. The level set method for the mean curvature flow on $(\Re^3, g)$. Technical Report 63, University of Tübingen, Tübingen, Germany, February 1997. report of the Sonderforschungsbereich 382 project.

[56] Roger Penrose. Gravitational collapse and space-time singularities. *Phys. Rev. Lett.*, 14:57, 1965.

[57] William H. Press, Brian P. Flannery, Saul A. Teukolsky, and William T. Vetterling. *Numerical Recipes in C++: The Art of Scientific Computing*. Cambridge University Press, Cambridge (UK) and New York, 2nd edition, 2002.

[58] Frans Pretorius. Simulation of binary black hole spacetimes with a harmonic evolution scheme. *Class. Quantum Grav.*, 23:S529–S552, 2006.

[59] Erik Schnetter. A fast apparent horizon algorithm. gr-qc/0206003, 2002.

[60] Erik Schnetter. Finding apparent horizons and other two-surfaces of constant expansion. *Class. Quantum Grav.*, 20(22):4719–4737, 2003.

[61] Erik Schnetter, Frank Herrmann, and Denis Pollney. Horizon pretracking. *Phys. Rev. D*, 71:44033, 2005.

[62] M. Shibata and T. Nakamura. Evolution of three-dimensional gravitational waves: Harmonic slicing case. *Phys. Rev. D*, 52:5428–5444, 1995.

[63] Deirdre M. Shoemaker, Mijan F. Huq, and Richard A. Matzner. Generic tracking of multiple apparent horizons with level flow. *Phys. Rev. D*, 62:124005, 2000.

[64] L. Smarr, A. Čadež, B. DeWitt, and K. Eppley. Collision of two black holes: Theoretical framework. *Phys. Rev. D*, 14:2443–2452, 1976.

[65] B. Szilágyi, D. Poolney, L. Rezzolla, J. Thornburg, and J. Winicour. An explicit harmonic code for black-hole evolution using excision. *only ArXiv*, 2006. gr-qc/0612150.

[66] Marcus Thierfelder. Finding event horizons in multiple black hole simulations. Talk at the DPG meeting in Munich, Germany, 12.03.2009, 2009.

[67] Marcus Thierfelder. Finding event horizons in multiple black hole simulations. Talk at the Marcel Grossmann Meeting 12, Paris, France, 13.07.2009, 2009.

[68] Marcus Thierfelder. private communication. Jena, 2009.

[69] J. Thornburg. Finding apparent horizons in numerical relativity. *Phys. Rev. D*, 54(8):4899–4918, October 15 1996. gr-qc/9508014.

[70] Jonathan Thornburg. A fast apparent-horizon finder for 3-dimensional Cartesian grids in numerical relativity. *Class. Quantum Grav.*, 21(2):743–766, 21 January 2004.

[71] Jonathan Thornburg. Event and apparent horizon finders for 3 + 1 numerical relativity. *Living Rev. Relativity*, 2006. [Online article].

[72] Robert M. Wald. *General relativity*. The University of Chicago Press, Chicago, 1984.

[73] Robert M. Wald and Vivek Iyer. Trapped surfaces in the Schwarzschild geometry and cosmic censorship. *Phys. Rev. D*, 44:R3719–R3722, 1991.

[74] Eric W. Weisstein. Enneper's minimal surface. *MathWorld – A Wolfram Web Resource*, 2009. [Online article] http://mathworld.wolfram.com-/EnnepersMinimalSurface.html.

[75] B. Willkes et al. The geo 600 gravitational wave detector. *Class. Quantum Grav.*, 19:S1377–S1387, 2002.

[76] Xfig drawing tool, http://www.xfig.org.

[77] James W. York. Kinematics and dynamics of general relativity. In Larry L. Smarr, editor, *Sources of gravitational radiation*, pages 83–126. Cambridge University Press, Cambridge, UK, 1979.

Appendix A

Notation and Abbreviations

Throughout the thesis certain abbreviations for frequent expressions can be found. Their definitions are in the text but might sometimes not be found immediately. For concreteness all uncommon notations are summarized below.

Natural units are applied such that $c = G = 1$.

Greek indices μ, ν indicate four-dimensional quantities, small Latin letters from the middle of the alphabet i, j, k etc. indicate three-dimensional objects and small Latin letters from the beginning of the alphabet a, b, etc. are for objects that belong to the two-dimensional surface.

$\mathbf{x} \sim \mathbf{s}$ means that variable x has the same order of magnitude as expression s.

$\mathbf{h}_{,\theta}, \mathbf{h}_{,\phi}, \mathbf{h}_{,\theta\theta}, \mathbf{h}_{,\phi\phi}, \mathbf{h}_{,\theta\phi}$ mean $\frac{\partial}{\partial\theta}h$, $\frac{\partial}{\partial\phi}h$, $\frac{\partial^2}{\partial\theta\partial\theta}h$, $\frac{\partial^2}{\partial\phi\partial\phi}h$, $\frac{\partial^2}{\partial\theta\partial\phi}h$, respectively.

$\mathbf{\Lambda}^{\mathbf{G}}_{\mathbf{S}}$ means the maximal absolute eigenvalue of the iteration matrix that belongs to one Newton step for the goal function G evaluated at surface S.

$\mathbf{G}^{\mathbf{X}}$ the goal function with equation $X = 0$

Appendix B

Axisymmetric Code Precision

In chapter 2 it was stated that for runs with fixed step size the runs are not convergent if the step size is too small. The accuracy of the code levels off at about 10^{-12}. As comparison convergence rates for runs with type LONG DOUBLE instead of DOUBLE where computed. With the system and compiler used, that means an increase from around 15 to 18 digits in precision. The equivalent to table 2.1 is shown in table B.1. It can be seen that the same smallness of the step size $\Delta\lambda$ is needed to reach the convergent regime. The additional digits will hold the fourth order of convergence also for smaller values of the step size. The differences of the three resolutions settles at around 10^{-15} instead of 10^{-12} for DOUBLE variables, that is consistent with the proposed increase of three digits in the precision of the variables.

Table B.1: Results of convergence tests for type LONG DOUBLE. Nomenclature is as in table 2.1.

$\Delta\lambda$	$\rho_0 =$	.1	.01	.001	.0001
10^{-2}		3.8	-	-	-
10^{-3}		4	-	-	-
10^{-4}		4	3.8	-	-
10^{-5}		+	4	-	-
10^{-6}		+	+	3.8	-
10^{-7}		+	+	4	-
10^{-8}		+	+	+	3.8

Appendix C

The Linearized Perturbations

The linearizations of the perturbations of the height functions and their derivatives to first order. Equations that are marked by (*) are not needed in equation (4.19). Terms including first derivatives:

$$
\begin{aligned}
h_{,\theta}^2 &\approx h_{0,\theta}^2 + 2h_{0,\theta}h_{1,\theta}, \\
h_{,\phi}^2 &\approx h_{0,\phi}^2 + 2h_{0,\phi}h_{1,\phi}, \\
h_{,\theta}h_{,\phi} &\approx h_{0,\theta}h_{0,\phi} + h_{0,\theta}h_{1,\phi} + h_{0,\phi}h_{1,\theta}, \\
h_{,\theta}^3 &\approx h_{0,\theta}^3 + 3h_{0,\theta}^2h_{1,\theta}, \\
h_{,\theta}^2h_{,\phi} &\approx h_{0,\theta}^2h_{0,\phi} + h_{0,\theta}^2h_{1,\phi} + 2h_{0,\theta}h_{0,\phi}h_{1,\theta}, \\
h_{,\theta}h_{,\phi}^2 &\approx h_{0,\theta}h_{0,\phi}^2 + h_{0,\phi}^2h_{1,\theta} + 2h_{0,\theta}h_{0,\phi}h_{1,\phi}, \\
h_{,\phi}^3 &\approx h_{0,\phi}^3 + 3h_{0,\phi}^2h_{1,\phi}.
\end{aligned}
\tag{C.1}
$$

Terms that include $h_{,\theta\theta}$:

$$
\begin{aligned}
h_{,\theta\theta} &= h_{0,\theta\theta} + h_{1,\theta\theta}, \\
h_{,\theta\theta}h_{,\theta} &\approx h_{0,\theta\theta}h_{0,\theta} + h_{0,\theta\theta}h_{1,\theta} + h_{0,\theta}h_{1,\theta\theta}, \quad (*) \\
h_{,\theta\theta}h_{,\phi} &\approx h_{0,\theta\theta}h_{0,\phi} + h_{0,\theta\theta}h_{1,\phi} + h_{0,\phi}h_{1,\theta\theta}, \\
h_{,\theta\theta}h_{,\theta}^2 &\approx h_{0,\theta\theta}h_{0,\theta}^2 + 2h_{0,\theta\theta}h_{0,\theta}h_{1,\theta} + h_{0,\theta}^2h_{1,\theta\theta}, \quad (*) \\
h_{,\theta\theta}h_{,\phi}^2 &\approx h_{0,\theta\theta}h_{0,\phi}^2 + 2h_{0,\theta\theta}h_{0,\phi}h_{1,\phi} + h_{0,\phi}^2h_{1,\theta\theta}, \\
h_{,\theta\theta}h_{,\theta}h_{,\phi} &\approx h_{0,\theta\theta}h_{0,\theta}h_{0,\phi} + h_{0,\theta\theta}(h_{0,\theta}h_{1,\phi} + h_{1,\theta}h_{0,\phi}) + h_{0,\theta}h_{0,\phi}h_{1,\theta\theta}. \quad (*)
\end{aligned}
\tag{C.2}
$$

Terms including $h_{,\phi\phi}$:

$$
\begin{aligned}
h_{,\phi\phi} &= h_{0,\phi\phi} + h_{1,\phi\phi}, \\
h_{,\phi\phi}h_{,\theta} &\approx h_{0,\phi\phi}h_{0,\theta} + h_{0,\phi\phi}h_{1,\theta} + h_{0,\theta}h_{1,\phi\phi}, \\
h_{,\phi\phi}h_{,\phi} &\approx h_{0,\phi\phi}h_{0,\phi} + h_{0,\phi\phi}h_{1,\phi} + h_{0,\phi}h_{1,\phi\phi}, \quad (*) \\
h_{,\phi\phi}h_{,\theta}^2 &\approx h_{0,\phi\phi}h_{0,\theta}^2 + 2h_{0,\phi\phi}h_{0,\theta}h_{1,\theta} + h_{0,\theta}^2h_{1,\phi\phi}, \\
h_{,\phi\phi}h_{,\phi}^2 &\approx h_{0,\phi\phi}h_{0,\phi}^2 + 2h_{0,\phi\phi}h_{0,\phi}h_{1,\phi} + h_{0,\phi}^2h_{1,\phi\phi}, \quad (*) \\
h_{,\phi\phi}h_{,\theta}h_{,\phi} &\approx h_{0,\phi\phi}h_{0,\theta}h_{0,\phi} + h_{0,\phi\phi}(h_{0,\theta}h_{1,\phi} + h_{1,\theta}h_{0,\phi}) + h_{0,\theta}h_{0,\phi}h_{1,\phi\phi}. \quad (*)
\end{aligned}
\tag{C.3}
$$

Terms including $h_{,\theta\phi}$:

$$
\begin{aligned}
h_{,\theta\phi} &= h_{0,\theta\phi} + h_{1,\theta\phi}, \\
h_{,\theta\phi}h_{,\theta} &\approx h_{0,\theta\phi}h_{0,\theta} + h_{0,\theta\phi}h_{1,\theta} + h_{0,\theta}h_{1,\theta\phi}, \\
h_{,\theta\phi}h_{,\phi} &\approx h_{0,\theta\phi}h_{0,\phi} + h_{0,\theta\phi}h_{1,\phi} + h_{0,\phi}h_{1,\theta\phi}, \\
h_{,\theta\phi}h_{,\theta}^2 &\approx h_{0,\theta\phi}h_{0,\theta}^2 + 2h_{0,\theta\phi}h_{0,\theta}h_{1,\theta} + h_{0,\theta}^2h_{1,\theta\phi}, \quad (*) \\
h_{,\theta\phi}h_{,\phi}^2 &\approx h_{0,\theta\phi}h_{0,\phi}^2 + 2h_{0,\theta\phi}h_{0,\phi}h_{1,\phi} + h_{0,\phi}^2h_{1,\theta\phi}, \quad (*) \\
h_{,\theta\phi}h_{,\theta}h_{,\phi} &\approx h_{0,\theta\phi}h_{0,\theta}h_{0,\phi} + h_{0,\theta\phi}(h_{0,\theta}h_{1,\phi} + h_{1,\theta}h_{0,\phi}) + h_{0,\theta}h_{0,\phi}h_{1,\theta\phi}.
\end{aligned}
\tag{C.4}
$$

Appendix D

Analytic Argumentation in Axial Symmetry

Here the case that two axial and reflection symmetric black holes in Brill Lindquist geometry shall have overlapping marginally trapped surfaces is considered. The idea is to show that MOTSs can not touch. Then a smooth transition from the far limit to a hypothetical overlapping state is not possible. However it turns out that they can touch but it gives some restriction on the form of the surface. At first the surface region near to the origin is approximated by a sphere, then a more general fractional polynomial was used.

Consider the metric of a hypersurface of time symmetry

$$g_{ij} = \left(1 + \frac{m}{2}\left(\frac{1}{r_-} + \frac{1}{r_+}\right)\right)^4 \delta_{ij} \ , \tag{D.1}$$

$$r_\pm = \sqrt{\rho^2 + (z \mp a/2)^2} \tag{D.2}$$

where a is the coordinate distance between the black holes. The marginally trapped surfaces are given by the minimal surface equation $\nabla_i s^i = 0$ based on the outward unit normal s^i

$$s^i = \frac{n^i}{\sqrt{g_{kl}\, n^k n^l}} \ . \tag{D.3}$$

Assume $\mathcal{S}$ be a surface that goes through the origin (see figure D.1). Near to it the surface shall be described by a sphere $K_{|R|}((0|0|R))$ that has its center on the

Figure D.1: Outline of surfaces near to origin,. *Left*: like a sphere, *right*: according to a fractional polynomial.

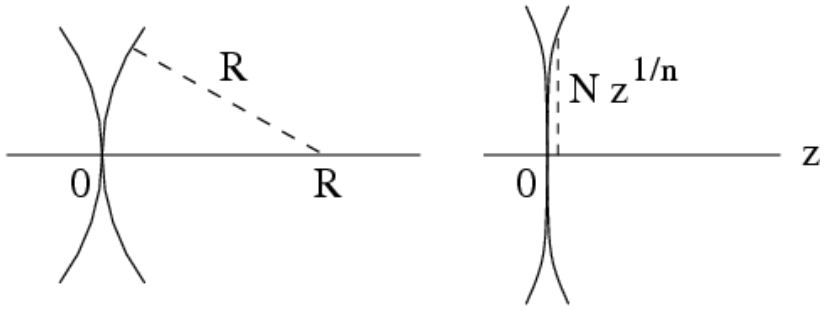

axis. The expansion at the origin is

$$\nabla_i s^i_{(\text{sphere})} = \frac{2}{R\psi^2} = \frac{2}{R(1+2m/a)^2} \ . \tag{D.4}$$

The only possibility for the expansion to vanish is that $R \to \infty$. The surface is then flat near the origin. This is not surprising, because the influence of both black holes cancel. At first sight this might suggest that only surfaces that are flat can have vanishing expansion at the origin. But the following more general surfaces do.

Consider surfaces that near to the origin have the form

$$\rho = \sqrt{x^2+y^2} = Nz^{1/n} \tag{D.5}$$

with constants $N > 0$ and $n \geq 2$. The expansion at the origin in this layout is

$$\nabla_i s^i_{(z^{1/n})} = \lim_{z\to 0}\left[\left(1+\frac{2m}{a}\right)^{-2}\frac{n-1+N}{N^2}z^{1-2/n}\right]. \tag{D.6}$$

For $n = 2$ and finite N the expansion is a positive constant, only for $N \to \infty$ the expansion vanishes. This is the case that corresponds to the spheres with increasing radius. The big difference comes for $n \geq 3$ where $1-2/n > 0$. Then the limit in equation (D.6) can be taken and the resulting expansion is always zero. This reflects the fact that the metric has the form of a saddle point around the

origin and the expansion is zero for a plane along the axis of reflection symmetry. Every surface that exhibits more than a quadratic increase of the distance ρ from the origin from the z-axis with respect to z will be considered as flat around the origin in this context. So the possibility that the surfaces touch and thus may also overlap is not ruled out but some limitations on the form of the surface near the origin are given.

Appendix E

Theorem on the Newton Path

The following lines restate the prerequisites for theorem 3.6 from Deuflhard [28]. The functional $F(x)$ there corresponds to $H(h)$ in this thesis. A more general level function $T(x|A)$ is given as

$$T(x|A) \coloneqq \frac{1}{2}||AF(x)||^2 = \frac{1}{2}(AF(x))^T AF(x) \tag{E.1}$$

for an arbitrary nonsingular matrix A. The level sets

$$G(z|A) \coloneqq \{x \in D \subseteq \mathbb{R}^n | T(x|A) \leq T(z|A)\} \tag{E.2}$$

grep all surfaces with a measure smaller than z depending on A and the union

$$\bar{G}(x) \coloneqq \bigcap_{A \in GL(n)} G(x|A) \tag{E.3}$$

is used to remove the arbitrariness out of the definition. $GL(n)$ is the set of all nonsingular $n \times n$ matrices. The function F has to be $C^1(D)$ and $F'(x)$ nonsingular inside the considered domain $D \in \mathbb{R}^n$. For some $\hat{A} \in GL(n)$, the path-connected component of $G(x^0|\hat{A})$ in x^0 shall be compact and contained in D. Then the path-connected component of $\bar{G}(x^0)$ is a topological path, the Newton path. Additional properties are listed in the reference.

Appendix F

Influence of Damping on Convergence

It is examined in an example how different values of the damping parameter can change the behaviour of Newton's method. In figure F.1 the same initial data was iterated for ten steps and the mean value of the height is plotted. The difference between the plots lies in the damping, that is given by three numbers (normal, step limit, full step). The first is the value from equation (4.57). The second gives the maximal ratio between the change of the height and the mean height, thus in principle that should prevent large jumps. When the ratio between the maximal change of the height and the mean height is smaller than the last parameter, the algorithm does not use damping at all, which should speed up the iteration near to the solution.

For the comparison of the different plots the behaviour of the blue dashed lines are important, that are those with maximal eigenvalue smaller than one. Low damping results in two lines that do not converge although their mean height is relatively close to the final one. With increased damping first one (middle plot) then also the second of these problematic initial surfaces (bottom plot) does converge.

Figure F.1: Damped Newton iteration with increasingly higher damping. Damping parameters from top to bottom (0.4,0.7.0.3), (0.3,0.6,0.3) and (0.2,0.5,0.2). With low damping some iterations fail to converge, more damping helps.

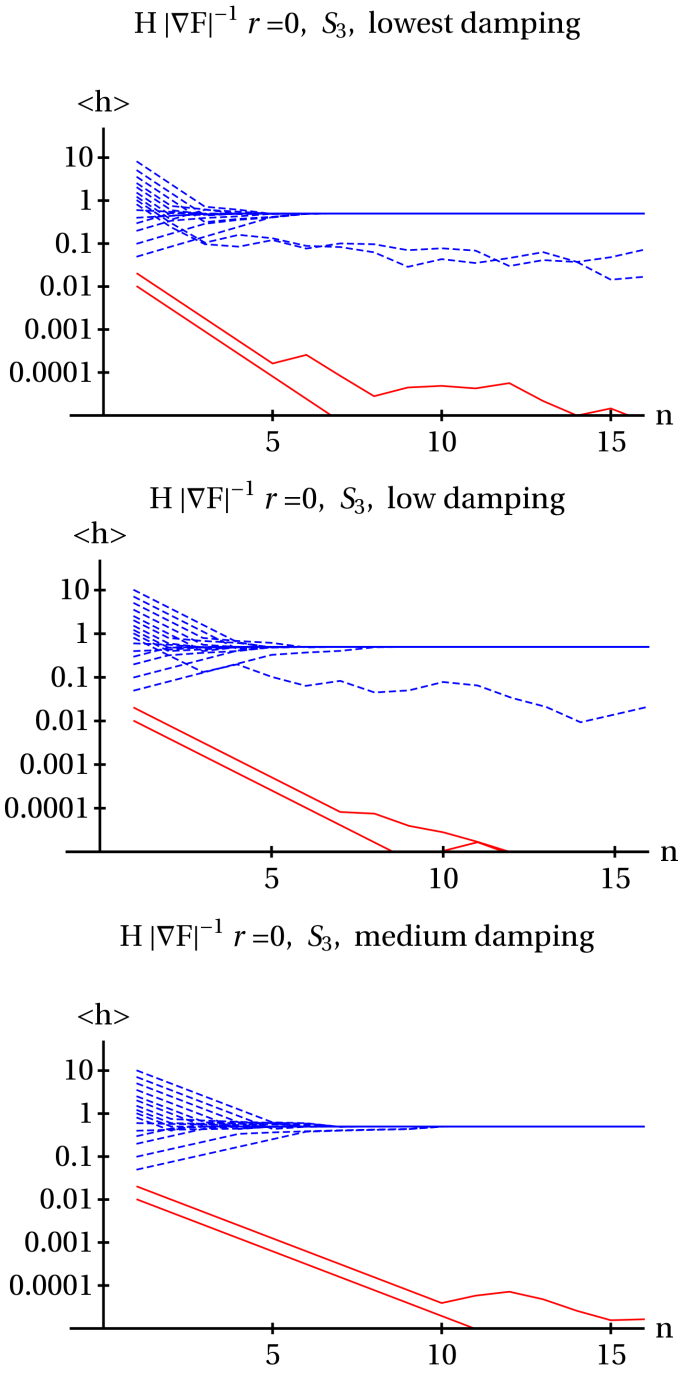

Miscellaneous

The pictures and diagrams were produced by the following programs:
The picture 3.4 of the evolution of two black holes was visualized with VisIt [43].
The drawings are made with Xfig [76].
The drawing 2.5 was made with XmGrace [34].
All other diagrams were made with MATHEMATICA [47].
The typesetting was done by LaTeX.
Wikipedia (http://de.wikipedia.org/) was used for introductory reading and links to some topics (e.g. minimal surfaces).
The English language was checked with the help of the online dictionary LEO (http://dict.leo.org) and the program ispell (http://ficus-www.cs.ucla.edu/geoff/-ispell.html).

Acknowledgements

This work was created in the stimulating environment of the gravity group at the theoretical physics institute of the university of Jena. Foremost, I thank my supervisor Bernd Brügmann for his help and support during my dissertation. My thanks to all colleagues who made this an enjoyable time over the years. I am thankful to Roman Gold and David Hilditch for their careful proof-reading of the manuscript. And last but not least I thank my parents for their support during all the years.

This work was financially supported by the Collaborative Research Centre/ Transregio 7 'Gravitational Wave Astronomy' of the German Research Foundation (DFG).

Ehrenwörtliche Erklärung

Ich erkläre hiermit ehrenwörtlich, dass ich die vorliegende Arbeit selbständig, ohne unzulässige Hilfe Dritter und ohne Benutzung anderer als der angegebenen Hilfsmittel und Literatur angefertigt habe. Die aus anderen Quellen direkt oder indirekt übernommenen Daten und Konzepte sind unter Angabe der Quelle gekennzeichnet.

Bei der Auswahl und Auswertung folgenden Materials haben mir die nachstehend aufgeführten Personen in der jeweils beschriebenen Weise unentgeltlich geholfen:

1. Gerhard Zumbusch: Literatur zu nicht-linearen Differentialgleichungen

Weitere Personen waren an der inhaltlich-materiellen Erstellung der vorliegenden Arbeit nicht beteiligt. Insbesondere habe ich hierfür nicht die entgeltliche Hilfe von Vermittlungs- bzw. Beratungsdiensten (Promotionsberater oder anderen Personen) in Anspruch genommen. Niemand hat von mir unmittelbar oder mittelbar geldwerte Leistungen für Arbeiten erhalten, die im Zusammenhang mit dem Inhalt der vorgelegten Dissertation stehen.

Die Arbeit wurde bisher weder im In- noch im Ausland in gleicher oder ähnlicher Form einer anderen Prüfungsbehörde vorgelegt.

Die geltende Promotionsordnung der Physikalisch-Astronomischen Fakultät ist mir bekannt.

Ich versichere ehrenwörtlich, dass ich nach bestem Wissen die reine Wahrheit gesagt und nichts verschwiegen habe.

Jena, 25.09.2009 Norbert Lages

Lebenslauf

	Lages, Norbert
23.10.1978	Geburt in Überlingen
1985 - 1989	Grundschule Hödingen
1989 - 1998	Gymnasium Überlingen
1998	Abschluss Abitur
1998 - 1999	Zivildienst: Jugendherberge Burg Wildenstein
1999 - 2005	Physikstudium Universität Tübingen
2001 - 2002	Auslandssemester: Trent University, Peterborough, Kanada
Jun - Okt 2002	Praktikum bei der Robert Bosch GmbH, Gerlingen
12/2005	Abschluss Diplom-Physiker
Jan - Apr 2006	Praktikum bei der MAHLE GmbH, Stuttgart
2006 - 2009	Wissenschaftlicher Mitarbeiter Universität Jena

Jena, 25.09.2009 Norbert Lages

Veröffentlichungen

- Kurt Langfeld, Norbert Lages and Hugo Reinhardt, *Zero density heavy quark SU(2) gauge theory and the Stefan-Boltzmann limit* presented at Lattice2005 (Nonzero temperature and density), PoS (LATTICE 2005), arXiv:hep-lat/0509156

Vorträge

- DPG-Tagung 2009, München, *Apparent Horizon Finding*, 12.03.2009
- Marcel Grossmann 12, Paris, *Overlapping Marginally Trapped Surfaces*, 15.07.2009